Title

DIMENSIONALITY AND ITS EFFECTS UPON THE VALENCE ELECTRONIC STRUCTURE OF ORDERED METALLIC SYSTEMS

Author

Tobin, J.G.

Publication Date

1983-07-01

Lawrence Berkeley Laboratory
UNIVERSITY OF CALIFORNIA

Materials & Molecular Research Division

DIMENSIONALITY AND ITS EFFECTS UPON THE VALENCE ELECTRONIC STRUCTURE OF ORDERED METALLIC SYSTEMS

J.G. Tobin
(Ph.D. Thesis)

July 1983

Prepared for the U.S. Department of Energy under Contract DE-AC03-76SF00098

DISCLAIMER

LBL-14704

DIMENSIONALITY AND ITS EFFECTS UPON THE VALANCE ELECTRONIC STRUCTURE OF ORDERED METALLICA SYSTEMS

James Gerard Tobin
(Ph.D. Thesis)

Lawrence Berkeley Laboratory
University of California
Berkeley, California 94720

July 1983

This work was supported by the Director, Office of Energy Research, Office of Basic Energy Sciences, Chemical Sciences Division of the U.S. Department of Energy under Contract No. DE-AC03-76SF00098. It was performed at the Stanford Synchrotron Radiation Laboratory, which is supported by the NSF through the Division of Materials Research.

DIMENSIONALITY AND ITS EFFECTS UPON THE VALENCE ELECTRONIC STRUCTURE OF ORDERED METALLIC SYSTEMS

James Gerard Tobin

ABSTRACT

The system c(10x2)Ag/Cu(001) was investigated with Angle-Resolved Photoemission (ARP), Low Energy Electron Diffraction (LEED) and Auger Electron Spectroscopy (AES). LEED and AES provided the calibration of a quartz microbalance used to measure the amount of silver evaporated onto the copper single crystal and also established the monolayer geometrical structure at one monolayer exposure. An off-normal ARP bandmapping study performed with polarized HeI and NeI radiation demonstrated the electronically two-dimensional nature of the silver d-bands at coverages of near one monolayer. The states at the surface Brillouin Zone center were assigned upon the basis of their polarization dependences and a structural model of hexagonal symmetry. A normal emission ARP experiment was performed at the Stanford Synchrotron Radiation Laboratory (SSRL) over the photon energy range of 6-32 eV. Data from it documented the evolution of the valence electronic structure of the silver overlayer from a two-dimensional hexagonal valence to a three- dimensional behavior converging towards that of bulk Ag(111). A structural study was attempted using the ARP technique of Normal Emission Photoelectron Diffraction over the photon energy range of 3.4 to 3.7 keV at SSRL, the results of which are inconclusive.

TABLE OF CONTENTS

I. General Introduction

Silver evaporated onto Cu(001) forms an ordered structure that is referred to as c(10x2)Ag/Cu(001). The structural model associated with this label is a slightly strained (±2 percent) hexagonal array that can properly explain the kinematics of the observed Low Energy Electron Diffraction (LEED) pattern if the combined symmetry of the adsorbate and substrate is considered. LEED and Auger Electron Spectroscopy (AES) results indicate that the structure at one monolayer exposure is truly a monolayer slab of silver on top of the Cu(001) surface. The growth mode at exposures above one monolayer has, until now, been totally unknown. The interlayer spacing is not known.

Thus this system was ripe for investigation with Angle-Resolved Photoemission (ARP). ARP has the capability to obtain both energy and directional or momentum information from an analysis of the photoelectrons ejected from the sample. By its very nature, it is much less surface-destructive and surface-reactive than techniques which rely upon electron stimulated excitation. The dipole selection rules which govern it provide a particularly simple framework within which to analyze the symmetry dependences of the emission features caused by the absorption of polarized light. Moreover, the ARP spectra obtained from single crystal systems are material, energy, direction and polarization specific. In essence, they are the fingerprints of the the surface and its electronic structure.

The remainder of the thesis deals with a series of LEED, AES and especially ARP experiments, the goal of which was the complete elucidation of the electronic and geometrical structures of Ag/Cu(001) and the investigation of the effects of dimensionality upon them. Chapter II describes an off-normal ARP bandmapping experiment that established the two-dimensional behavior of the silver d-bands at coverages near one monolayer. Chapter III describes a normal emission ARP study that demonstrated the evolution of the the valence electronic structure of the silver overlayer from two-dimensional to three-dimensional behavior, as the exposure was increased to five monolayers. Chapter IV describes a high resolution ARP experiment performed upon bulk, single crystal Ag(111) to complement the overlayer data. Chapter V describes a Normal Emission Photoelectron Diffraction (NPD) study which was attempted to determine the interplanar spacing of a monolayer of c(10x2)Ag/Cu(001), the results of which are inconclusive. Finally, Chapter VI is an overview with final conclusions.

II. THE TWO-DIMENSIONAL VALENCE ELECTRONIC STRUCTURE OF A MONOLAYER OF Ag ON Cu(001)

A. INTRODUCTION

Complex surfaces consisting of metal overlayers on different metallic substrates have been studied in a number of photoemission experiments[1-9] and theoretical works.[10,11] In a related development, considerable attention has been focussed upon the calculation of the electronic properties of thin metal slabs[11-17] as functions of thickness. To date, most of this effort has concentrated upon density-of-states (DOS) measurements. With the exception of References 6,7 and 8, experimental results have been limited by the unresolved nature of angle-integrated photoemission. In this thesis and related papers,[9] the first complete resonance lamp and synchrotron radiation angle-resolved photoemission experiment on such a system is presented, including a mapping of the dispersion relations of the overlayer valence bands and the assignment of the observed states on the basis of the polarization dependence of these features and a group-theoretical analysis.

The system c(10x2) Ag/Cu(001) was chosen for several reasons. Earlier Low Energy Electron Diffraction (LEED) and Auger studies[18] had demonstrated that the c(10x2)Ag was a single close-packed-hexagonal layer at monolayer exposures. Both the substrate Cu(001)[19] and Ag(111,)[20-25] which is the 3-dimensional analog of the c(10x2)Ag, had been thoroughly investigated. Silver and

copper are remarkably stable and Cu(001)[26,27] has a well defined surface states (B^F= 1.8eV near $\bar{M}$ in the Cu(001) Surface Brillouin Zone) that can be used for surface characterization. Moreover, the valence bands of Cu(001) and Ag(111) show relatively little overlap in energy.

This chapter is organized into four more sections. Experimental procedures are described in Section B, and photoemission results are given in Section C. These results are discussed in Section D, in which the two-dimensional dispersion relations are derived, and group-theoretical arguments are used to establish band symmetries. Conclusions appear in Section E.

B. EXPERIMENTAL

This Section has two parts. General procedures are described first, then the LEED/Auger calibration of the sample coverage is treated in detail.

1. GENERAL PROCEDURES

The experiment was performed in an angle-resolved photoelectron spectrometer, using a polarized photon beam from a gas discharge lamp, documented elsewhere.[27] HeI (21.22 eV) and NeI (16.67, 16.85 eV) were used as excitation lines. The base pressure was 2-3 x 10^{-10} Torr, and during lamp operation the pressure rose into the 10^{-9} Torr regime. Two copper crystals were cut and polished to within ±1° of the (001) crystallographic plane. Both were chemically polished to remove the surface layers. The solution used on the first crystal included HCl (Ref. 28), while that used on the second did not (Ref.

29). Samples were cleaned by continuous Ar ion etching during cycles of heating and cooling at pressures of 10^{-5} Torr, with maximum temperatures of 500-600°C, except that removal of all evaporated silver, as determined by Auger spectroscopy, was achieved by extended room- temperature sputtering prior to the beginning of cycling. This was done to minimize the danger of alloying. A final anneal to 500-600°C was performed on the cleaned sample to order the surface, as confirmed by LEED. For the annealed surface, the impurity to copper Auger derivative peak height ratios were typically 0.005 or less for carbon, 0.003 or negligible for sulfur, and negligible for oxygen and silver. The success of the cleaning procedure was confirmed by observing the $\bar{M}$ surface state of Cu(001). Similar Auger measurements were made after the silver exposures and photoemission experiments.

Evaporation was performed by a shielded thermal source of Ag, equipped with a shutter for time control of exposures and a water-cooled quartz crystal microbalance inside the shielding to monitor the evaporation rate. The microbalance was positioned closer to the source, to intercept a larger solid angle. The pressure rose negligibly during the evaporation operation , generally remaining below the mid 10^{-10} Torr range.

Resolution in the photoemission measurements was determined by a convolution of the source line width, which is negligible, the effect of the NeI doublet, and the analyzer resolution, which is 0.006 PE, where PE is the pass energy of the hemispherical analyzer. All measurements were taken at either 10 eV, 20 eV, or 40 eV pass energy. At normal emission and polar emission angles less than or equal to

30°, the polar angle of incidence, $\theta_{h\nu}$, of the light was 60° with respect to the normal (Figure 1). For polar photoelectron emission angles, θ_e, larger than 30°, the angle of incidence was such that $\theta_{h\nu} + \theta_e = 90°$. Measurements were made with the polarization both in the plane of the surface (s-polarization) and in the plane of rotation (p-polarization).

Samples were aligned by laser autocollimation and with LEED. Spectra were taken on both sides of the spectrometer; thus laser autocollimation was performed through several different windows. There is an assumed relative error of ±1° in each alignment, introduced by using different windows or LEED. Limited distortion of the LEED patterns and loss of low kinetic energy electrons in the photoemission spectra was observed. Apparently this was due to charging of the sample plate insulators, particularly after silver exposures.

2. THE LEED/AUGER CALIBRATION

An exact knowledge of the amount of Ag deposited upon the surface was crucial. While the quartz microbalance provided a precise relative measure of the evaporation rate, it was necessary to determine experimentally the thickness monitor coverage equivalent to one monolayer coverage on the crystal. This was done by taking a series of Auger and LEED measurement of surfaces at progressively higher exposures.

An earlier experiment[30] performed on the system Ag/Ni(001) demonstrated the validity of a model that predicted abrupt changes in

slope of Auger intensity versus coverage at coverages of integral monolayers, in systems which grow layer-by-layer. Subsequent experimentation has confirmed this in several systems.[4-7]

Owing to the sensitivity of the absolute Auger signal upon positioning relative to the focus of the LEED optics, measurements on this system were made in terms of the ratio of the adsorbate to substrate signals. While this complicates the model slightly by removing the linear dependences, the essential feature of kinks at monolayer coverages should be retained. This is confirmed by the results shown in Figure 2, which shows a break-in-slope at $\Delta T' = 40 \pm 5$Å. $\Delta T'$ is a relative reading taken from the quartz crystal thickness monitor and should not be construed as an actual thickness. At a slightly greater exposure than that with the discontinuity in the Auger ratio, the first observation of LEED spots associated with the c(10x2) structure[18,31] were made.

In the initial calibration experiment, both sets of orthogonal domains were observed (Figure 3). The copper crystal used in this and some of the clean Cu(001) photoemission measurements displayed a sharp LEED pattern and the Cu(001) $\bar{M}$ surface state, but was not of specular quality. Subsequently, upon substituting a specular quality Cu(001) crystal, which also displayed a sharp LEED pattern, similar Auger ratios, and the $\bar{M}$ surface state, only one of the two domains was observed. These results were quite reproducible. Test photoemission spectra taken with the crystals clean and with silver adsorbed were essentially the same for both crystals. The absence of the second

domain has been tentatively attributed to the following: as the quality of the crystal preparation improved, deviation of the crystal face from the Cu(001) plane became crucial in breaking the degeneracy of the <110> directions. This type of subtle effect would only be noticeable in a specular crystal. Alignment of a crystal to within $\pm 1^{\circ}$ would still produce steps every 57 atoms. Unlike active gas adsorbates which occupy high symmetry sites, the Ag overlayer is a close packed structure in which the ordering is susceptible to the influences of steps. This effect may very well provide a means of selectively preparing single domain structures and it warrants further investigation.

In terms of its effect upon photoemission, the presence or absence of the second domain is moot. This follows because the photoelectron originates from an electronic environment which is equivalent in either domain, save for easily accountable azimuthal-directional effects.

Samples of known thickness were thus prepared. The one monolayer point was determined with approximately ±10 percent accuracy, but to to include propagation of errors a conservative error estimate of ±20 percent will be quoted for all overlayer thickness values. Thickness estimates from the calibrated quartz microbalance were checked by comparison of Auger ratios and LEED patterns with those found during the calibration. In general, the agreement was fairly good and the sample preparation was reproducible.

C. PHOTOEMISSION RESULTS

The angle-resolved photoemission spectra of clean Cu(001) and slightly over one monolayer of c(10x2)Ag/Cu(001) are shown in Figures 4-9. In Figure 4, the data were collected using s-polarized HeI radiation while rotating off-normal in the (100) plane of Cu(001). The easily observable silver feature near B^F = 5eV disperses to higher binding energy with increasing angle. Note that the feature at $\theta_e = 0^\circ$ is a flat-top, broad peak that could very well be a convolution of two peaks. At θ_e above 10°, another feature is becoming apparent near B^F = 6eV. Also, the $\overline{M}$ surface state of the Cu(001) surface is lost in the c(10x2)Ag/Cu(001) spectra: the lower binding energy side of the copper d-bands shows a significant drop in intensity at the larger angles due to the deposition of the silver. This suggests that the low binding energy side of the Cu d-bands is largely surface-layer derived.

Figure 5 shows the p-polarization spectra collected with HeI radiation, rotating in the (100) plane of Cu(001). The contribution from the 23.1eV satellite of HeI exciting the copper d-bands (apparent B^F near 1eV) is more obvious here than before, and there is significant distortion of the substrate features in the c(10x2)Ag/Cu(001) spectra. Nevertheless, several silver features are easily identifiable. The feature observed near B^F= 5eV in the s-polarized spectra is observed at normal emission and a new lower binding energy peak at B^F= 4.2eV is seen at θ_e= 0° and 10°. Moreover, a dispersive peak is observed at binding energies greater

than 6eV at all angles and another dispersive feature is seen near B^F= 5.5eV at all angles above 20°.

Remaining in the same azimuth but using s-polarized NeI radiation, the spectra in Figure 6 share the simplicity of Figure 4. The broad silver feature near B^F = 5eV again disperses to greater binding energy with increasing θ_e but becomes very weak at larger angles. The exact binding energy of this feature becomes harder to assign. This difficulty is also encountered with the more tightly bound peak with $B^F > 6$eV at θ_e above 13°. Some of the curvature in the clean copper spectra near B^F = 7-9 eV is due to trace Ar in the lamp. ArI(11.7eV) and ArII(13.4ev) could excite the copper d-bands to give peaks at such apparent binding energies. These are also seen at very low kinetic energies in the HeI spectra.

Similar features are also seen in Figure 7, which shows the NeI p-polarized data for the (100) azimuth. Again the copper d-bands are distorted in the adsorbate spectra, but in general it is possible to follow the progress of some of the silver bands, particularly at binding energies greater than 5eV and $\theta_e \geq 26°$. With the exception of the prominent silver feature near 5eV at normal emission, the features in the adsorbate spectra of $\theta_e \leq 26°$ mimic those in the clean Cu(001) spectra. Note, however, the changes in relative intensities that could be due to variation of the mean free path with kinetic energy and possibly to surface resonance coupling of the silver layer and copper bulk. The two silver features at $\theta_e \geq 26°$ are weak but observable at B^F near 5.5eV and at $B^F \geq 6$eV.

Changing azimuths, Figures 8 and 9 contain spectra collected with, respectively, s- and p-polarized HeI radiation, while rotating off-normal in the (110) plane of Cu(001). As above, the s-polarized spectra are simpler and the copper d-bands in the c(10x2) spectra show a shift or drop in intensity on the lower binding energy side, as well as the HeI satellite structure at low binding energies. Note that the only silver feature observed is a prominent peak near $B^F = 5eV$.

Figure 9 has several traceable silver features but also has the worst distortion observed. The combination of refraction, scattering at the interface, energy dependent mean free paths, and possible work function shifts serve to distort the Cu features in the adsorbate spectra. The Cu features disperse quite rapidly in this plane and a misalignment of only 2° could explain the observed shift in features, but the observed behavior could also be caused solely by refractive effects, particularly in light of the progressively dispersing trends in the copper features. Three silver peaks are observed at $\theta_e = 0°$, at binding energies of 4.2eV, near 4.8eV, and at 6.4eV. At 10°, only the peaks at 4.2eV and 6.3eV are seen and at $\theta_e \geq 20°$, peaks near 5.6eV and at $B^F > 6eV$ are seen.

Because angle-resolved photoemission is susceptible to these distorting factors, direct subtraction of background spectra alone proved to be inadequate. However, ARP allows the actual resolution of separate features, and the background Cu(001) spectra serve as a guide to eliminate substrate peaks, allowing unambiguous assignment of features to the Ag overlayer. Thus, in general, the only Ag features

lost were those that overlap with the Cu d-bands.

The clean Cu(001) spectra taken with HeI (21.22eV) and the first copper crystal had a spectrometer work function with a standard deviation of 4.46±0.04eV. Clean Cu(001) spectra taken with NeI (16.85eV) and the second copper crystal exhibited a spectrometer work function of 4.50±0.06eV. The Ag/Cu(001) monolayer data, all collected with the second crystal and with both HeI and NeI, had a spectrometer work function of 4.51±0.05eV. These are determinations made using p-polarized light: the s-polarized spectra tended to have much smaller intensity increases at the Fermi level and, while the values were consistent with the above, they were also of much lower precision and reliability. The above average values were used in measuring binding energies.

To provide an independent method of confirming the assignments derived from Figures 4-9, spectra were also collected from higher coverage samples. An exposure of 2.5 monolayers of silver produced a surface that also displayed a single c(10x2) LEED pattern. Photoemission spectra from this sample are shown in Figure 10. These were observed with HeI radiation while rotating in the (100) plane of Cu(001), using s- and p-polarized light in separate measurements. The silver features are correspondingly stronger and the residual copper features distorted and weaker, in agreement with with the previous assignments. (In the synchrotron radiation experiment described in Chapter III,[9] normal emission spectra were collected from samples ranging in exposure from 1/2 to 5 monolayers. These were also

consistent with the above resonance lamp spectra.)

In Figure 11, derived energies of all of the observed silver features from the monolayer samples are plotted versus the parallel component of the crystal momentum, $k_{(x,y)}$. The scheme used to calculate these values will be discussed in detail in Section D, but briefly it should be noted that to calculate $k_{(x,y)}$, the values of ϕ_{AN} from above and ϕ = 4.74 eV (Ref. 32 for Ag(111)) were used. An upper limit of ϕ would be ϕ = 5.16 eV from Cu(001).[33] A lower limit can be estimated from ϕ = 4.3eV from Ref. 32 for Ag. Thus a reasonable estimation of $\phi_{AN}-\phi$ would be $-0.2(5)$ eV, which would contribute up to a four percent uncertainty to $k_{(x,y)}$.

Before making any attempt at assignment of the individual bands in the Ag 2-dimensional Surface Brillouin Zone (SBZ), we note that there are four separate bands observed in Figure 11, which are labelled i through iv, starting with the most tightly bound. Some of these disperse as functions of the parallel component of the crystal momentum, $k_{(x,y)}$, and none show any significant dependence upon the perpendicular component of the crystal momentum, k_z. (These bands are organized separately by polarization dependence in Tables I through IV, ignoring any avoided band-crossings. Table V contains all of the normal emission B^F data for Band iii, p- and s-polarization.) The worst disagreement between measurements with different values of k_z is at $k_{(x,y)} \geq 0.8\text{Å}^{-1}$ in the <100> surface direction, in the data taken with s-polarized light. The NeI peaks seem to be dispersing downward more rapidly than the HeI data.

As mentioned above, at larger angles the NeI features are quite weak and more difficult to locate precisely. Considering the 4 percent uncertainty in $k_{(x,y)}$ from the work function estimates and the full-width-half- maximum (FWHM) experimental resolution of 120meV, these data are still in reasonably good agreement. (There is also the possibility that Band ii is contributing as well due to a breakdown of selection rules, as will be discussed in Section III.) This is conclusive evidence that the Ag overlayer is effectively isolated from the Cu substrate in terms of the valence d-band dispersion relations. It is of interest that Bands ii and iii would cross at the zone boundary Z, except that at Z both bands are of the same symmetry and must have an avoided crossing. Also, there is a strong similarity between the bands in the two directions taken through the SBZ. Dispersion relations and band symmetries will be derived in the next Section, after reviewing the relevant group-theoretical basis for interpreting the spectra.

Interestingly, these off-normal bandmapping results are distinctly different from those observed using synchrotron radiation at $h\nu$ =14 and 21eV impinging upon the (111) face of a silver crystal (for which k_z is a good quantum number) under analogous conditions and in the same apparatus, as can be seen in Chapter IV, Figure 8 (Ref. 34). The two-dimensionality observed here is quite similar to that found in a surface enriched alloy crystal by Heimann et al.[35]

As a check of our thickness estimates, photoemission intensities of the silver and copper features were compared. Intensities were

estimated by fitting with gaussians and a quadratic background and by a method of background subtraction using the clean Cu(001) spectra. To minimize band and refractive effects, only the normal emission data were used. In going from one to 2.5 monolayer exposure, the Ag/Cu photoemission ratio increases by a factor of 3. A simple model of the photoemission intensities would be to assume that the silver intensity is proportional to exposure at low exposures and that the copper intensity would be that of the clean surface attenuated by the overlayer by a factor of $e^{-z/z'}$, with z the film thickness assuming layer-by-layer growth and z' the escape depth of the copper valence electrons through the silver film at normal emission. Assuming a thickness of 2Å per silver monolayer and an escape depth of 10Å for the copper electrons (from the Universal Curve[36]) an increase of a factor of 3.4 is predicted in going from one to 2.5 monolayers. A slightly superior model derived in Chapter II, Appendix 1 using a monolayer thickness of 2.5Å predicts a ratio of 3.1 for an escape depth of 10Å and a ratio Of 2.9 for an escape depth of 15Å. This is quite reasonable agreement, considering the extent of the approximations made.

D. DISCUSSION

The energy and momentum resolving capability of angle-resolved photoemission (ARP) allows a direct measurement of the dispersion relations of the valence bands, i.e., the functional dependence of the energy upon the electron crystal momentum. This is based upon the momentum and energy conservation implicit in the direct transition

model[37] (DTM). Energy conservation requires:

$$h\nu = B^F + KE + \phi = B^F + KE_{AN} + \phi_{AN} \quad (1)$$

where $h\nu$ is the photon energy, B^F is the binding energy with respect to the Fermi level, KE (KE_{AN}) is the external kinetic energy of the escaping electron with respect to the vacuum (analyzer) and ϕ (ϕ_{AN}) is the true (analyzer or spectrometer) work function. The Fermi level is a convenient and accurate reference in ARP and the work function is the difference between the Fermi and vacuum reference levels. The kinetic energy can be expressed in terms of the external momentum of the electron, q,

$$KE = \frac{(h/2\pi)^2 q^2}{2m} \quad (2)$$

Conservation of momentum requires

$$\underline{k}_f = \underline{k}_i + \underline{k}_{h\nu} + \underline{g} \cong \underline{k}_i + \underline{g} \quad (3)$$

where $\underline{k}_f$ and $\underline{k}_i$ are the final state and initial state crystal momenta of the electron, $\underline{k}_{h\nu}$ is the photon momentum, which in this photon energy range is negligible, and $\underline{g}$ is a reciprocal lattice vector. Primary cone emission will be assumed throughout this work.[38] Defining the z-axis as perpendicular to the surface and the x- and y-axes in the surface, each of the crystal momenta and the external momentum can be expressed as a vector sum of components parallel (x,y) and perpendicular (z) to the surface of the crystal.

$$\underline{k}_f = \underline{k}_{f,z} + \underline{k}_{f,(x,y)} \tag{4}$$

$$\underline{k}_i = \underline{k}_{i,z} + \underline{k}_{i,(x,y)} \tag{5}$$

$$\underline{q} = \underline{q}_z + \underline{q}_{(x,y)} \tag{6}$$

The external momentum, $\underline{q}$, and the crystal momentum, $\underline{k}_f$, are related in magnitude by the inner potential, V_0, which is the sum of the work function, ϕ, and the Fermi energy, E_F:

$$\frac{(h/2\pi)^2 k_f^2}{2m} - \frac{(h/2\pi)^2 q^2}{2m} = V_0 = E_F + \phi \tag{7}$$

Moreover, since the break in symmetry at the surface is only along the direction perpendicular to the surface, it is possible to separate the effects of the potential change upon the components of the momenta:

$$\frac{(h/2\pi)^2 k_{f,z}^2}{2m} - \frac{(h/2\pi)^2 q_z^2}{2m} = V_0 \tag{8}$$

$$\underline{k}_{f,(x,y)} = \underline{q}_{(x,y)} \tag{9}$$

where it is assumed that no surface umklapping is occurring. This is reasonable since the magnitude of the parallel components of the momenta that will be observed in this experiment will, in general, be much smaller than any available surface reciprocal lattice vector.

The ultimate goal of this experiment is to determine the dependence of the binding energy of the silver valence states upon the initial state crystal momentum:

$$B^F = B^F\ (\underline{k}_{i,z} + \underline{k}_{i,(x,y)}) \qquad (10)$$

If the metal overlayer is truly an isolated two-dimensional system, the B^F will be independent of $\underline{k}_{i,z}$. If there is strong coupling of the Ag and Cu, then the B^F would depend upon both $\underline{k}_{i,(x,y)}$ and $\underline{k}_{i,z}$. The most direct method to determine this is to perform a series of ARP measurements at normal emission and rotating the analyzer off-normal, thus varying $\underline{k}_{i,(x,y)}$. If this is done at two significantly different photon energies, in this case, HeI (21.22 eV) and NeI (16.8 eV), it is possible to map the B^F as a function of $\underline{k}_{i,(x,y)}$ with two different sets of $\underline{k}_{i,z}$. This task is simplified by beginning at the center of the Surface Brillouin Zone (SBZ), i.e., normal emission, and moving outward toward the SBZ boundaries. In this manner, the parallel component of the reciprocal lattice vector of equation (3) can be assumed to be zero, at least for angles near normal emission. Thus,

$$\underline{k}_{i,(x,y)} = \underline{k}_{f,(x,y)} = \underline{q}_{(x,y)} = \underline{q}\,[\sin(\theta_e)] \qquad (11)$$

where θ_e is the polar angle of emission, measured from the surface normal, and q can be determined from equations (1) and (2), using KE_{AN}, ϕ_{AN} and ϕ. A knowledge of V_0 and the final state is necessary to calculate $k_{f,z}$.

Next, it will be shown that by using a simple model of a hexagonal-close-packed layer and treating the Cu(001) substrate as an averaged flat surface, all of the observed features in

c(10x2)Ag/Cu(001) can be explained in terms of Ag4d(L=2) and Ag5s(L=0) electrons.

Without any knowledge of the specifics of the potential above, save its symmetry, it is immediately recognizable that C_{6v} symmetry exists at the zone center, $\bar{\Gamma}$, where $k_{(x,y)} = 0$, and that C_S symmetry holds along the $\bar{\Gamma}-\bar{M}$ and $\bar{\Gamma}-\bar{K}$ lines in the 2-D SBZ, with $k_{(x,y)} > 0$. It is less obvious but reasonable to expect a C_S symmetry to be approximately accurate along $\bar{\Gamma}-\bar{Z}$, at least near $\bar{\Gamma}$ (Figure 3). (The copper beneath the silver monolayer breaks the symmetry in the z-direction.) The C_S symmetry implies a significant degree of delocalization: if the valence electrons are localized on the central atom to the extent that the only important perturbation of the atomic potential is due to nearest neighbors, then all emission angles will exhibit C_{6v} symmetry selection rules.

The next major question regards the relative importance of crystal-field and spin-orbit splitting. In bulk Ag(111),[24] the two contributions are of the same order of magnitude: 10 Dq = .865 ± .027 eV and $\xi(4d)$ = .232 ± .011, which is also quite close to the atomic value $\xi(4d)$ = .224 eV.[39] However, this is somewhat misleading, since bulk Ag(111) has octahedral symmetry and the overlayer has hexagonal C_{6v}: the reduction in symmetry would be expected to increase the size of the crystal field term splitting. In a crude sort of way, it can be viewed as a comparison of spherical and $C_{\infty v}$ symmetries: all of the spherial harmonics of a given L value are degenerate in a spherical potential but L = 2 atomic states fall

in different representations in $C_{\infty v}$. Nevertheless, both single (no spin) and double groups (spin) were included in the analysis for completeness, with consideration given to the different regimes associated with various relative sizes of spin-orbit and crystal-field splittings.

Consider now the symmetry of the matrix element corresponding to the photoelectron excitation:

$$M_{if} = \langle f] \underline{O} [i\rangle \tag{12}$$

$$\underline{O} = (\underline{A} \cdot \underline{p}) + (\underline{p} \cdot \underline{A}) \tag{13}$$

where $\underline{A}$ and $\underline{p}$ are operators, the electromagnetic vector potential and electron momentum, respectively. The surface breaks the z-direction symmetry so that $[\underline{A}, \underline{p}] \neq 0$, but a common approximation is to assume the commutator is zero. Actually, if both the initial and final states are eigenfunctions of momentum then even this approximation is unnecessary. Ignoring the complication imposed upon $\underline{A}$ by the surface and assuming at least one of the initial or final states as an momentum eigenstate, the following approximation should hold:

$$M_{if} = \langle f] \underline{A} [i\rangle \cdot \underline{p} \tag{14}$$

with $\underline{A}$ being treated as the polarization of the light in free space. It is known[40,41] that the overall symmetry representation of M_{if} is A_1, the completely symmetric representation. Moreover, if the single (double) group representation is used, $\langle f]$ must have A_1

($D_{1/2}$) symmetry. ($D_{1/2}$ is the most symmetric of all double group representations and $A_1 \times D_{1/2} = D_{1/2}$.) Thus, $\Gamma_f \times \Gamma_0 \times \Gamma_i$ must contain A_1 to have a non-zero matrix element and Γ_f is already determined. By using a polarized light source, Γ_0 is well defined and can be varied at will to selectively excite different initial states. $\underline{A}$ is treated as the polarization vector and, as such, has a representation which is the sum of the representations of its cartesian components. Now it is possible to work backward to predict which initial states will have non-zero matrix elements for a given polarization. (Note that the assumption that the configuration is $4d^9 5s^2$ is necessary only if the spin-orbit plays a dominant role (Ref. 24).)

The single group analysis will be discussed first. In the single group representation, <f] is in A_1, so that $\Gamma_0 \times \Gamma_i$ must contain A_1 for M_{if} to be nonzero. Consider first the s-polarized excitation: $\underline{A}_s = \underline{A}_{s,(x,y)}$; that is, s-polarized light has no component perpendicular to the surface and, moreover, is aligned such that it is perpendicular to the plane containing outgoing off-normal electrons. Thus it is within the E_1 representation in C_{6v} and A" representation in C_s. This implies that only initial states of E_1 (C_{6v}) and A" (C_s) could have non-zero matrix elements with s-polarized light. For p-polarization, $\underline{A}_p = \underline{A}_{p,z} + \underline{A}_{p,(x,y)}$ and is aligned such that it is in the same plane containing the electrons collected off-normal. For normal emission, $\underline{A}_{p,z}$ is of $A_1(C_{6v})$; $\underline{A}_{p,(x,y)}$ transforms as $E_1(C_{6v})$. Off-normal, $\underline{A}_p$

belongs to $A'(C_S)$. Hence, only $A_1(C_{6v})$ and $E_1(C_{6v})$ states could be seen at normal emission, p-polarization and only $A'(C_S)$ could be seen with $\underline{A}_p$, off-normal.

However, it must be remembered that in terms of relative intensities, $\underline{A}\cdot\underline{p}$ alignment favors $\underline{A}_{p,z}$ at normal emission and $\underline{A}_{p,(x,y)}$ at emission far off normal. $\underline{A}_s \cdot \underline{p} = 0$ in all cases, if treated as vectors instead of operators.

Consider now normal emission. Since $k_{(x,y)} = 0$, this is the center of the Surface Brillouin Zone and, moreover, atomic effects will dominate here.[24] Thus, it is useful to think in terms of the spherical harmonics and linear combinations of such. Only Band iii of Figure 11 shows any intensity at normal emission with s polarized light. (See Figures 4, 6 and 8.) This strongly suggests that Band iii transforms as the $E_1(C_{6v})$ representation and has basis functions composed of $Y_2^{\pm 1}$ spherical harmonics. There are two bands, i and iv, which have intensity with $\underline{A}_p$ but none with $\underline{A}_s$: this implies that $\underline{A}_z$ is important and that these bands are in the $A_1(C_{6v})$ representation. Basis functions could include Y_2^o and Y_o^o. Considering their relative placement and the precedent of the assignments in 3-dimensional Ag(111),[24] Band i appears to be Y_o^o (s-electrons) and band iv is Y_2^o, of $A_1(C_{6v})$ representation, at the center of the SBZ. Band ii has no intensity at normal emission but is seen off normal: this suggests an assignment of $Y_2^{\pm 2}$ of the $E_2(C_{6v})$ representation.

Of course, these assignments must be consistent with the observed

behavior off normal. Band i is $A_1(C_{6v})$ which becomes $A'(C_S)$ and should be seen only with $\underline{A}_p$; Band ii is $E_2(C_{6v})$ which splits into $A'(C_S)$ and $A''(C_S)$ which should be seen with only $\underline{A}_p$ and $\underline{A}_s$, respectively; Band iii is $E_1(C_{6v})$ which also splits into $A'(C_S)$ and $A''(C_S)$ which again should only be observed only with $\underline{A}_p$ and $\underline{A}_s$, respectively; Band iv is $A_1(C_{6v})$ which becomes $A'(C_S)$ and should be seen only with $\underline{A}_p$. However, the splittings of Bands ii and iii are not observed. The bands continue to exhibit behavior consistent with C_{6v} symmetry effects as the emission direction is rotated off-normal, even for Bands ii and iii. It seems that the C_S perturbation to the C_{6v} potential, or alternatively the degree of delocalization, is sufficient to break the selection rule forbidding the $E_2(C_{6v})$ initial state transitions with p-polarized light and that the C_S perturbation favors the s-polarized excited transition for Band iii. Both of these suggest that the initial state is still dominated by C_{6v} effects but that the C_S perturbation now distinguishes between in plane (p) and out of plane (s) polarization. The modified C_{6v} selection rules hold exactly in the <110> direction and generally in the <100> direction but near the boundary in the <100> direction they break down. By then the C_S approximation is inappropriate (it is C_1 at $\bar{Z}$) and $\underline{A}\cdot\underline{p}$ alignment becomes the dominant effect.

Thus a single group analysis, with the crystal-field dominating over spin-orbit effects, is capable of explaining all of the features observed. But if this is correct, then it should be possible to see

spin-orbit splitting of at least some of the states at $\bar{\Gamma}$, where localized atomic effects, as opposed to delocalized band effects, dominate.

More precisely, Y_2^0 and Y_0^0 will not be split, $Y_2^{\pm 2}$ is not observed but $Y_2^{\pm 1}$ (Band iii) should show splitting at $\bar{\Gamma}$. (See Appendix 1.) Careful examination of this feature, the 0° peak at B^F near 4.8eV in Figures 4-9, shows that it is a broad, flat-top peak, suggestive of two convoluted peaks. Peak position estimates made by fitting with two lorentzians and a linear background exhibited a splitting of 0.27(6) eV. Table V contains the fitting data and a summary of peak positions obtained by visual inspection, which produced a spin-orbit splitting of 0.20(5) eV. The average of the two methods is 0.24(6) eV.

Since the splitting of $Y_2^{\pm 1}$ states would be equal to ξ, the spin orbit splitting parameter, $\xi(4d)$-2D = 0.24(6) eV. This agrees reasonably well with the atomic (0.224 eV, Ref. 39) and bulk Ag(111) (0.232 eV, Ref. 24) values.

The use of double groups leads to similar selection rules but no easily identifiable correspondence between observed polarization dependence and symmetry selection rules is observed if it is assumed that spin orbit effects dominate crystal field at $\bar{\Gamma}$. Moreover, discrepancies between predicted and observed behavior occur off normal: e.g., all states should be observable with s and p polarized light if double groups are used in C_S.

It must also be noted that the bulk Ag(111) octahedral potential

is of such high symmetry that only two double group representations are used for the d-bands (Bands 2-6 at Γ in Ag(111))in any case of relative contribution from spin-orbit and crystal-field splitting and that no band crossings are required to go from one extreme to the other. On the other hand, the symmetry is much reduced in the C_{6v} potential and there are many possible representations. This would serve to limit first order perturbative mixing of states, owing to the restriction that they be of the same representation. This appears to have the effect of reducing the impact of the spin-orbit induced mixing and contributing to the validity of the single group analysis.

Considering the effect of the six in-plane neighbors in a ligand-field scheme, it should be possible to independently predict the ordering of the C_{6v} states of L = 2 origin and to scale splittings from the known bulk value of Ag(111). By performing a Taylor expansion[42] of the Coulombic potential (Appendix 2) associated with the nearest neighbors in a FCC octahedral lattice and C_{6v} hexagonal plane, the following expression for the effective potentials can be found. (See Appendices 2 and 3 for details.)

$$V_{\substack{FCC \\ OCT}} = -\frac{35}{8}\frac{e}{a^5}\left(\frac{-3}{5}r^4 + x^4 + y^4 + z^4\right) , \tag{15}$$

$$V_{HEX} = -\frac{3}{2}\frac{e}{a^3}(3z'^2 - r^2), \tag{16}$$

where e is the charge of an electron, a is the nearest neighbor distance, and $\underline{x}$ = [100], $\underline{y}$ = [010], $\underline{z}$ = [001] in (15) and $\underline{z}'$ = [111]

of bulk Ag in (16). Calculating the first order expectation values for the E_g and T_{2g} states of Ag(111) and the states of the Ag hexagonal layer, the ordering and splitting shown in Figure 12 were obtained.

The most important point is that the ordering agrees perfectly with that found spectroscopically. Also, the total splitting in the hexagonal case should be larger than in the octahedral, because $\langle r^2\rangle/a^2$ should be greater than $\langle r^4\rangle/a^4$. This supports the assertion made earlier in favor of large splittings and the appropriate nature of single groups for the hexagonal system.

The experimentally observed splittings were found to be $\Delta(Y_2^0-Y_2^{\pm1}) = 0.6$eV and $\Delta(Y_2^{\pm1}-Y_2^{\pm2}) = 1.0$eV, where the $Y_2^{\pm2}$ value of $B^F = 5.7$eV was extrapolated from off normal measurements. An attempt was made to predict the splittings by scaling off the previously measured bulk Ag(111) crystal field splitting of 10Dq = 0.865 eV. However, it is necessary to have a knowledge of the ratio of $\langle r^2\rangle_{\text{monolayer}}$ to $\langle r^4\rangle_{\text{Ag(111)}}$. The use of relativistic Hartree-Fock-Slater atomic expectation values[43] for each of these produced unphysical splittings that were an order of magnitude too large. By assuming that $\langle r^2\rangle/a^2$ approximately equals $\langle r^4\rangle/a^4$ it is possible to obtain reasonable values, but only qualitative arguments exist to support this assertion. Obviously, a quantitative evaluation must wait for an exact theoretical analysis which includes a calculation of radial wavefunctions and expectation values.

Finally, these polarization-dependent angle-resolved photoemission results agree qualitatively with those found for polycrystalline thin films of Ag using angle integrated photoemission.[44]

E. CONCLUSIONS

It has been shown by angle resolved photoemission that the d-bands of a monolayer of c(10x2)Ag/Cu(001) behave 2-dimensionally. The electronic valence bands of the silver monolayer clearly show dispersion in the overlayer plane ($k_{(x,y)}$) and a lack of dispersion in the direction along the surface normal (k_z). The experimental photoemission features can be assigned upon the basis of C_{6v} selection rules and the use of single group representations. Delocalization of the 4d electrons is sufficient to produce two-dimensional dispersion but in general the cross sections are dominated by nearest neighbor symmetry perturbation. This is consistent with the previous observation of the importance of atomic cross section effects in bulk Ag.[45] A simple model predicts accurately the observed ordering of the L = 2 states but a quantitative analysis is not possible at this time. The spin-orbit splitting parameter is found to agree reasonably well with those observed in atomic and bulk systems.

APPENDIX 1

Spin Orbit Splitting Perturbation of $l = 2$ States in a C_{6V} Crystal Field Potential

The general plan is to first generate the total angular momentum states ($[j\ m_j >$) as linear combinations of the products of angular orbital momentum, $[l\ m_l >$, and spin angular momentum, $[s\ m_s >$, states, then rearrange so as to describe the ls states as sums of the j states and finally calculate the first order perturbation due to spin orbit. An implicit assumption here is that the spin orbit splitting is small and the symmetry of the states complicated so that the crystal field splitting remains dominant. Note that in this case, $l = 2$, $s = 1/2$ and $j = 5/2$ or $3/2$ and that $[l\ m_l\ s\ m_s > = [l\ m_l > [s\ ,_s >$.

It can be easily shown that the following j states can be described as linear combinations of the products of l and s states. Note the orthonormality of the states.

$$[5/2,\ 5/2 > = [2,\ 2,\ 1/2,\ 1/2 >$$

$$[5/2,\ 3/2 > = (4/5)^{1/2}\ [2,\ 1,\ 1/2,\ 1/2 > + (1/5)^{1/2}\ [2,\ 2,\ 1/2,\ -1/2 >$$

$$[5/2,\ 1/2 > = (3/5)^{1/2}\ [2,\ 0,\ 1/2,\ 1/2 > + (2/5)^{1/2}\ [2,\ 1,\ 1/2,\ -1/2 >$$

$$[5/2,\ -1/2 > = (2/5)^{1/2}\ [2,\ -1,\ 1/2,\ 1/2 > + (3/5)^{1/2}\ [2,\ 0,\ 1/2,\ -1/2 >$$

$$[5/2,\ -3/2 > = (1/5)^{1/2}\ [2,\ -2,\ 1/2,\ 1/2 > + (4/5)^{1/2}\ [2,\ -1,\ 1/2,\ -1/2 >$$

$$[5/2,\ -5/2 > = [2,\ -2,\ 1/2,\ -1/2 >$$

$[3/2, 3/2 > = (1/5)^{1/2} [2, 1, 1/2, 1/2 > - (4/5)^{1/2} [2, 2, 1/2, -1/2 >$

$[3/2, 1/2 > = (2/5)^{1/2} [2, 0, 1/2, 1/2 > - (3/5)^{1/2} [2, 1, 1/2, -1/2 >$

$[3/2, -1/2 > = (3/5)^{1/2} [2, -1, 1/2, 1/2 > - (2/5)^{1/2} [2, 0, 1/2, -1/2 >$

$[3/2, -3/2 > = (4/5)^{1/2} [2, -2, 1/2, 1/2 > - (1/5)^{1/2} [2, -1, 1/2, -1/2 >$

In a C_{6V} potential, the $[l = 2, \pm m >$ states are of different representations and, as shown in the text and Appendices 2 and 3, split. $Y_{l=2}^{m=\pm 2}$ states are of E_2, $Y_{l=2}^{m=\pm 1}$ are of E_1, and $Y_{l=2}^{m=0}$ is of A_1 representation. Rearranging the equations above, it is possible to express the $[l = 2, m_l, s = 1/2, m_s >$ states as sums of $[j, m_j >$.

E_2 representation: $Y_2^{\pm 2}$

$[2, 2, 1/2, 1/2 > = [5/2, 5/2 >$

$[2, 2, 1/2, -1/2 > = (1/5)^{1/2} [5/2, 3/2 > - (4/5)^{1/2} [3/2, 3/2 >$

$[2, -2, 1/2, 1/2 > = (1/5)^{1/2} [5/2, -3/2 > + (4/5)^{1/2} [3/2, -3/2 >$

$[2, -2, 1/2, -1/2 > = [5/2, -5/2 >$

E_1 representation: $Y_2^{\pm 1}$

$[2, 1, 1/2, 1/2 > = (4/5)^{1/2} [5/2, 3/2 > + (1/5)^{1/2} [3/2, 3/2 >$

$[2, 1, 1/2, -1/2 > = (2/5)^{1/2} [5/2, 1/2 > - (3/5)^{1/2} [3/2, 1/2 >$

$[2, -1, 1/2, 1/2 > = (2/5)^{1/2} [5/2, -1/2 > + (3/5)^{1/2} [3/2, -1/2 >$

$[2, -1, 1/2, -1/2 > = (4/5)^{1/2} [5/2, -3/2 > - (1/5)^{1/2} [3/2, -3/2 >$

A_1 representation: Y_2^0

$[2, 0, 1/2, 1/2 > = (3/5)^{1/2} [5/2, 1/2 > + (2/5)^{1/2} [3/2, 1/2 >$

$[2, 0, 1/2, -1/2 > = (3/5)^{1/2} [5/2, -1/2 > - (2/5)^{1/2} [3/2, -1/2 >$

Again, note the orthonormality of the states.

The perturbation is proportional to the dot product of the orbital and spin angular momenta, which can be expressed in terms of J^2, L^2 and S^2 and j, l and s

$$\underline{J} = \underline{L} + \underline{S}$$

$$J^2 = L^2 + S^2 + 2 (\underline{L} \cdot \underline{S})$$

$$\underline{L} \cdot \underline{S} = \frac{J^2 - L^2 - S^2}{2}$$

$$H = \xi (\underline{L} \cdot \underline{S}) = (\xi /2) [J^2 - L^2 - S^2]$$

Since the states are eigenstates of $\underline{J}$, $\underline{L}$, and $\underline{S}$:

$$H = (\xi /2)[j(j + 1) - l(l + 1) - s(s + 1)] (h/2\pi)^2$$

In this case l = 2 and s = 1/2:

$$H = (\xi /2)[j(j + 1) - (27/4)](h/2\pi)^2 = (\xi /2)[j(j + 1) - (27/4)]$$

(treating $h/2\pi$ as unity).

An important aspect of degenerate perturbation theory is the mixing of states due to the perturbation. For the states to mix, they must have non-zero off-diagonal matrix elements for the perturbation Hamiltonian. If the states were not already split by the crystal field Hamiltonian, mixing of the $[l, m_l, s, m_s >$ states would be very strong. However, since the C_{6V} crystal field splits the states into different representations and it is assumed that the crystal field splitting is significantly larger than the spin orbit perturbation, each representation manifold will be considered separately. Within a given representation manifold, there are no non-zero off-diagonal matrix elements. Hence, the first order perturbation correction is the expectation value or diagonal matrix element of each $[l = 2, m_l, s = 1/2, m_s >$ state.

E_2 representation: $Y_2^{\pm 2}$

$< 2, 2, 1/2, 1/2] (\underline{L} \cdot \underline{S}) [2, 2, 1/2, 1/2 > = 1$

$< 2, 2, 1/2, -1/2] (\underline{L} \cdot \underline{S}) [2, 2, 1/2, -1/2 > = -1$

$< 2, -2, 1/2, 1/2] (\underline{L} \cdot \underline{S}) [2, -2, 1/2, 1/2 > = -1$

$< 2, -2, 1/2, -1/2] (\underline{L} \cdot \underline{S}) [2, -2, 1/2, -1/2 > = 1$

Spin orbit shift	$\Delta E_{shift} = \pm 1 \xi$
Spin orbit splitting	$\Delta E_{split} = 2 \xi$

E_1 representation: $Y_2^{\pm 1}$

$< 2, 1, 1/2, 1/2] (\underline{L} \cdot \underline{S}) [2, 1, 1/2, 1/2 > = 1/2$

$< 2, 1, 1/2, -1/2] (\underline{L} \cdot \underline{S}) [2, 1, 1/2, -1/2 > = -1/2$

$< 2, -1, 1/2, 1/2] (\underline{L} \cdot \underline{S}) [2, -1, 1/2, 1/2 > = -1/2$

$< 2, -1, 1/2, -1/2] (\underline{L} \cdot \underline{S}) [2, -1, 1/2, -1/2 > = 1/2$

Spin orbit shift	$\Delta E_{shift} = \pm 1/2\, \xi$
Spin orbit splitting	$\Delta E_{split} = 1\, \xi$

A_1 representation: Y_2^0

$< 2, 0, 1/2, 1/2] (\underline{L} \cdot \underline{S}) [2, 0, 1/2, 1/2 > = 0$

$< 2, 0, 1/2, -1/2] (\underline{L} \cdot \underline{S}) [2, 0, 1/2, -1/2 > = 0$

Spin orbit shift	$\Delta E_{shift} = 0$
Spin orbit splitting	$\Delta E_{split} = 0$

APPENDIX 2

Taylor Series Expansion of the Coulombic Potential and its Application to Planar Hexagonal, Simple Cubic, and Face Centered Cubic-Octahedral Symmetry Potentials

By using a Taylor series expansion of the Coulombic potential, it is possible to make use of the high symmetry of close packed systems such as planar hexagonal, simple cubic (SC) and face centered cubic (FCC) to allow cancellation of many terms and the isolation of the dominant high symmetry contribution to the potential.

First the Coulombic potential:

$V = q/r = e/r$

which in this case has $q = e$, because the nearest neighbor metal atoms are treated as +1 cations. [Atomic Ag has a configuration of $[Kr]\ 3d^{10}\ 4s^{1}$.]

A Taylor series expansion in the three dimensions for a function $f(x, y, z)$

$$f(x_1+ h, y_1+ k, z_1+ l) = \sum_{n=0}^{\infty} \frac{\left[h \frac{\partial}{\partial x} + k \frac{\partial}{\partial y} + l \frac{\partial}{\partial z}\right]^n}{n!} f(x, y, z) \Bigg|_{\substack{x = x_1 \\ y = y_1 \\ z = z_1}}$$

substituting $f(x, y, z) = \frac{1}{r} = \frac{1}{(x^2 + y^2 + z^2)^{1/2}}$,

i.e., the ion center at (0, 0, 0) and then changing $x_1 \to x$, $y_1 \to y$

and $z_1 \to z$:

0th $$\frac{1}{(x^2 + y^2 + z^2)^{1/2}}$$

1st $$-(hx + ky + lz)(x^2 + y^2 + z^2)^{-3/2}$$

2nd $$-(1/2)(h^2 + k^2 + l^2)(x^2 + y^2 + z^2)^{-3/2}$$
$$+(3/2)(hx + ky + lz)^2 (x^2 + y^2 + z^2)^{-5/2}$$

3rd $$(3/2)(x^2 + y^2 + z^2)^{-5/2} (h^2 + k^2 + l^2)(hx + ky + lz)$$
$$-(5/2)(hx + ky + lz)^3 (x^2 + y^2 + z^2)^{-7/2}$$

4th $$(3/8)(x^2 + y^2 + z^2)^{-5/2} (h^2 + k^2 + l^2)^2$$
$$-(15/4)(x^2 + y^2 + z^2)^{-7/2} (h^2 + k^2 + l^2)(hx + ky + lz)^2$$
$$+(35/8)(x^2 + y^2 + z^2)^{-9/2} (hx + ky + lz)^4$$

5th $$-(15/8)(x^2 + y^2 + z^2)^{-7/2} (h^2 + k^2 + l^2)^2 (hx + ky + lz)$$
$$+(35/4)(x^2 + y^2 + z^2)^{-9/2} (h^2 + k^2 + l^2)(hx + ky + lz)^3$$
$$-(63/8)(x^2 + y^2 + z^2)^{-11/2} (hx + ky + lz)^5$$

6th $$-(5/16)(x^2 + y^2 + z^2)^{-7/2} (h^2 + k^2 + l^2)^3$$
$$+(105/16)(x^2 + y^2 + z^2)^{-9/2} (h^2 + k^2 + l^2)^2 (hx + ky + lz)^2$$
$$-(315/16)(x^2 + y^2 + z^2)^{-11/2} (h^2 + k^2 + l^2)(hx + ky + lz)^4$$
$$+(231/16)(x^2 + y^2 + z^2)^{-13/2} (hx + ky + lz)^6$$

The above results are for an ion centered at (0, 0, 0). To generalize for an ion centered at (a_1, b_1, c_1), substitute $x \to (x - a_1)$, $y \to (y - b_1)$, $z \to (z - c_1)$.

0th $$\frac{1}{[(x - a_1)^2 + (y - b_1)^2 + (z - c_1)^2]^{1/2}}$$

1st $$- [h(x - a_1) + k(y - b_1) + l(z - c_1)] [(x - a_1)^2 + (y - b_1)^2 + (z - c_1)^2]^{-3/2}$$

2nd $$-(1/2)(h^2 + k^2 + l^2) [(x - a_1)^2 + (y - b_1)^2 + (z - c_1)^2]^{-3/2}$$
$$+(3/2)[h(x - a_1) + k(y - b_1) + l(z - c_1)]^2 [(x - a_1)^2 + (y - b_1)^2 + (z - c_1)^2]^{-5/2}$$

3rd $$(3/2)[(x - a_1)^2 + (y - b_1)^2 + (z - c_1)^2]^{-5/2} (h^2 + k^2 + l^2) [h(x - a_1) + k(y - b_1) + l(z - c_1)]$$
$$-(5/2)[h(x - a_1) + k(y - b_1) + l(z - c_1)]^3 [(x - a_1)^2 + (y - b_1)^2 + (z - c_1)^2]^{-7/2}$$

4th $$(3/8)[(x - a_1)^2 + (y - b_1)^2 + (z - c_1)^2]^{-5/2} (h^2 + k^2 + l^2)^2$$
$$-(15/4)[(x - a_1)^2 + (y - b_1)^2 + (z - c_1)^2]^{-7/2} (h^2 + k^2 + l^2) [h(x - a_1) + k(y - b_1) + l(z - c_1)]$$
$$+(35/8)[(x - a_1)^2 + (y - b_1)^2 + (z - c_1)^2]^{-9/2} [h(x - a_1) + h(y - b_1) + l(z - c_1)]^4$$

5th $$-(15/8)[(x - a_1)^2 + (y - b_1)^2 + (z - c_1)^2]^{-7/2} (h^2 + k^2 + l^2)^2 [h(x - a_1) + k(y - b_1) + l(z - c_1)] +(35/4)[(x - a_1)^2 + (y - b_1)^2 + (z - c_1)^2]^{-9/2} (h^2 + k^2 + l^2) [h(x - a_1) + h(y - b_1) + l(z - c_1)]^3 -(63/8)[(x - a_1)^2 + (y - b_1)^2 + (z - c_1)^2]^{-11/2} [h(x - a_1) + k(y - b_1) + l(z - c_1)]^5$$

6th $$-(5/16)[(x - a_1)^2 + (y - b_1)^2 + (z - c_1)^2]^{-7/2} (h^2 + k^2 + l^2)^3 +(105/16)[(x - a_1)^2 + (y - b_1)^2 + (z - c_1)^2]^{-9/2} (h^2 + k^2 + l^2)^2 [k(x - a_1) + k(y - b_1) + l(z - c_1)]^2 -(315/16)[(x - a_1)^2 + (y - b_1)^2 + (z - c_1)^2]^{-11/2} (h^2 + k^2 + l^2) [h(x - a_1) + k(y - b_1) + l(z - c_1)]^4 +(231/16)[(x - a_1)^2 + (y - b_1)^2 + (z - c_1)^2]^{-13/2} [h(x - a_1) + k(y - b_1) + l(z - c_1)]^6$$

In the special case which is now being discussed, the ions are distributed about a central atom at (0, 0, 0), hence the substitution $x = y = z = 0$ is appropriate. Also, all of the nearest neighbor ions are at a distance a, the nearest neighbor distance. Thus $a_1^2 + b_1^2 + c_1^2 = a^2$. Defining $\rho^2 = h^2 + k^2 + l^2$ and incorporating the above substitutions:

0th $1/a$

1st $(ha_1 + kb_1 + lc_1)/a^3$

2nd $-(1/2)(\rho^2)/a^3$
$+(3/2)(ha_1 + kb_1 + lc_1)^2/a^5$

3rd $-(3/2)(\rho^2)\ (ha_1 + kb_1 + lc_1)/a^5$
$+(5/2)(ha_1 + kb_1 + lc_1)^3/a^7$

4th $(3/8)\rho^4/a^5$
$-(15/4)\ \rho^2\ (ha_1 + kb_1 + lc_1)^2/a^7$
$+(35/8)(ha_1 + kb_1 + lc_1)^4/a^9$

5th $(15/8)(\rho^4)(ha_1 + kb_1 + lc_1)/a^7$
$-(35/4)(\rho^2)(ha_1 + kb_1 + lc_1)^3/a^9$
$+(63/8)(ha_1 + kb_1 + lc_1)^5/a^{11}$

6th $-(5/16)\ \rho^6/a^7$
$+(105/16)(\rho^4)(ha_1 + kb_1 + lc_1)^2/a^9$
$-(315/16)(\rho^2)(ha_1 + kb_1 + lc_1)^4/a^{11}$
$+(231/16)(ha_1 + kb_1 + lc_1)^6/a^{13}$

In all of the systems of interest, there are pairs of nearest

neighbors at (a_1, b_1, c_1) and $(-a_1, -b_1, -c_1)$. Thus all the odd terms cancel and only the even terms need to be considered.

0th $\quad 1/a$

2nd $\quad -(1/2)\ \rho^2/a^3$

$+(3/2)(ha_1 + kb_1 + lc_1)^2/a^5$

4th $\quad (3/8)\ \rho^4/a^5$

$-(15/4)\ \rho^2\ (ha_1 + kb_1 + lc_1)^2/a^7$

$+(35/8)(ha_1 + kb_1 + lc_1)^4/a^9$

6th $\quad -(5/16)\ \rho^6/a^7$

$+(105/16)\ \rho^4\ (ha_1 + kb_1 + lc_1)^2/a^9$

$-(315/16)\ \rho^2\ (ha_1 + kb_1 + lc_1)^4/a^{11}$

$+(231/16)(ha_1 + kb_1 + lc_1)^6/a^{13}$

Now that a generalized expansion exists for symmetric pairs of ions, it can be applied to the systems of interest. First the planar hexagonal close packed will be done. Only 0th, 2nd and 4th order terms will be considered.

Planar Hexagonal

6 nearest neighbors

(a, o, o) $\qquad$ $(-a, o, o)$

$\left(\frac{1}{2}a, \frac{(3)^{\frac{1}{2}}}{2}a, o\right)$ $\qquad$ $\left(-\frac{1}{2}a, -\frac{(3)^{\frac{1}{2}}}{2}a, o\right)$

$\left(\frac{1}{2}a, \frac{-(3)^{\frac{1}{2}}}{2}a, o\right)$ $\qquad$ $\left(-\frac{1}{2}a, \frac{(3)^{\frac{1}{2}}}{2}a, o\right)$

0th $\quad 6/a$

2nd $\quad -\frac{3}{2}\frac{1}{a^3}(3l^2 - \rho^2)$

4th $\quad \frac{9}{4}\frac{\rho^4}{a^5} - \frac{45}{4}\frac{\rho^2}{a^5}(\rho^2 - l^2) + \frac{315}{64}\frac{1}{a^5}(h^4 + 2h^2k^2 + k^4)$

Next, the simple cubic potential will be calculated.

Simple Cubic

6 nearest neighbors

(a, o, o) $\qquad$ $(-a, o, o)$

(o, a, o) $\qquad$ $(o, -a, o)$

(o, o, a) $\qquad$ $(o, o, -a)$

0th $\quad 6/a$

2nd $\quad 0$ $\qquad$ No spherical term

4th $\quad -\frac{35}{4}\frac{1}{a^5}\left[\frac{3}{5}\rho^4 - (h^4 + k^4 + l^4)\right]$

Finally, face centered cubic will be done.

Face Centered Cubic

12 nearest neighbors

	$(2)^{-1/2}$ (a, a, o)	$(2)^{-1/2}$ (-a, -a, o)
	$(2)^{-1/2}$ (a, -a, o)	$(2)^{-1/2}$ (-a, a, o)
	$(2)^{-1/2}$ (a, 0, a)	$(2)^{-1/2}$ (-a, o, -a)
	$(2)^{-1/2}$ (a, o, -a)	$(2)^{-1/2}$ (-a, o, a)
	$(2)^{-1/2}$ (o, a, a)	$(2)^{-1/2}$ (o, -a, -a)
	$(2)^{-1/2}$ (o, a, -a)	$(2)^{-1/2}$ (o, -a, a)

0th $12/a$

2nd 0 No spherical term

4th $(35/8)(1/a^5)[3/5\ \rho^4 - (h^4 + k^4 + l^4)]$

Note: The fourth order term is -1/2 of the simple cubic 4th order term. This is intuitively appealing since the ions and gaps are interchanged between SC and FCC and there are twice as many ions in FCC as SC, hence 1/2 the deviation from sphericity.

APPENDIX 3

Calculation of the Crystal Field Splitting in Planar Hexagonal and Face Centered Cubic Potentials

The high symmetry potentials were calculated in Appendix 2 for planar hexagonal and face centered cubic nearest neighbor structures. In this appendix, these potentials are used to calculate the relative splitting of the $l = 2$ states in such crystal fields.

From Appendix 2, substituting $h \to x$, $k \to y$, $l \to z$, $\rho \to r$ and inserting the charge e, the first non-zero term above 0th order:

$$V_{HEX} = -(3/2)(e/a^3)(3\,z^2 - r^2)$$

$$V_{FCC} = -(35/8)(e/a^5)[x^4 + y^4 + z^4 - (3/5)\,r^4]$$

Note that the zeroth order term is being omitted. It would serve only to shift the entire manifold. First, the hexagonal case will be considered and then the face centered cubic-octahedral.

Planar Hexagonal

$H = H^0 + H^1$ Hamiltonian

$H^1 = q\,V_{HEX} = -e\,V_{HEX}$ Perturbation Hamiltonian

If the Hamiltonian H^0 were solely of an atomic spherical

symmetry, then all of the $l = 2$ states would be degenerate. Hence, let the $l = 2$ states be treated with degenerate perturbation theory.

The major consideration of first order degenerate perturbation theory is to determine the correct basis set and the cross terms or non-zero off-diagonal matrix elements of the initial basis set. In this case

$$H^1 = -e\, V_{HEX}$$
$$= (3/2)(e^2/a^3)(3\, z^2 - r^2)$$
$$= (6e^2/a^3)(\pi/5)^{1/2}\, r^2\, Y_0^2 = c_1\, r^2\, Y_2^o$$

where Y_2^0 is the spherical harmonic with $l = 2$, $m_l = 0$, and c_1 is a constant. The initial basis set is the group of $l = 2$ spherical harmonics, with spin. Hence, it is easy to calculate the matrix elements using three j (Wigner) integrals.

$$< l = 2,\ m_l = m\ ,\ s = 1/2,\ m_s = \phi_1]\ Y_2^0$$
$$[l = 2,\ m_l = M,\ s = 1/2,\ m_s = \phi_2 > =$$
$$[\int (Y_2^m)^*\ Y_2^o\ Y_2^M\ \sin\theta\ d\theta\ d\phi\ ]\ [\ \delta_{\phi_1,\phi_2}\ ]$$

which will only be non-zero if

1) $\phi_1 = \phi_2$

2) $m = M$

Thus in this basis set, only diagonal matrix elements are non-zero and there are no cross terms.

Under these conditions, the first order perturbation correction is

equal to the expectation value (diagonal matrix element) of the perturbation Hamiltonian.

$$E_n = E_n^{(o)} + H_{nn}^{(1)}$$

$$H_{nn}^{(1)} = \langle n] -e\, V_{HEX}\, [n \rangle$$

$$= \langle 2, m, 1/2, \phi\,]\, c_1\, r^2\, Y_2^0\, [\, 2, m, 1/2, \phi \rangle$$

$$= c_1\, r^2 \int (Y_2^m)^*\, Y_2^0\, Y_2^m \sin\theta\, d\theta\, d\phi$$

To be more exact, $r^2 \rightarrow \langle r^2 \rangle$, with $\langle r^2 \rangle$ being the radial expectation value, which is the same for a given l manifold and principal quantum number. Hence:

$$H_{nn}^{(1)} = c_1 \langle r^2 \rangle \int (Y_2^m)^*\, Y_2^0\, Y_2^m \sin\theta\, d\theta\, d\phi$$

Noting that $(Y_1^m)^* = (-1)^m\, Y_1^{-m}$ and using 3-j (Wigner) symbols to calculate the expectation values:

$$Y_2^0 \qquad H_{nn}^{(1)} = \frac{6}{7} \frac{e^2 \langle r^2 \rangle}{a^3} = \frac{6}{7} E'$$

$$Y_2^{\pm 1} \qquad H_{nn}^{(1)} = \frac{3}{7} \frac{e^2 \langle r^2 \rangle}{a^3} = \frac{3}{7} E'$$

$$Y_2^{\pm 2} \qquad H_{nn}^{(1)} = \frac{-6}{7} \frac{e^2 \langle r^2 \rangle}{a^3} = \frac{-6}{7} E'$$

$$E' = e^2 \langle r^2 \rangle / a^3 \geq 0$$

Planar Hexagonal Splitting

Representation Under C_{6V}	Spherical Harmonic	Shift	Splitting
A_1	Y_2^0	(6/7) E'	
			(3/7) E'
E_1	$Y_2^{\pm 1}$	(3/7) E'	
			(9/7) E'
E_2	$Y_2^{\pm 2}$	(-6/7) E'	

$$E' = \frac{e^2 \langle r^2 \rangle}{a^3} \geq 0$$

Hence $A_1(Y_2^0)$ is the least tightly bound and $E_2(Y_2^{\pm 2})$ is the most tightly bound. To calculate the magnitude of the splitting it is necessary to have a detailed knowledge of the radial wavefunction to calculate $\langle r^2 \rangle$. Unfortunately, that does not exist at this point for c(10 x 2) Ag/Cu(001). Note that the relative splitting is in the ratio of 1/3 = 0.33. The observed ratio is 0.6/1.0 = 0.6. However, this is based upon a linear extrapolation to the center of the surface Brillouin zone for $E_2(Y_2^{\pm 2})$ and is thus only approximate.

Face Centered Cubic - Octahedral

Consider the perturbation Hamiltonian:

$$H^1 = -e\, V_{\substack{FCC \\ OCT}}$$

$$= (35/8)(e/a^5)(x^4 + y^4 + z^4 - (3/5)r^4)$$

$$= c_2\, r^4\, [Y_4^o + (5/14)^{1/2}\, (Y_4^4 + Y_4^{-4})]$$

$$c_2 = (\pi)^{1/2}(7/6)(e/a^5)$$

Check for cross terms with spherical harmonics. First the Y_4^0 term:

$$< 2, m, 1/2, \phi_1]\ Y_4^o\ [\ 2, M, 1/2, \phi_2 >$$

$$= [\ \int (Y_2^m)^*\ Y_4^o\ Y_2^M \sin\theta\, d\theta\, d\phi\ ]\ [\delta\phi 1, \phi 2]$$

This will be non-zero if:

1) $\phi_1 = \phi_2$

2) $m = M$

Hence, there are only diagonal terms here. Next, the $Y_4^{\pm 4}$ terms are considered:

$$< 2, m, 1/2, \phi_1]\ Y_4^{\pm 4}\ [\ 2, M, 1/2, \phi_2 >$$

$$= [\ \int (Y_2^m)^*\ Y_4^{\pm 4}\ Y_4^M \sin\theta\, d\theta\, d\phi\ ]\ [\ \delta_{\phi 1, \phi 2}]$$

which will be non-zero if:

1) $\phi_1 = \phi_2$

2) $-m + (\pm 4) + M = 0$

$$M - m = \pm 4$$

This means that the only cross terms are between $m_l = 2$ and $m_l = -2$, with the same spin. From degenerate perturbation theory for a doubly degenerate level, it is known that

$$E_n = E_n^{(0)} + 1/2\ (H_{nn}^{(1)} + H_{ll}^{(1)}) \pm 1/2\ [(H_{nn}^{(1)} - H_{ll}^{(1)})^2 + 4|H_{nl}^{(1)}|^2]^{1/2}$$

and that

$$[N > = C_{nn}\ [n > + C_{nl}\ [l >$$

$$[L > = C_{ln}\ [n > + C_{ll}\ [l >$$

with $[N >$, $[L >$ the new basis set and $[n >$, $[l >$ the old basis set. It is possible to continue with the present basis set to calculate the energetics or to calculate a new basis set without cross terms. The latter path is more straightforward and informative and thus will be pursued.

$[N >$ and $[L >$ are orthonormal and it is assumed that all the coefficients are real. $[n >$ and $[l >$ are orthonormal. Then

$$<N][N> = 1 = C_{nn}^2 + C_{nl}^2$$

$$<L][L> = 1 = C_{ln}^2 + C_{ll}^2$$

$$<L][N> = <N][L> = 0 = C_{nn}C_{ln} + C_{nl}C_{ll}$$

In the case of interest, the H^1 causing the splitting is $Y_4^{\pm 4}$ and the states are $Y_2^{\pm 2}$. This implies an equivalence of n and l above, with only the relative phase, or sign, being different. This means that

$$|C_{nn}| = |C_{nl}|$$

and

$$|C_{1n}| = |C_{11}|$$

Combining this with the above orthonormality

$$|C_{nn}| = |C_{11}| = |C_{1n}| = |C_{n1}| = (2)^{-1/2}$$

Going back to $Y_2^{\pm 2}$, two states are thus obtained

$$(2)^{-1/2}\ (Y_2^2 + Y_2^{-2}) = C_3\ (x^2 - y^2)$$
$$(2)^{-1/2}\ (Y_2^2 - Y_2^{-2}) = C_4\ (xy)$$

with C_3 and C_4 normalization coefficients.

This is consistent with what is known of the O_h point group: xy and $x^2 - y^2$ are of different representations and thus have no off-diagonal matrix elements for operators of octahedral symmetry.

Now that an orthonormal basis set which is diagonal under the octahedral perturbation has been obtained, the splitting must be calculated using 3-j (Wigner) symbols and remembering that $(Y_1^m)^* = (-1)^m\ Y_1^{-m}$.

$$\int Y_2^0\ Y_4^0\ Y_2^0 \sin\theta\, d\theta\, d\phi = (3/7)(\pi)^{-1/2}$$
$$\int (Y_2^{\pm 1})^*\ Y_4^0\ Y_2^{\pm 1} \sin\theta\, d\theta\, d\phi = -(2/7)(\pi)^{-1/2}$$
$$\int (Y_2^{\pm 2})^*\ Y_4^0\ Y_2^{\pm 2} \sin\theta\, d\theta\, d\phi = (1/14)(\pi)^{-1/2}$$
$$\int (Y_2^2)^*\ Y_4^4\ Y_2^{\pm 2} \sin\theta\, d\theta\, d\phi = [(5/14)(1/\pi)]^{1/2}$$

All other integrals of interest are zero. Summing the contributions, the following results are obtained.

Y_2^0 $\quad (3/7)\ (\pi)^{-1/2}$

$Y_2^{\pm 1}$ $\quad (-2/7)\ (\pi)^{-1/2}$

$$\frac{Y_2^2 + Y_2^{-2}}{(2)^{1/2}} \quad (1/2)(\pi)^{-1/2}\,[(1/14) + (1/14) + (5/14)^{1/2}\,(5/14)^{1/2} + (5/14)^{1/2}\,(5/14)^{1/2}] = (3/7)\,(\pi)^{-1/2}$$

$$\frac{Y_2^2 - Y_2^{-2}}{(2)^{1/2}} \quad (1/2)(\pi)^{-1/2}\,[(1/14) + (1/14) - (5/14)^{1/2}\,(5/14)^{1/2} - (5/14)^{1/2}\,(5/14)^{1/2}] = -(2/7)(\pi)^{-1/2}$$

This is consistent with placing Y_2^0 and $(2)^{-1/2}\,(Y_2^2 + Y_2^{-2})$ in the E_g representation and $Y_2^{\pm 1}$ and $(2)^{-1/2}\,(Y_2^2 - Y_2^{-2})$ in the T_{2g} representation of O_h.

To calculate the splittings:

$$H_{NN}^{(1)} = \langle N] - e\,V_{\substack{FCC \\ OCT}}\,[N\rangle$$

$$= (7/6)(\pi)^{1/2}(e/a^5)\langle r^4\rangle\,\langle N]\,(Y_4^0 + (5/14)^{1/2}\,(Y_4^4 + Y_4^{-4}))\,[N\rangle$$

with $\langle r^4\rangle$ the radial expectation value, which is the same for a given pair of principal and orbital angular momentum quantum numbers.

Representation	Spherical Harmonic	Shift	Splitting
E_g $(3z^2 - r^2)$	Y_2^0	$\frac{e^2\langle r^4\rangle}{a^5}$ $\frac{1}{2} = \frac{1}{2}$ E"	
E_g $(x^2 - y^2)$	$(2)^{-1/2}$ $(Y_2^2 + Y_2^{-2})$		
			5/6 E"
T_{2g} (xy, yz)	$Y_2^{\pm 1}$	$\frac{e^2\langle r^4\rangle}{a^5}$ $(\frac{-1}{3}) = \frac{-1}{3}$ E"	
T_{2g} (xy)	$(2)^{-1/2}$ $(Y_2^2 - Y_2^{-2})$		

$$E'' = \frac{e^2\langle r^4\rangle}{a^5}$$

REFERENCES

1. D. E. Eastman and W. D. Grobman, Phys. Rev. Lett. 30, 177 (1973).
2. I. Abbati, L. Braichovich, C. M. Bertoni, C. Calandra and F. Manghi, Phys. Rev. Lett. 40, 469 (1978); I. Abbati, L. Braichovich, A. Fasana, C.M. Bertoni, F. Manghi, and C. Calandra, Phys. Rev. B23, 6448 (1981).
3. S.-L. Weng and M. El-Batanouny, Phys. Rev. Lett. 44, 612 (1980).
4. L. Gonzalez, R. Miranda, M. Salmeron, J. A. Verges, and F. Yndurain, Phys. Rev. B24, 3245 (1981).
5. C. Binns and C. Norris, Surf. Sci. 115, 395 (1982); 116, 338 (1982).
6. R. Miranda, F. Yndurain, C. Chandesris, J. Lecante, and Y. Petroff, Phys. Rev. B25, 527 (1982); Surf. Sci. 117, 319 (1982).
7. G.C. Smith, C. Norris, C. Binns and H.A. Padmore, J. Phys. C: Solid State Phys. 15, 6481 (1982).
8. M. El-Batanouny, D.R. Hamann, S.R. Chubb and J.W. Davenport, Phys. Rev. B27, 2575 (1983); M. El-Batanouny, M. Strongin and G.P. Williams, Phys. Rev. B27, 4580 (1983).
9. J. G. Tobin, S. W. Robey, L. E. Klebanoff and D. A. Shirley, LBL-14187, submitted to Phys. Rev. Lett.; LBL-15134.
10. J. Tersoff and L. M. Falicov, Phys. Rev. B25, 2959 (1982).
11. D.-S. Wang, A. J. Freeman, H. Krakauer, Phys. Rev. B26, 1340 (1982); C. S. Wang and A. J. Freeman, Phys. Rev. B18, 1714 (1978); Phys. Rev. B19, 793 (1979); Phys. Rev. B21, 4585 (1980); Phys. Rev. B24, 4364 (1981).

12. B. R. Cooper, Phys. Rev. Lett. 26, 1316 (1973).

13. J. G. Gay, J. R. Smith, and F. J. Arlinghaus, Phys. Rev. Lett. 38, 561 (1977); Phys. Rev. B20, 1332 (1979); Phys. Rev. B21, 2055 (1980); Phys. Rev. B21, 2201 (1980); Phys. Rev. B22, 4757 (1980); Phys. Rev. B25, 643 (1982).

14. G. S. Painter, Phys. Rev. B17, 3848 (1978).

16. O. Jepsen, J. Madsen and O. K. Andersen, Phys. Rev. B26, 2790 (1982).

17. P. D. Loly and J. B. Pendry, J. Phys. C. 16, 423 (1983).

18. P. W. Palmberg and T. N. Rhodin, J. Appl. Phys. 39, 2425 (1968); J. Chem. Phys. 49, 134 (1968); 49, 147 (1968).

19. J. A. Knapp, F. J. Himpsel and D. E. Eastman, Phys. Rev. B19, 4952 (1979).

20. N. E. Christensen, Phys. Stat. Sol. (B) 54, 551 (1972).

21. H. F. Roloff and H. Neddermeyer, Solid State Comm. 21, 561 (1977).

22. G. V. Hansson and S. A. Flodstrom, Phys. Rev. B17, 473 (1978).

23. D. Liebowitz and N. J. Shevchik, Phys. Rev. B17, 3825 (1978).

24. P. S. Wehner, R. S. Williams, S. D. Kevan, D. Denley and D. A. Shirley, Phys. Rev. B19, 6164 (1979).

25. D. P. Spears, R. Melander, L. G. Petersson and S.B.M. Hagstrom, Phys. Rev. B21, 1462 (1980).

26. P. Heimann, J. Hermanson, H. Miosga, and H. Neddermeyer, Phys. Rev. Lett. 42, 1782 (1979); Phys. Rev. B20, 3059 (1979).

27. S. D. Kevan and D. A. Shirley, Phys. Rev. B22, 542 (1980).

28. G. Petzow, "Metallographic Etching", Amer. Soc. for Metals,1978;

page 59, chemical polish Number 1.

29. W.J.M. Tegart, "The Electrolytic and Chemical Polishing of Metals", Pergamon, 1959; page 100, modified solution.
30. D. C. Jackson, T. E. Gallon and A. Chambers, Surf. Sci. 36, 381 (1973).
31. E. Bauer, Surf. Sci. 7, 351 (1967).
32. J. Holzl, F. K. Schulte and H. Wagner, "Solid Surface Physics", Springer-Verlag, 1979.
33. Z. Hussain, S. Kono, L.-G. Petersson, C.S. Fadley and L.F. Wagner, Phys. Rev. B23, 724 (1981).
34. J.G. Tobin, S.W. Robey, D.A. Shirley, W.J. Gignac, J.G. Nelson, R.S. Williams, LBL-15135.
35. P.Heimann, J.Hermanson, H.Miosga and H. Neddermeyer, Sol. State Comm. 37, 519 (1981).
36. P.S. Wehner, Ph. D. thesis, Univ. of Cal.-Berk., 1978, unpublished.
37. Z. Hussain, E. Umbach, J.J. Barton, J.G. Tobin and D.A. Shirley, Phys. Rev. B25, 672 (1982).
38. G.D. Mahan, Phys. Rev. B2, 4334 (1970).
39. L. Ley, S. P. Kowalzyk, F. R. McFeeley, and D. A. Shirley, Phys. Rev. B10, 4881 (1974).
40. J. Hermanson, Sol. St. Comm. 22, 9 (1977).
41. M. Scheffler, K. Kambe and F. Forstmann, Sol. St. Comm. 25, 93 (1978).
42. C. J. Ballhausen, "Introduction to Ligand Field Theory," McGraw-Hill, 1962.

43. T. A. Carlson, C. C. Lu, T. C. Tucker, C. W. Nestor, F. B. Malik, "Eigenvalues, Radial Expectation Values and Potentials for Free Atoms from Z= 2 to 126 as Calculated from Relativistic Hartree-Fock-Slater Atomic Wavefunctions," Oak Ridge National Laboratory, 4614.

44. E.E. Koch, J. Barth, J.-H. Fock, A. Goldmann and A. Otto, Solid State Comm. 42, 897 (1982).

45. R.F. Davis, S.D. Kevan, B.-C. Lu, J.G. Tobin and D.A. Shirley, Chem. Phys. Lett. 71, 448 (1980).

TABLE CAPTIONS

Table I Experimentally determined values of B^F for Band iv, which is identified with Y_2^o $(3z^2-r^2)$.

Table II Experimentally determined values of B^F for Band iii, which is identified with $Y_2^{\pm 1}$ (xz, yz). Only the s-polarization data is shown here. At normal emission, the feature is visible with s- and p-polarized light (Table V).

Table III Experimentally determined values of B^F for Band ii, which is identified with $Y_2^{\pm 2}$ (xy, x^2-y^2).

Table IV Experimentally determined values of B^F for Band i, which is identified with Y_o^o (r^2).

Table V Normal emission data for Band ii, including both s- and p-polarization features. The values of B^F, like the others in Tables I-IV, were determined by visual inspection. From these, a spin-orbit splitting was determined, ΔB_1^F. ΔB_2^F was determined from fitting the feature with two lorentzians and a linear background. The average spin-orbit-splitting is also shown.

Table I
Band iv

	HeI P-POL (100)	HeI P-POL (110)
$k_{(x,y)}$ ($Å^{-1}$)	B^F(eV)	B^F(eV)
0.00	4.21	4.23
0.31	4.19	4.17

Table II.
Band iii

	HeI S-POL (100)	NeI S-POL (100)	HeI S-POL (110)
$k_{(x,y)}(\text{Å}^{-1})$		B^F(eV)	
0.00	4.66	4.64	4.71
	4.91	4.79	4.87
0.31	4.83	4.78	4.71
0.60	4.87	4.95	4.83
0.86	5.09	5.26	4.97
1.01		5.44	
1.11	5.19		
1.30	5.46		
1.46	5.60		

Table III.
Band ii

	HeI P-POL (100)	NeI P-POL (100)	HeI P-POL (110)
$k_{(x,y)}(\text{Å}^{-1})$		$B^F(eV)$	
0.00			
0.30			
0.57		5.54	5.60
0.85	5.44	5.53	5.52
1.01		5.46	
1.10	5.41		
1.31	5.31		
1.48	5.29		

Table IV
Band i

	HeI P-POL (100)	NeI P-POL (100)	HeI S-POL (100)	NeI S-POL (100)	HeI P-POL (110)
$k_{(x,y)}(\text{Å}^{-1})$			$B^F(eV)$		
0.00	6.65				6.42
0.28	6.46				6.25
0.55	6.16	6.12	6.26	6.21	6.10
0.81	6.25	6.27	6.07	6.23	6.46
0.94		6.17		6.30	
1.05	6.40		6.26		
1.26	6.15		6.22		
1.43	6.14		6.20		

Table V
Spin Orbit Splitting at the 2D SBZ Center
($k_{(x,y)}$ = 0.00 $Å^{-1}$)

	POL	AZIMUTH	B^F(eV)		ΔB^F_1(eV)	ΔB^F_2(eV)
HeI	S	(100)	4.66	4.91	0.25	0.30
NeI	S	(100)	4.64	4.79	0.15	0.28
HeI	S	(110)	4.71	4.87	0.16	0.23
HeI	P	(100)	4.71	4.91	0.20	0.29
NeI	P	(100)	4.73		———	0.33
HeI	P	(110)	4.73	4.97	0.24	0.17
AVERAGE			4.69	4.89	0.20	0.27
STANDARD DEVIATION			0.04	0.07	0.05	0.06

SPIN ORBIT SPLITTING = 0.24(6) eV

FIGURE CAPTIONS

Figure 1. Schematic of the vectoral geometry of the ARPES experiments. The Cu(001) normal, the Poynting vector of the light and the center line of the analyzer acceptance cone are all in the horizontal plane. For p-polarization, the polarization is also in the horizontal plane. In the case of s-polarization, it is perpendicular to the horizontal plane.

Figure 2. Plot of the derivative intensity ratio of the Ag MNN Auger line at 350 eV to the Cu MVV Auger line at 60 eV versus readings from the quartz microbalance thickness monitor.

Figure 3. A depiction of one of the two orthogonal domains of c(10x2) Ag/Cu(001) in real space. Note that the c(10x2) is a slightly strained (±2 percent) hexagonal structure. The actual registry with the substrate is unknown. The Surface Brillouin Zones of Cu(001) and both undistorted hexagonal c(10x2)Ag domains as well as the paths taken across each zone when rotating off-normal in the Cu(001) planes (110) and (100) are shown. Only the domain associated with (c) was observed with LEED. Rotating off normal in the (100) plane, the same direction is taken in both Ag domains.

Figure 4. Spectra taken of clean Cu(001) (lower member of each pair) and 1 1/4 monolayers of c(10x2)Ag/Cu(001) (upper member of each pair), with s-polarized HeI radiation. Analyzer and total resolution is 120 meV. The HeI satellite at 23.1 eV

causes the small structure near the Fermi edge. These spectra were taken rotating away from normal in the (100) plane, with the polarization in the (001) plane. The light polarization and electron emission direction are separated by 90°. The angle listed is the polar emission angle (θ_e).

Figure 5. Same as Figure 4 except that the polarization vector of the light is in the same plane as surface normal and the emitted electrons. The relative angles of the polarization and photoemission vectors are $\langle \underline{A}, \underline{q} = 30^\circ - \theta_e$ for $\theta_e \leq 30^\circ$ and $\langle \underline{A}, \underline{q} = 0^\circ$ for $\theta_e \geq 30^\circ$.

Figure 6. Spectra taken of clean Cu(001) (lower), and 1 3/8 monolayers of c(10x2)Ag/Cu(001) (upper), with NeI radiation. The doublet is at 16.67 and 16.85 eV, so that $h\nu = 16.76 \pm .13$ eV. The analyzer resolution was 240 meV (40eV pass energy) for the clean Cu(001) and 120 meV (20 eV pass energy) for the adsorbate spectra. Adding in quadrature, the total resolution was 270 meV for the clean Cu(001) and 150 meV for the Ag/Cu(001). The spectra were taken rotating off-normal in the (100) plane of Cu(001) with the polarization vector in the (001) plane of Cu(001). $\langle \underline{A}, \underline{q} = 90^\circ$. The angle listed on the side is the polar emission angle, θ_e.

Figure 7. Same as Figure 6 but with the polarization vector in the plane containing the surface normal and the electron emission direction, i.e., (100) of Cu(001). The angles were $\langle \underline{A}, \underline{q} = 30^\circ - \theta_e$ for $\theta_e \leq 30^\circ$; $\langle \underline{A}, \underline{q} = 0^\circ$ for $\theta_e \geq 30^\circ$.

Figure 8. Spectra taken of clean Cu(001) (lower) and 1 3/8 monolayers of c(10x2)Ag/Cu(001) (upper), with HeI and at 120 meV analyzer and total resolution. Same as Figure 4 but with off-normal rotation in the (110) plane of Cu(001). In this case, $<\underline{A}, \underline{q} = 90^\circ$.

Figure 9. Same as Figure 8 but with the polarization vector in the same plane as the surface normal and the electron emission direction, i.e., the (110) plane of Cu(001). $<\underline{A}, \underline{q} = 30^\circ - \theta_e$. The angle listed on the side is the polar emission angle, θ_e.

Figure 10. Spectra taken of 2.5 monolayers of c(10x2)Ag/Cu(001) with HeI radiation and 120 meV resolution. The angle listed along the side as the polar emisson angle, θ_e, in the (100) plane of Cu(001). The s-polarization and the p-polarization spectra are in the upper and lower halves, respectively. For the s polarized, $<\underline{A}, \underline{q} = 90^\circ$. For the p-polarized, $<\underline{A}, \underline{q} = 30^\circ - \theta_e$ for $\theta_e \leq 30^\circ$ and $<\underline{A}, \underline{q} = 0^\circ$ for $\theta_e \geq 30^\circ$.

Figure 11. Plot of binding energy versus $k_{(x,y)}$ in two directions across the Surface Brillouin Zone of c(10x2)Ag. See Figure 3. Table V contains the binding energies of the closely spaced, normal emission data points that would be inside the cross-hatched box.

Figure 12. Crystal field splitting predicted by a FCC octahedral field caused by 12 nearest neighbors and by a hexagonal C_{6v} field caused by 6 in-plane nearest neighbors.

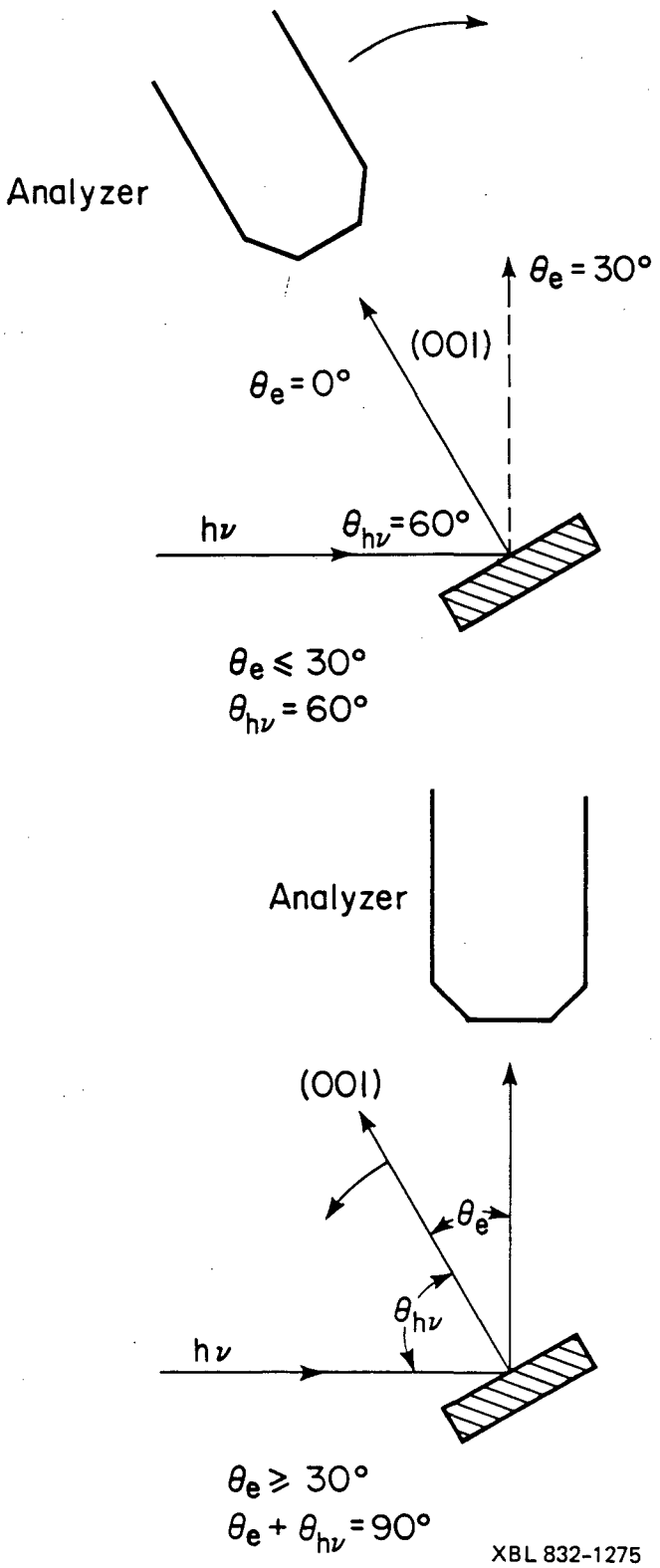
Analyzer
$\theta_e = 30°$
(001)
$\theta_e = 0°$
$h\nu$
$\theta_{h\nu} = 60°$
$\theta_e \leq 30°$
$\theta_{h\nu} = 60°$
Analyzer
(001)
θ_e
$\theta_{h\nu}$
$h\nu$
$\theta_e \geq 30°$
$\theta_e + \theta_{h\nu} = 90°$
XBL 832-1275

Fig. 1

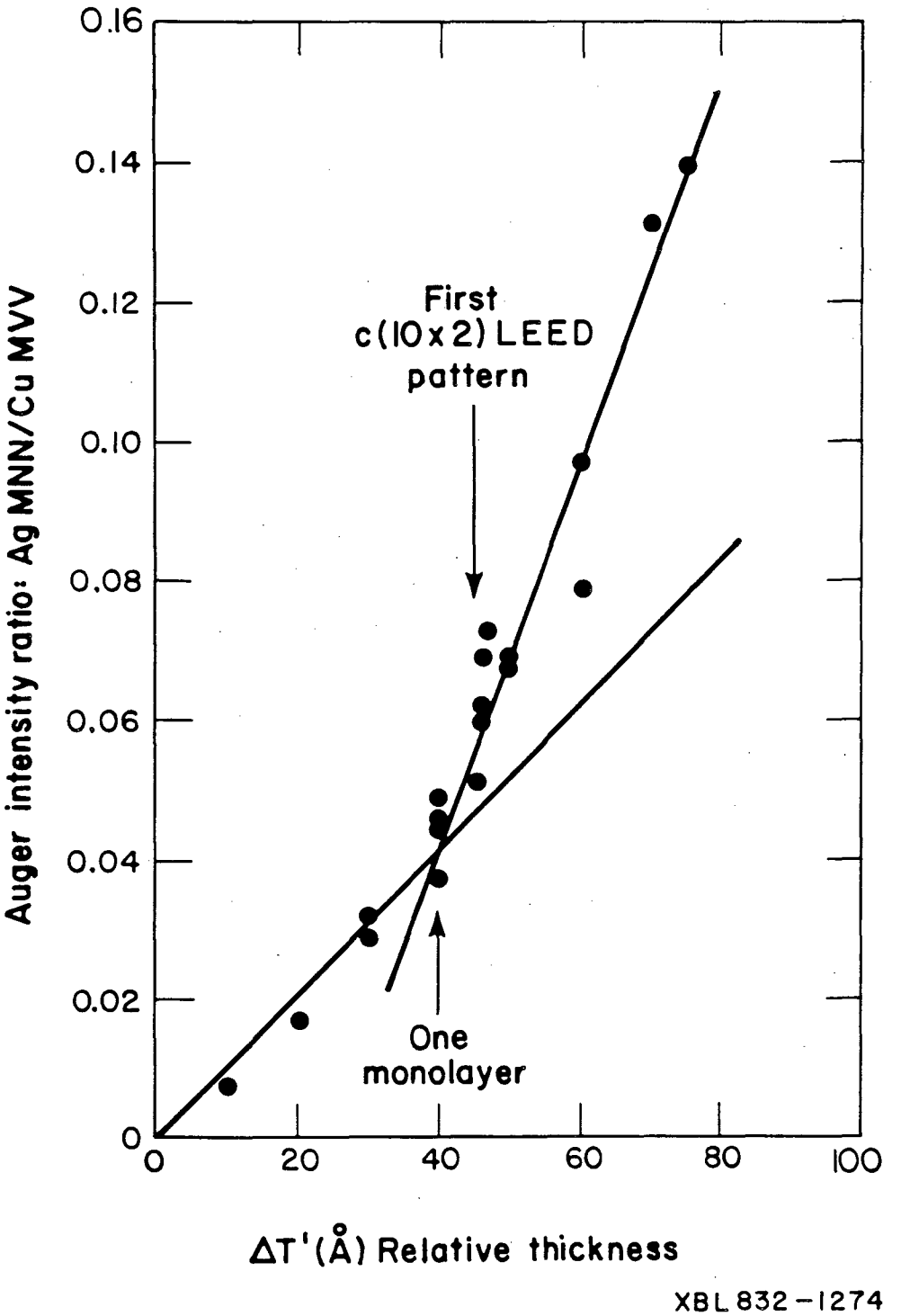
0.16
0.14
0.12
0.10
0.08
0.06
0.04
0.02
0
Auger intensity ratio: Ag MNN/Cu MVV
First
c(10x2) LEED
pattern
One
monolayer
0
20
40
60
80
100
ΔT'(Å) Relative thickness
XBL 832-1274

Fig. 2

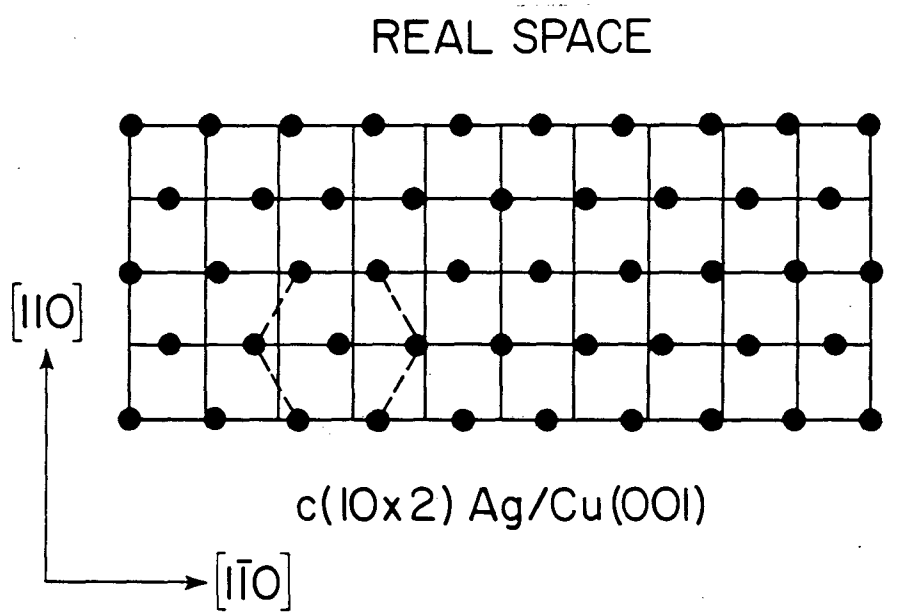
REAL SPACE
[110]
[1$\bar{1}$0]
c(10x2) Ag/Cu(001)
RECIPROCAL SPACE
(110) Plane
(100) Plane
a
$\bar{\Gamma}$ $\bar{\Delta}$
$\bar{X}$
$\bar{X}$=1.23 Å^{-1}
$\bar{\Gamma}$ $\bar{\Sigma}$
$\bar{M}$
$\bar{M}$=1.74 Å^{-1}
b
$\bar{\Gamma}$ $\bar{\Gamma}$
$\bar{K}$
$\bar{K}$=1.45 Å^{-1}
$\bar{\Gamma}$
$\bar{Z}$
$\bar{Z}$=1.29 Å^{-1}
c
$\bar{\Gamma}$ $\bar{\Sigma}$
$\bar{M}$
$\bar{M}$=1.25 Å^{-1}
$\bar{\Gamma}$
$\bar{Z}$
XBL 832-1276

Fig. 3

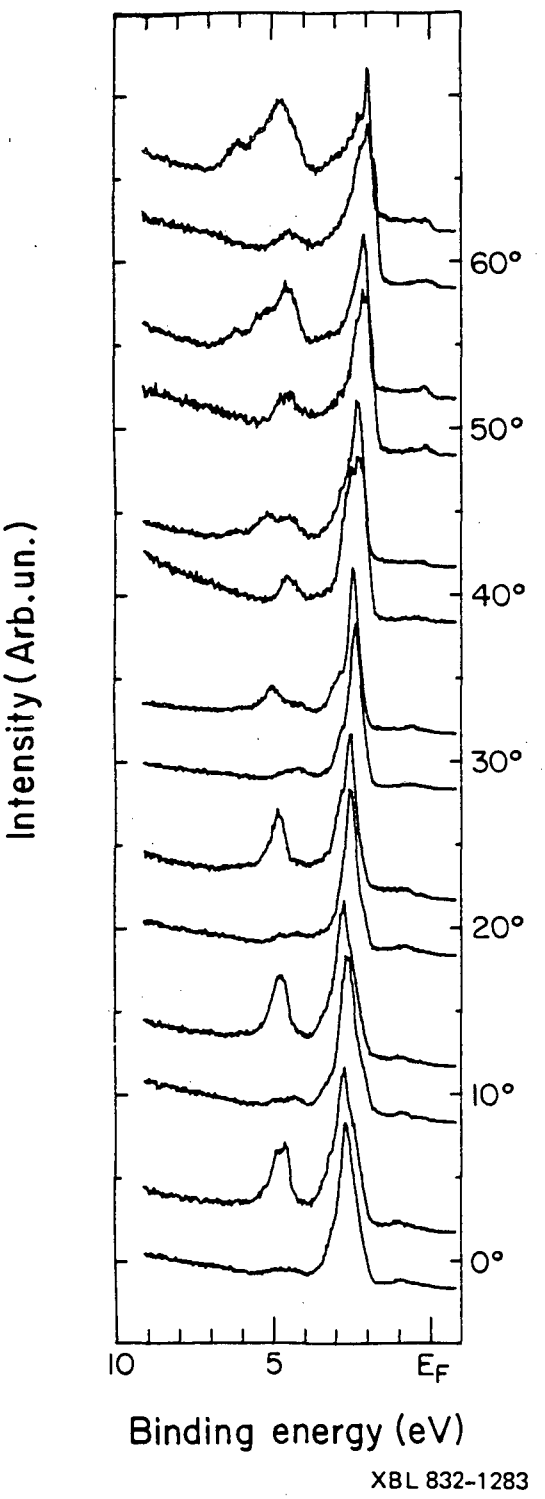
HeI S-Pol <100>
Intensity (Arb.un.)
60°
50°
40°
30°
20°
10°
0°
10
5
E_F
Binding energy (eV)
XBL 832-1283

Fig. 4

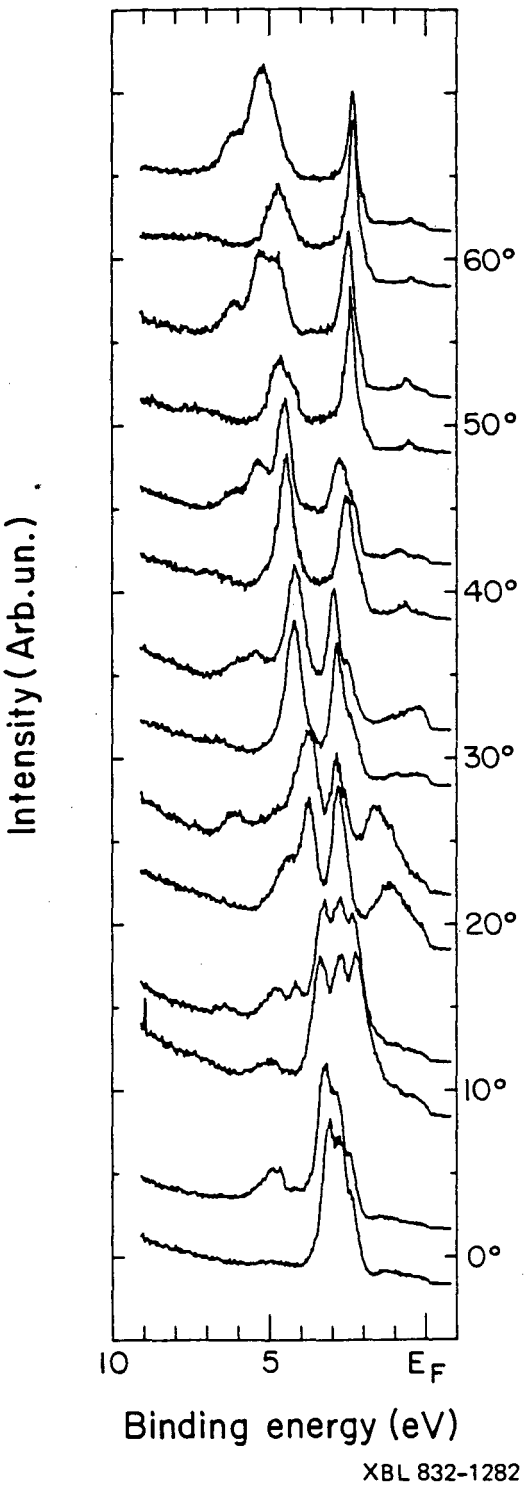
HeI P-Pol <100>
Intensity (Arb.un.)
60°
50°
40°
30°
20°
10°
0°
10
5
E_F
Binding energy (eV)
XBL 832-1282

Fig. 5

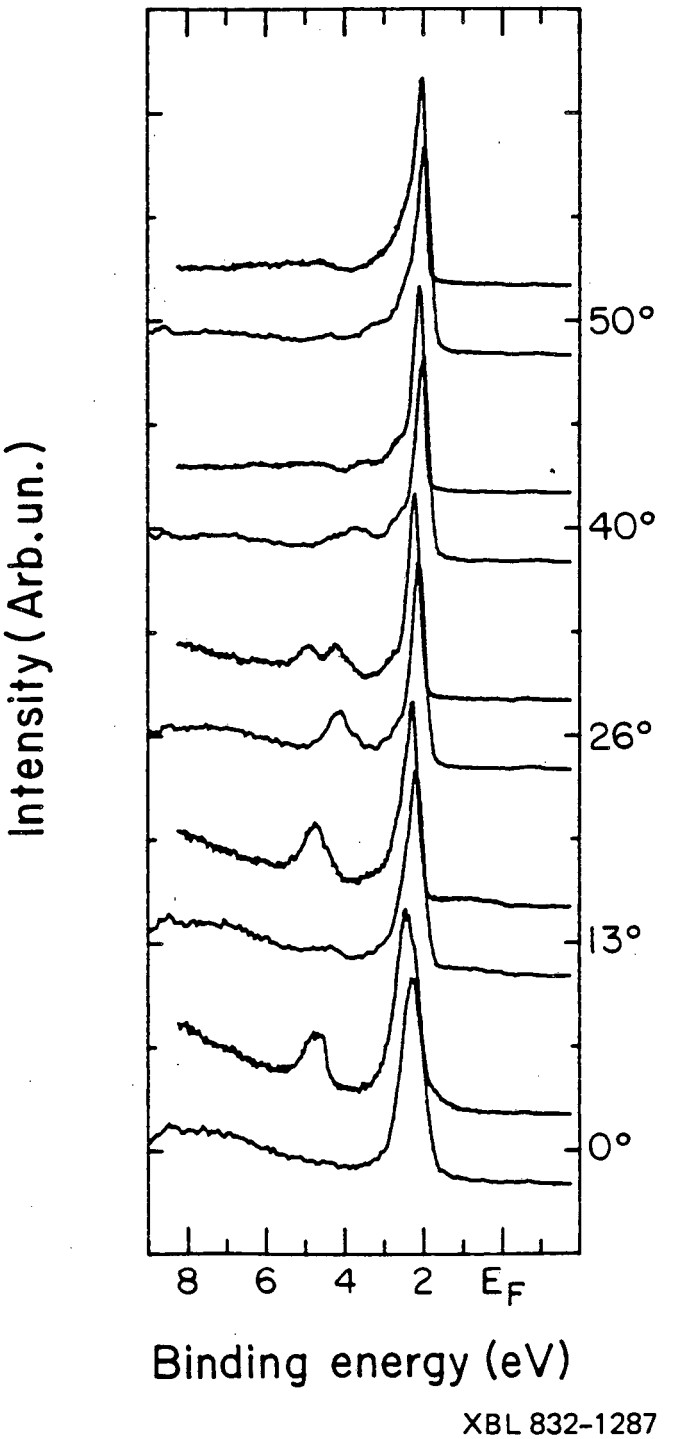
NeI S-POL <100>
Intensity (Arb.un.)
50°
40°
26°
13°
0°
8
6
4
2
E_F
Binding energy (eV)
XBL 832-1287

Fig. 6

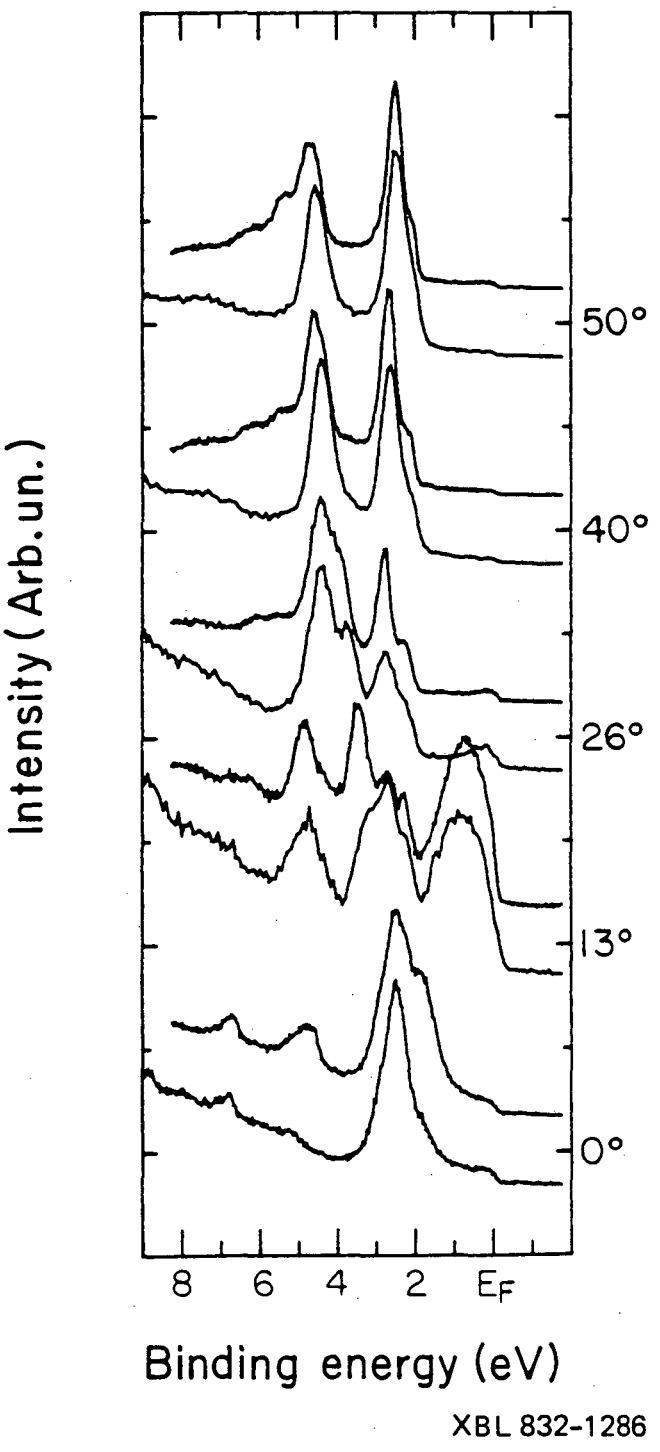
NeI P-POL <100>
Intensity (Arb.un.)
50°
40°
26°
13°
0°
8
6
4
2
EF
Binding energy (eV)
XBL 832-1286

Fig. 7

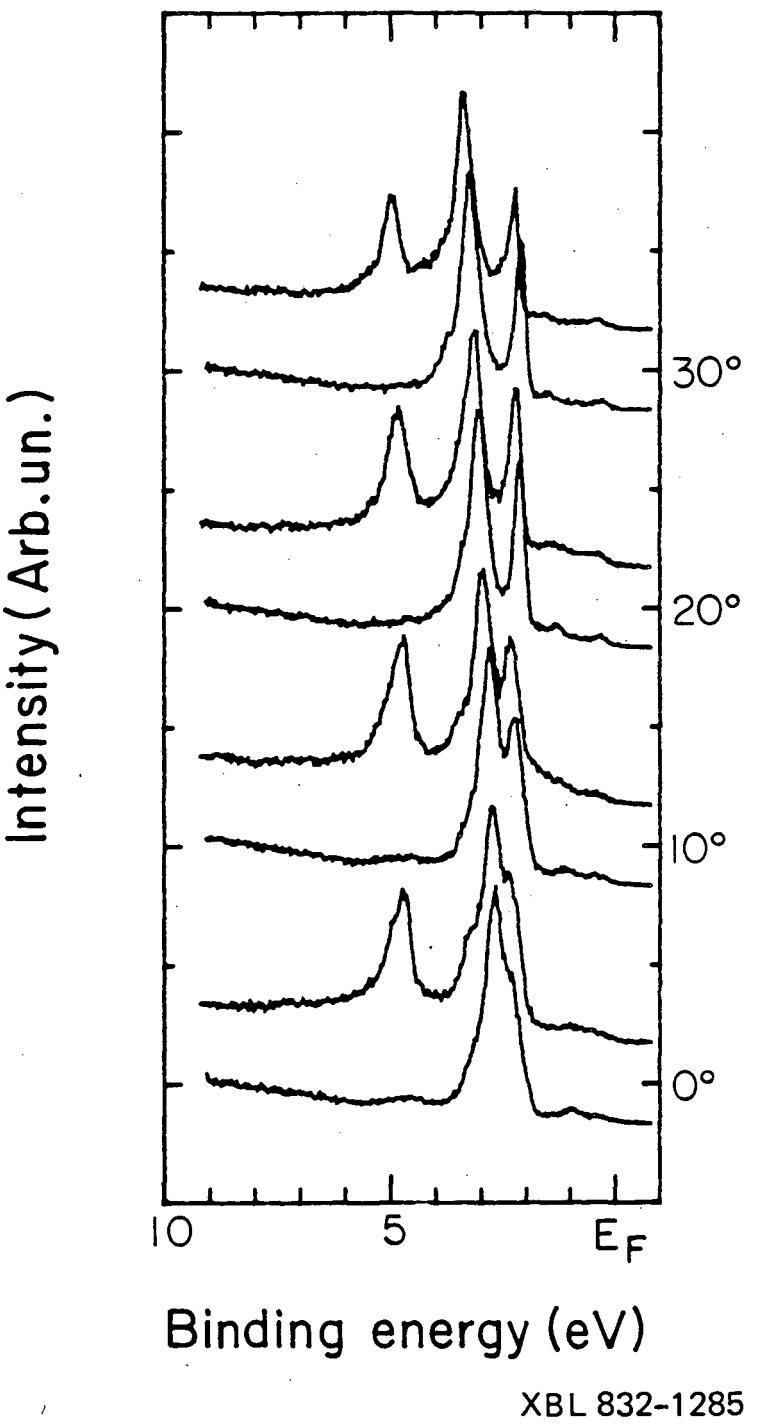
HeI S-POL <110>
Intensity (Arb.un.)
30°
20°
10°
0°
10
5
E_F
Binding energy (eV)
XBL 832-1285

Fig. 8

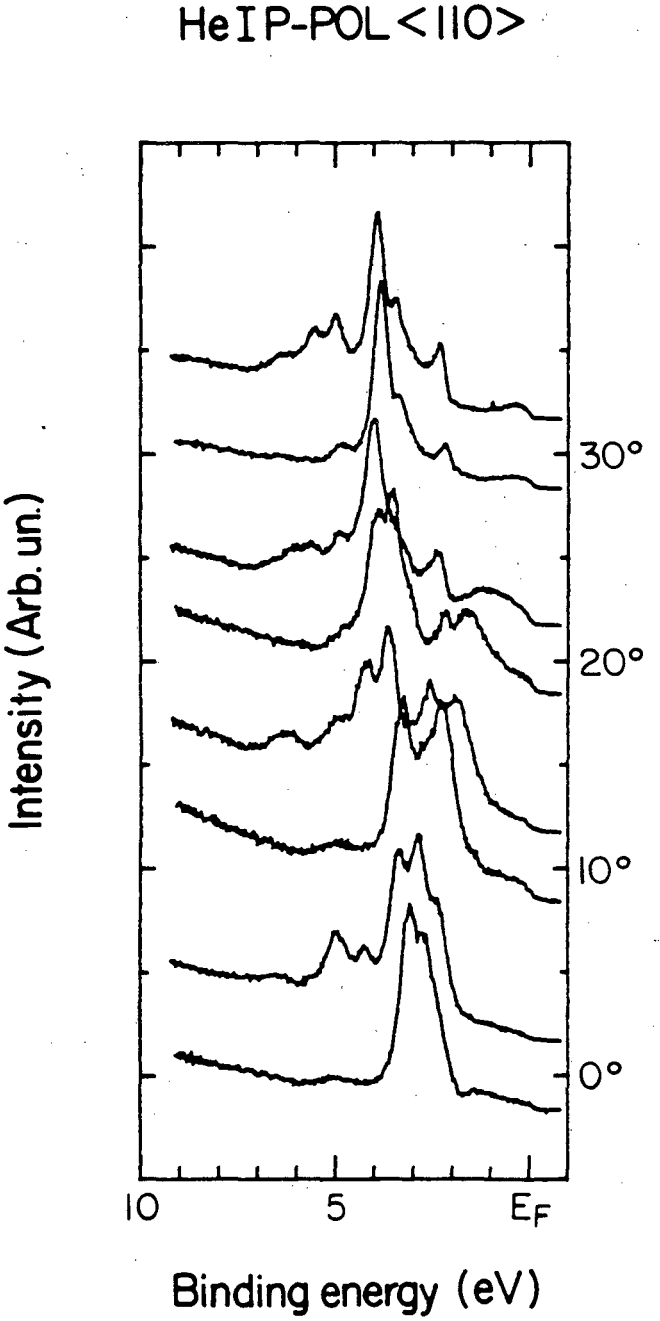
HeI P-POL <110>
Intensity (Arb. un.)
30°
20°
10°
0°
10
5
E_F
Binding energy (eV)
XBL 832-1288

Fig. 9

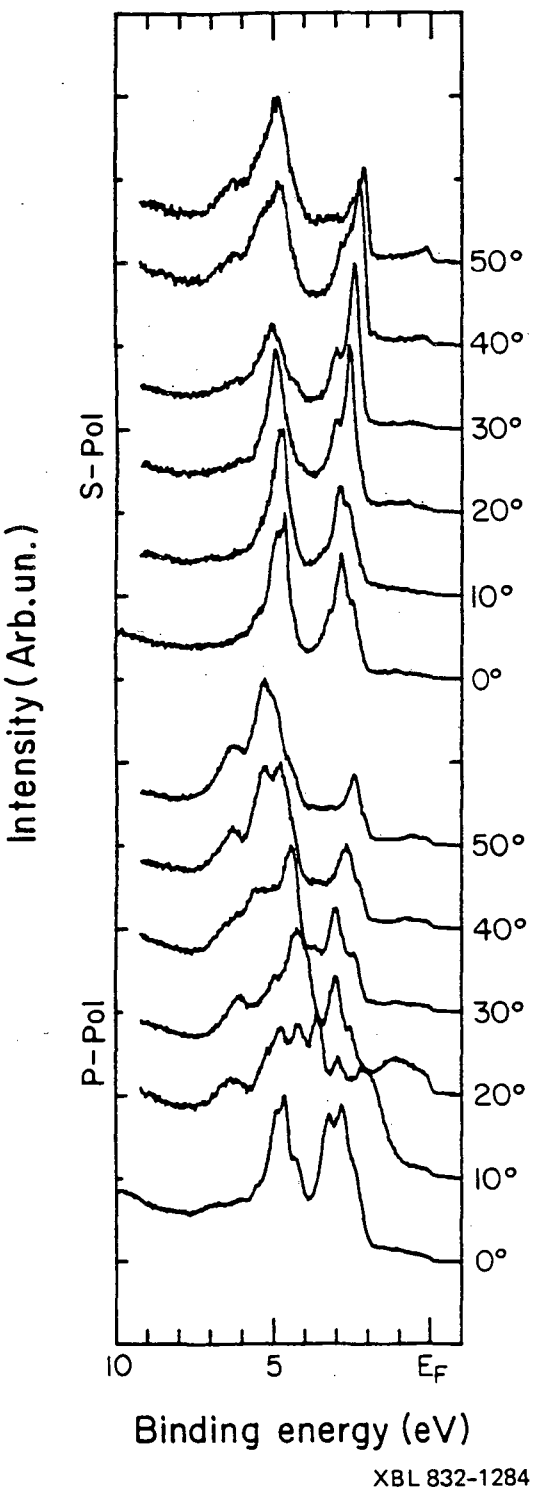
2.5 ML HeI <100>
Intensity (Arb.un.)
S-Pol
P-Pol
50°
40°
30°
20°
10°
0°
50°
40°
30°
20°
10°
0°
10
5
E_F
Binding energy (eV)
XBL 832-1284

Fig. 10

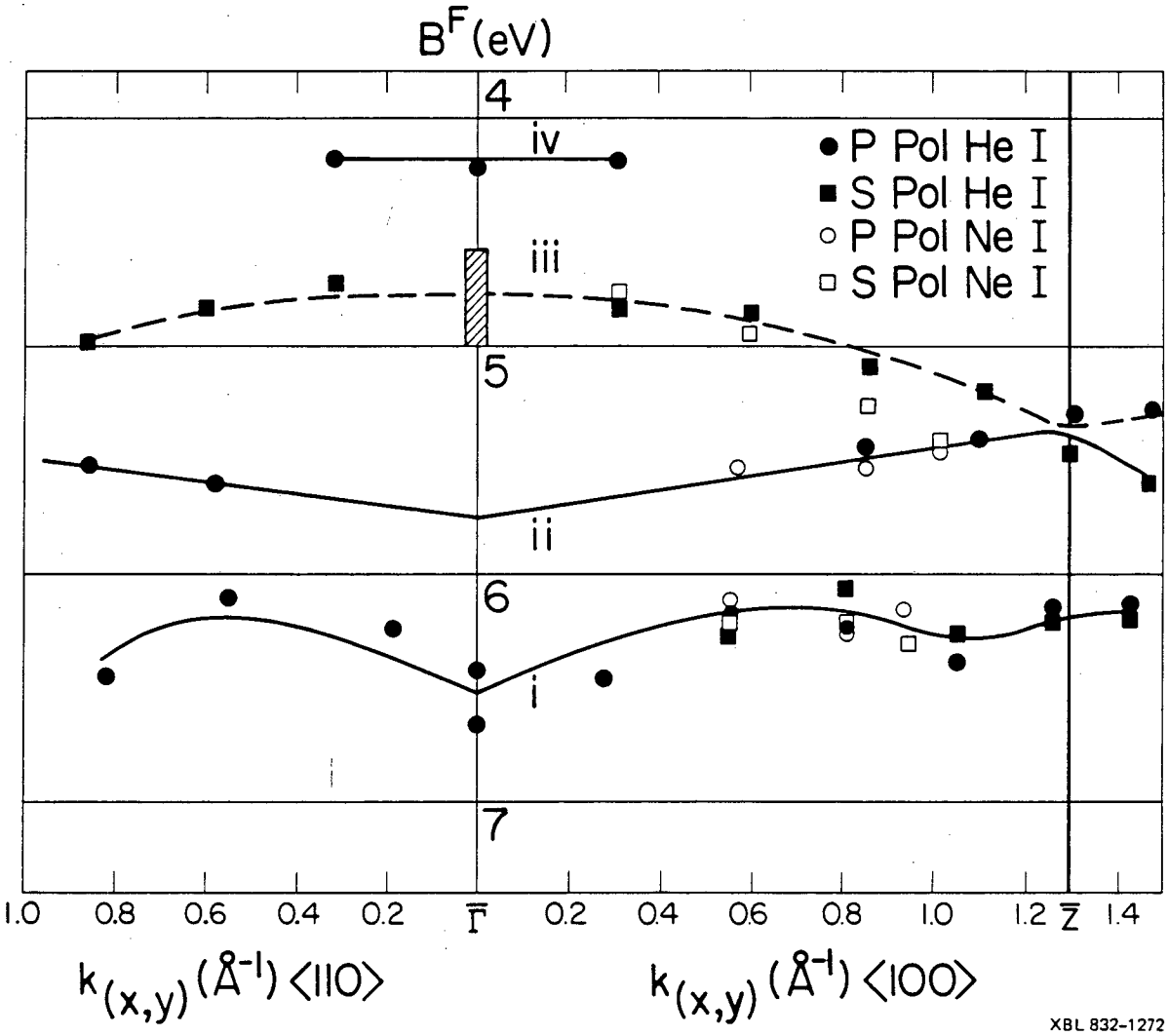
B^F(eV)
4
iv
iii
5
ii
6
i
7
P Pol He I
S Pol He I
P Pol Ne I
S Pol Ne I
1.0 0.8 0.6 0.4 0.2 Γ 0.2 0.4 0.6 0.8 1.0 1.2 Z 1.4
$k_{(x,y)}$ (Å^{-1}) <110>
$k_{(x,y)}$ (Å^{-1}) <100>
XBL 832-1272

Fig. 11

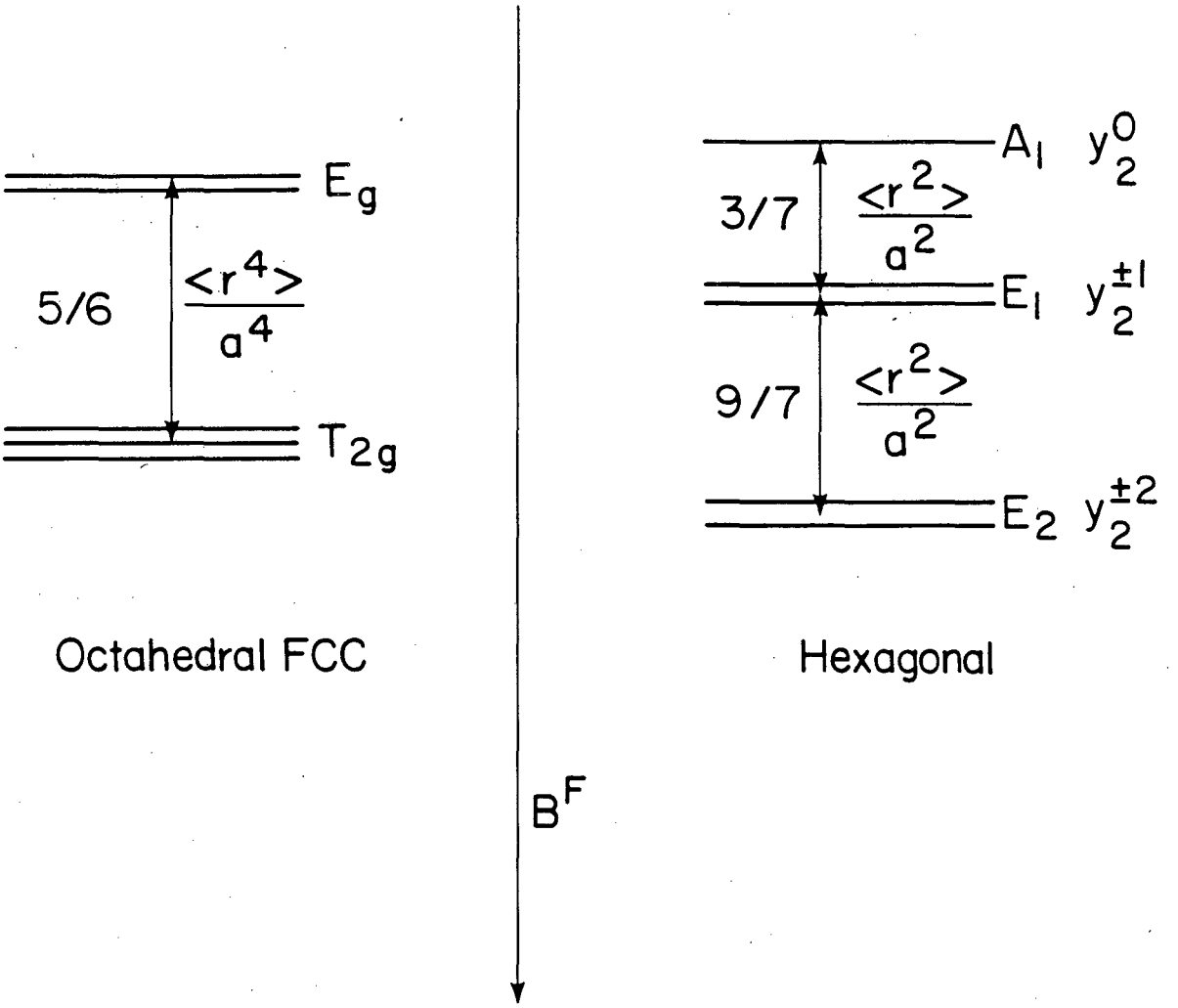

XBL 832-1277

Fig. 12

III. THE DEVELOPMENT OF 3-DIMENSIONAL VALENCE BAND STRUCTURE IN Ag OVERLAYERS ON Cu(001)

A. INTRODUCTION

Over the last several years, a number of photoemission experiments[1-7] and calculations[8,9] have investigated the properties of metal overlayer-metal substrate systems. Also, theoretical efforts[10-15] have been made to elucidate the effect of thickness upon the electronic structure of thin metal slabs, and photoemission has been used to monitor the layer-by-layer bandstructure of physisorbed Xe on Al(111).[16] In an earlier letter,[17] the observation of the development from 2-dimensional to 3-dimensional behavior in the metal overlayer system c(10x2)Ag/Cu(001) was reported. The details of the 2-dimensional system at monolayer coverages were presented in Chapter II.[18] In this chapter, a complete angle-resolved photoemission experiment at higher exposures is presented. This synchrotron radiation study documents the development of the electronic structure in the overlayer from 2-dimensional to 3-dimensional bulk behavior.

The system c(10x2) Ag/Cu(001) was chosen for several reasons, including its layer-by-layer growth pattern at low coverages and the expectation that this would continue at higher exposures, the ease of preparation, the stability of its constituents in vacuo, the limited overlap of the valence bands of adsorbate and substrate, and the fact that Ag(111) has been studied in detail.[19-24] This system also has

the distinct advantage of non-epitaxial growth: Low Energy Electron Diffraction (LEED) as well as Auger Electron Spectroscopy (AES) can therefore be used to follow the growth pattern. The system c(10x2)Ag/Cu(001) is a slightly strained hexagonal structure. It is reasonable to expect higher coverages to approach the geometrical and electronic structure of the (111) face of crystalline silver.

The remainder of this chapter is organized as follows: Section B is a description the experimental details, Section C contains photoemission results and Section D is a discussion of those results. Section E contains a summary of conclusions.

B. EXPERIMENTAL

The first part of this Section is devoted to the details of the photoemission experiment. The second deals with the LEED/AES calibration performed to allow accurate and reproducible preparation of evaporated samples.

1. GENERAL

The measurements were made at the Stanford Synchrotron Radiation Laboratory (SSRL) on Beam Line I-2, over the energy range of $h\nu$= 6-32eV, with an angle resolved photoelectron spectrometer described previously.[25] The base pressure during the experiment was $1x10^{-9}$ Torr and operation of the Ag evaporator had essentially no effect upon the chamber pressure.

The Cu(001) crystal was cut and polished to within $\pm 1^{\circ}$ of the (001) face and chemically polished before introduction into the vacuum system. The crystal was aligned in-situ using LEED and laser

autocollimation to a precision of better than ±1°. The crystal had a specular finish and sharp LEED 1x1 spots, indicative of surface ordering.

Evaporations were performed using a thermal source of Ag atoms which was monitored with a quartz crystal microbalance. The source and microbalance were contained inside a shielded assembly with a shutter to allow time-controlled evaporations.

Room temperature Ar ion etching at pressures of 10^{-5} Torr was used to remove evaporated Ag, as shown by Auger spectroscopy, but cycles of heating to between 500°C and 600°C and cooling with continuous sputtering were used to remove residual contaminants. A final annealing to above 500°C was used to order the clean Cu(001) crystal, at which point contaminant levels were such that neither oxygen nor sulfur was detectable and the C/Cu Auger ratio was 0.004.

Possible sulfur impurities were detected at lower exposures but after extended photoemission measurements and all evaporations, the sulfur and oxygen impurities were barely detectable. Any possible carbon Auger line was obscured by an Auger line of Ag at 260eV.

The analyzer resolution was kept at 60meV (10eV pass energy) throughout the experiment, but the monochromator contribution varied with photon energy and slit width. The uncertainties add in quadrature: $\Delta E^2_{Total} = \Delta E^2_{AN} + \Delta E^2_{MONO}$. The total resolution (FWHM) and the monochromator and analyzer contributions are shown in Table I. The half-angular acceptance was always ±3° or less.

All the photoemission spectra were taken with p-polarized radiation, mainly at normal emission. The polarization was in the same plane as the Poynting vector of the light, the surface normal and the (110) plane of Cu(001). The angle of incidence of the light was 60° with respect to the normal. The single domain of the c(10x2)Ag was oriented such that the polarization and the $\bar{\Gamma} - \bar{\Sigma} - \bar{M}$ direction of the hexagonal Surface Brillouin Zone were in the same plane, as shown in Figure 1.

The binding energies (B^F) were measured with respect to the Fermi energy (E_F), which was determined separately in each individual spectrum as the point of maximum slope in the rise from background to the initial s-p plateau or band feature. The spectrometer work function was determined as a function of exposure. The values found, including the RMS scatter as the error, are shown in Table II. The actual value of the spectrometer work function is, of course, relatively unimportant. The figures of merit are the small RMS scatter at each coverage and the relatively small variation as the coverage was increased. The Ag(111) measurements were made on a later separate experimental run. They are included in Table II for comparison. The Ag(111) experiment is described in Chapter IV and Ref. 24.

2. LEED/Auger Calibration

AES and LEED were used to calibrate the quartz microbalance thickness monitor, as previously discussed in Chapter II. In a layer-by-layer growth pattern, a discontinuity in the slope of the

ratio of adsorbate to substrate intensities is to be expected at one monolayer coverage. Ratios were used because of inaccuracies introduced into absolute measurements by movement of the crystal during the experiment. At a slightly higher coverage than that corresponding to the discontinuity in the slope of the Ag(350eV)/Cu(60eV) ratio, the first c(10x2) LEED spots were observed. The quartz microbalance was thus calibrated for sub- and multi-atomic layer coverages of Ag on the Cu(001) crystal.

As a check on the accuracy of the quartz microbalance, derivative intensity measurements were made of each sample for the Auger lines of Cu(60eV), Ag(350eV) and Cu(920eV) and constantly compared to the original measurements, Ag(350)/Cu(60) and Ag(350)/Cu(920), taken during calibration. The Cu(920eV) measurements were necessary because at higher exposures the Cu(60eV) is drastically attenuated due to its much shorter mean free path. The results proved to be generally internally consistent. A conservative estimate of the accuracy is ±20 percent of the exposure.

LEED observations made at higher exposures (2-5 ML) showed that the pattern was remaining essentially the same as that at 1 ML, but that the adsorbate spots were increasing in number, intensity and sharpness relative to substrate spots, with a possible removal of the splitting of some of the adsorbate spots. In our earlier LEED/AES experiments (Chapter II and Ref. 18), it had been observed that at exposures around 10 ML the copper substrate spots were no longer visible and the adsorbate spots were qualitatively the same as those

of a Ag(111) 1x1 pattern. The normal-emission HeI photoemission spectrum collected at this exposure was very similar to that of the Ag(111) spectrum of Spears et al.[23]

Finally, the photoemission intensities of the silver and copper features confirmed the results of the LEED/AES experiments. The relative intensities of the silver and copper valence bands were normalized to that for 1 ML. An empirical function which consisted of a scaled and shifted clean copper spectrum was used to fit the residual copper features. The silver intensity was obtained by subtracting the empirical function from the spectrum and then summing the intensity of the individual channels. These results were then compared to the predictions of a model including attenuation effects, a description of which is in Appendix 1. A summary is given in Table III. However, these results must be approached with caution: the cross sections of the silver valence bands may be changing with exposure.

As discussed in Chapter II, this Cu(001) sample exhibited only one of the two possible orthogonal domains of the c(10x2) structure. This may have been caused by the slight misalignment ($\pm 1^{\circ}$) of the crystal face from (001) and the subsequent breakdown of the degeneracy of the [100] and [010] directions due to steps.

C. PHOTOEMISSION RESULTS

The photoemission spectra shown in Figures 2 through 16 include the photon energy range of 6-32 eV and exposures of 1/2, 1, 2, 3, 4, and 5 monolayers of c(10x2)Ag/Cu(001), as well as clean Cu(001) and

Ag(111).[24] They are organized with the Cu(001) substrate spectra bottommost, the Ag(111) topmost and the c(10x2)Ag/Cu(001) spectra between, running from lowest exposures at the bottom to highest exposures at the top. All copper and Ag/Cu(001) spectra were collected at normal emission with the same set of angles, as illustated in Figure 1. The Ag(111) spectra were also taken at normal emission, with the orientation shown in Figure 1. This was done to facilitate the comparison of the c(10x2) spectra with those of the Ag(111). It is especially important that the surface Brillouin Zones of the Ag(111) and the c(10x2)Ag were oriented the same with respect to the Poynting vector and polarization of the radiation.

Figure 2 shows spectra taken at $h\nu$= 6, 7, and 8eV. The major point of interest here is the development of a precursor to the Ag(111) surface state that occurs near E_F. This is most easily seen in the 7 and 8eV spectra, where the silver state grows in continuously, while the copper features are slowly diminishing. Also of interest is the absence of a silver overlayer feature corresponding to Band 6 in Ag(111), which is present at $h\nu$ = 6, 7, and 8eV at B^F near 1-2 eV. This will be discussed in detail in the next section.

The spectra taken at $h\nu$= 9, 10 and 12 eV are shown in Figures 3 and 4. The precursor surface state is again present at $h\nu$ = 9eV, although it is growing in on top of a copper feature near E_F. In this photon energy range, the overlap of the silver and copper features is greatest but the resolution is sufficient in most spectra to separate adsorbate and substrate contributions. Although it is

impossible to locate any more silver overlayer features at $h\nu$= 9eV, perhaps because of the copper substrate features and the decreasing transmission function of the analyzer at low kinetic energies, several silver overlayer states are observable at $h\nu$= 10 and 12eV.

At $h\nu$= 10eV, a pair of silver features can be seen to be developing near B^F= 4.5eV and a weak peak possibly corresponding to Band 6 of Ag(111) is seen at B^F= 3.5eV at 3, 4 and 5 monolayers exposure. However, the peak at 3.5eV may be a residual copper feature at this photon energy. In the 12eV spectra, these same features are observable, and possibly a more tightly bound pair near B^F= 6eV. The first, near B^F= 5.5eV, is clearly identifiable but the second, near 6eV, may be an artifact of the analyzer transmission function. At this photon energy, the feature at 3.5eV may be a silver peak. The surface state precursor is obscured by the copper features near E_F at $h\nu$= 10 and 12eV.

As the photon energy is increased, the bulk bands move toward the centers of the three dimensional Brillouin Zones of silver and copper, and the overlap of adsorbate and substrate features decreases. This is apparent in Figures 5 and 6, where spectra taken with $h\nu$= 14 and 16eV are shown. At $h\nu$= 14eV, a trio of silver features near B^F= 4.6eV, a shoulder, a peak and a shoulder, is easily visible as is a weaker feature at higher coverage and binding energy, near B^F= 5.5 eV. The high binding energy shoulder at 4.9eV may be a copper feature in the $h\nu$= 14 and 16eV spectra. At binding energies above that, peaks are not identifiable, except at the highest

exposures. Similarly at 16eV, the large shoulder-peak-shoulder trio near 4.6eV is quite prominent and weaker features near 5.6 and 6.8eV are observable at higher coverages. A very weak peak near B^F= 3.5eV also persists in these spectra at some of the higher exposures. At these and greater photon energies, the higher exposure c(10x2)Ag/Cu(001) surfaces have spectra that are very similar in appearance to the bulk Ag(111) spectra, if the copper features at lower binding energies are ignored. This is emphasized by the decreasing electron escape depth with increasing electron (and thus photon) energy, which serves to amplify the Ag overlayer/Cu substrate spectral intensity ratio. The absence of Band 6 and hence the failure of the lower photon energy spectra of the higher exposure samples to closely mimick the Ag(111) spectra will be discussed in the next section.

The above trends are continued in Figures 7 and 8, showing the spectra collected with hν= 18eV and 20eV. In these spectra, many silver overlayer features are easily observable but the peak and shoulder pair near B^F= 4.8eV is most prominent. Less intense features are seen in the high-exposure samples at higher and lower binding energies: near B^F= 4.3, 5.6, 6.1, and 6.9eV. The weak feature near B^F= 3.5eV is about to be lost due to overlap with the intense substrate d-bands but is still visible at higher coverages at hν= 18eV. However, it may merely be the trailing edge of the Cu bands near B^F= 3eV.

In Figures 9, 10, 11 and 12, the spectra taken at hν= 21, 22, 23,

and 24eV are shown. The features at B^F= 4.3, 4.7, 4.8, 5.6, 6.1, and 6.9eV are present at all four photon energies, with the shoulder-peak pair near 4.7eV being among those most prominent. The feature at B^F= 6.9eV at 5 ML is absent at $h\nu$ = 23 and 24eV, lost in the broadening tail of the other peaks. In these spectra the peak at 4.3eV is quite strong, particularly at exposures of 2 and 3 monolayers of silver. It is enveloped by the broadening peak at 4.8eV at higher exposures, where it becomes a shoulder on the leading edge of the silver d-bands. Also, the peaks at greater binding are undergoing a relative increase in intensity, particularly at exposures of 4 and 5 monolayers, thus mimicking the behavior of the peaks in the Ag(111) spectra. This contributes to the difficulty in observing the feature at B^F= 6.9eV at 5 ML.

The spectra taken at $h\nu$= 26, 28, 30, and 32eV are plotted in Figures 13, 14, 15 and 16. These continue the trends observed in Figures 9-12, but the degraded resolution causes a larger sampling of k-space and hence a more significant averaging over parts of the Brillouin Zone. The most striking features are those at exposures of two monolayers, where, as before, a strong separate peak at B^F= 4.2eV is present, before it becomes a shoulder at higher exposures. Also note the very strong resemblance between the silver overlayer features at higher exposures and the Ag(111) spectra.

Figure 17 contains expanded plots of a select group of spectra. At photon energies of 26eV and above, a broad feature is present in the Ag(111) spectra at a kinetic energy of 17eV with respect to the

Fermi Level ($B^F = h\nu - 17eV$). The highest exposure c(10x2)Ag/Cu(001) samples also displayed this peak at $h\nu \geq 28eV$, as can be seen in Figure 17.

D. DISCUSSION

1. DISPERSIVE BEHAVIOR

The above data were collected over the range of $h\nu$ = 6–32eV and at normal emission. The component of momentum parallel to the surface is zero and the component perpendicular to the surface is equivalent to the total crystal momentum. Defining the z-axis as perpendicular to the surface and the x-axis and y-axis in the plane of the surface, $\underline{k} = \underline{k}_z$ and $\underline{k}_{(x,y)} = 0$. Thus this is a direct probe of the dependence of the dispersion relations upon the perpendicular component of the crystal momentum and three-dimensionality. Energy conservation can be expressed in the following form:

$$B^F = h\nu - KE - \phi = h\nu - KE_{AN} - \phi_{AN}, \qquad (1)$$

with KE (KE_{AN})the kinetic energy in the vacuum (analyzer), $h\nu$ the photon energy, B^F the binding energy with respect to the Fermi level, and ϕ (ϕ_{AN})the work function of the crystal (spectrometer/analyzer).

For normal emission from Ag(111), the final state is a particularly well-defined, single state.[22,26] The final state of the photoelectrons emitted from the c(10x2)Ag adlayers is not well understood. To avoid any unnecessary and possibly prejudicial

assumptions concerning the final state, the comparison of the overlayer and Ag(111) dispersion relations will be made empirically by plotting the binding energies versus photon energy. Figures 18-22 are plots of the B^F of the silver features versus photon energy for 1, 2, 3, 4 and 5 ML exposures, respectively. Figure 23 is a plot of the Ag(111) data versus photon energy. Separating the silver adsorbate from the copper substrate features was sometimes difficult. Any silver feature overlapping with the strong copper d-band peaks near B^F = 2-3eV was essentially lost. On the other extreme, the weak copper feature at $B^F \geq$ 5eV caused significant problems in assignment of weak peaks and shoulders in the region.

A careful examination of the binding energies(B^F) with respect to the Fermi level shows marked changes in going from one to two to three monolayers and demonstrates a convergence toward Ag(111)-like behavior at exposures of 4 and 5 ML. Each of the lower coverages will be discussed separately.

ONE MONOLAYER

At one monolayer exposure, the geometrical structure of the adlayer is known to be an atomic monolayer film and the valence electronic structure of the adlayer has been shown to be two-dimensional in Chapter II. In Figure 18, the silver features of the one monolayer coverage sample are shown to not disperse with photon energy and thus be independent of k_z. The scatter in the points merely reflects the difficulty in determining the B^F of these weak features, particularly in light of the flat bands of Figure 19.

This is direct confirmation of the 2-dimensional electronic structure found in the off-normal bandmapping experiment of Chapter II. As discussed in that chapter, if the the contribution of the Cu(001) surface is neglected, then the dominant symmetry of the potential will be C_{6v} at one monolayer. The features observed are attributed to the $A_1(C_{6v})d_{3z^2-r^2}$ state (B^F = 4.2eV), the spin-orbit-split $E_1(C_{6v})d_{xz,yz}$ (B^F = 4.8eV) and the $A_1(C_{6v})$s state (B^F = 6.3eV). Weak features near B^F = 3.6, 5.2 and 8 eV are in some of the spectra. These are due to transitions of the underlying Cu(001) substrate. The symmetry forbidden transition originating from the silver $E_2(C_{6v})d_{xy,\ x^2-y^2}$ state is not observed.

TWO MONOLAYERS

At two monolayers (Figure 19), C_{3v} symmetry would be present. Experimentally, the bands are still observed to be flat and qualitatively the same as for one monolayer, except that the lowest band (greatest B^F) has shifted from B^F= 6.4eV at one monolayer to 6.7eV at 2 monolayers. This may be a manifestation of Density-of States (DOS) broadening in going from two- to three-dimensionality, since band width should increase with slab thickness.[11]

Under C_{3v} symmetry, the representations and selection rules are slightly different, with the abovementioned states essentially the same. Operating under C_{6v} selection rules, the transition from the E_2 state is forbidden. In going from 1 to 2 ML, this $E_2(C_{6v})$ state becomes $E(C_{3v})$, which is symmetry allowed. A weak feature near B^F = 5.4eV is seen at some photon energies at exposures of 1

amd 2 ML, but it is believed to be due to the tail of the Cu(001) feature at B^F = 5.2eV. From the off-normal study, it is known that the E_2 state should be in this region of B^F. Perhaps it is obscured by the copper peak or the C_{6v} contribution to the C_{3v} potential dominates it to the extent that the transition is still essentially forbidden. ($\underline{A}\cdot\underline{p}$ vectoral alignment also militates against a large partial cross section at normal emission, since it is only allowed for the in-surface-plane component of the polarization, $\underline{A}_{(x,y)}$. However the same is true for the E_1 state, which nonetheless has significant intensity.)

The features near B^F = 4.7 and 4.9 eV at 1 and 2 ML are assigned as the spin-orbit-split doublet of the $Y_2^{\pm 1}$ [$E_1(C_{6v})$ or $E(C_{3v})$] state. The observed splitting and RMS scatter at 1 ML is 0.26 ± 0.05 eV and at 2 monolayers it is 0.25 ± 0.04 eV. These values agree well with that of 0.24eV found in the resonance lamp experiment for coverages near one monolayer, as discussed in Chapter II.

THREE MONOLAYERS

At three monolayers (Figure 20), qualitatively new behavior is observed. For all adlayers thicker than two monolayers, there will always be a C_{3v} symmetry interface layer and a C_{3v} symmetry surface layer sandwiching octahedral symmetry layers between them, assuming a layer-by -layer and face-centered-cubic growth pattern. At three monolayers, the first octahedral layer will be present and experimentally two new bands are observed. One, near B^F = 5.5 eV, overlaps with the copper substrate feature but is much stronger than

before. The other, at B^F = 6.1 eV, has no substrate complications. Moreover, the band structure at $h\nu \geq$ 26eV is distinctly bulk-like in that there are now 5 separate levels between B^F = 4.5eV and B^F = 7eV, corresponding to Bands 1, (2,3), 4, 5, and 6 of Ag(111). There also appears to be the beginning of dispersion in Bands d and e at $h\nu \leq$ 20eV.

The feature at B^F = 4.2eV is not one of the bulk bands but appears to be the residual $A_1(C_{3v})$ state of the surface layer, and possibly of the interface layer as well. This explains the shoulder seen near 4eV in the bulk Ag(111) spectra, previously interpreted as being due to indirect transitions.[22] Looking at the spectra in Figures 10-16, this feature can be seen to persist as a separate peak even up to 4 monolayers, where it finally becomes enveloped in the broadening Bands d and e.

A peak at B^F = 3.5 eV is seen at $h\nu$ = 10-16 eV at exposures of 3-5 ML. It appears to be due to the copper substrate spectral structure but it may also be a dispersive s-p state away from the bulk zone center.

The success of the group theoretical analysis in explaining the new bands seen at 3 monolayers is the strongest evidence to date that the growth mode is layer-by-layer, at least up to coverages of three monolayers. Considering that only 100 atoms are necessary to observe bulk-like effects in Au clusters,[27] the absence of any other bands at one and two monolayer coverages is convincing evidence of their planar nature, and supports the hypothesis of continued layer-by-layer

growth.

FOUR AND FIVE MONOLAYERS

Continuing to the 4 and 5 monolayer coverages (Figures 21 and 22), the bands remain essentially stationary at $h\nu \geq$ 26eV, but dispersion is observed in Bands d and e as the photon energy approaches 10eV. This mimicks what is observed for Ag(111) in Figure 23 and corresponds to the dispersion occurring away from Γ and toward L in the bulk three-dimensional Brillouin Zone, as discussed in Chapter IV. The appearance of states near B^F = 3.5eV may be related to the dispersion of the bulk Band 6 up to the Fermi energy near the L point. But even without that connection, the features near B^F = 4.7eV are moving upward steadily in going from $h\nu$ = 20 to 10 eV in the 5 monolayer system.

The gradual, continuous development toward bulk band structure is consistent with a layer-by-layer growth pattern. At the five monolayer exposure, there are approximately 6×10^{15} atoms of Ag per square centimeter and a 5 ML slab would be approximately 13Å thick. At 5×10^{15} atoms/cm^2, the electronic density of states of the Au clusters studied by Lee et al[27] is very bulk-like. Assuming hemispherical cluster growth, this implies that bulk behavior is associated with thicknesses or heights of 10-20Å. In this experiment the perpendicular direction alone is being probed. If significant island formation were occuring in the silver overlayer, heights of twice the quoted silver exposure could well be expected and the transition from two- to three-dimensionality would be much more

rapid. Moreover, the continued observation of the $A_1(C_{3v})$ state at $B^F = 4.3$eV suggests the existence of large sections of an intact hexagonal topmost layer.

The question arises concerning the absence from the overlayer spectra of an intense, sharp feature for Band 6 at $B^F < 4$eV. The only silver overlayer features near the Ag(111) Band 6 at $h\nu < 14$eV are the weak, flat structure at $B^F = 3.5$eV and the broad, intense precursor to the Ag(111) surface state near E_F. At the other extreme, sharp, intense silver overlayer peaks are seen at $h\nu \geq 14$eV at $B^F \geq 4$eV. There are two possible explanations for this behavior, neither of which rules out the other.

(1) Interactions with the substrate affect Band 6. Band 6 at $B^F < 4$eV and the Ag(111) surface state are of s-p character, while Bands 1-6 of Ag(111) at $B^F \geq 4$eV are mainly of d character. Calculations[8] have shown that adsorbate d levels can behave as isolated core states and may not participate in interactions with the substrate. On the other hand, delocalized s and p electrons would be the most likely candidates for interaction with the substrate. Hence, substrate-adsorbate bonding interactions, which must be occurring to some extent because of the observed stability of the overlayer on the Cu(001) surface, would not perturb the adsorbate d levels ($B^F \geq 4$eV) but rather would severely affect the sp states, i.e. Band 6 at $B^F < 4$eV and the surface state.

(2) Spatial localization of the electrons inside the slab could affect the electronic transitions. For the initial state electrons,

the slightly different inner potential and the symmetry break at the Ag/Cu interface would serve to trap the electrons in a spatially localized region in the z-direction. The thickness of the overlayer slab would constitute the width of the real space localization. Using the Heisenberg Uncertainty Principle, $\Delta z \Delta k_z \geq 1/2$, the uncertainty in the perpendicular momentum can be found. Assuming layer-by-layer growth and a monolayer thickness of 2.5Å, Δk_z would be 0.20Å^{-1} for 1 ML and 0.04Å^{-1} for 5 ML. Because the entire Γ to L distance in reciprocal space is 1.33Å^{-1} in Ag(111), the initial state averaging effect will be severe at lower coverages but may not constitute a large effect at greater thicknesses.

Considering the final state electrons, the situation is distinctly different. A final state electron with a crystal momentum of 1.3Å^{-1} (near L of Ag(111)) would would have a de Broglie wavelength of close to 5Å, while a final state electron with a crystal momentum of 2.6Å^{-1} (near Γ of Ag(111)) would have a wavelength of about 2.5Å. Assuming a final state similar to Ag(111) for the silver overlayer, the spectra at $h\nu < 10$eV have a final state with wavelengths near 5Å, while those at $h\nu > 20$eV have final state wavelengths closer to 2.5Å. A 5 ML slab would be only 12.5Å thick. Moreover, the center slice of octahedral symmetry would be only 7.5Å wide. Thus, even for the 5 ML slab, the de Broglie wavelength of the final state at $h\nu < 10$eV would be almost as large as the octahedral slice width. This suggests that the "Three-step" concept of photoemission, which is the basis of the Direct Transition Model analysis of the valence band structure of such

systems as Ag(111), will fail at the lower photon energies. There is no well-defined crystal momentum final state inside the overlayer at these energies. However, the similarity of the sp plateau intensity behavior in the overlayer and that of Ag(111), as discussed below, may in fact indicate a developing Band 6.

This, in turn, implies that no sharp peaks should be observed at any coverages, which is contrary to observation. However, at the lowest coverages there is no perpendicular periodicity and hence no effect. Only as the z-direction develops thickness and periodicity does any of the above arguments have any meaning. It seems as if the normal emission spectra are those of a "one-dimensional" atomic system at low coverages.

2. DEVELOPMENT OF Ag(111) SPECTRAL CHARACTERISTICS

Besides the development of normal emission dispersion, there are several other facets of spectral behavior peculiar to Ag(111) that are seen to develop in the c(10x2)Ag overlayers.

BAND 7 RESONANCE

A sharp variation in intensity of the d-band peaks is observed in Ag(111) at $h\nu$= 21-24 eV. It is caused by the matching of the photon energy and the energy separation between the initial state d-bands and a flat region of Band 7 near Γ, the center of the bulk Brillouin Zone. This is also observed at 4 and 5 ML exposures in c(10x2)Ag.

While it is extremely difficult to fit each peak accurately, it is possible to measure the intensities of the top and bottom halves of the Ag VB. Figure 24 shows a comparison of these integrated

intensities for Ag(111)[24] and c(10x2)Ag/Cu(001). It is obvious that the cross-sections resonance seen in Ag(111) is also occurring in the adlayers, although to a diminished degree. Qualitatively, the resonance is observable in the raw spectra for the above systems from $h\nu$ = 20eV to $h\nu$ = 26eV.

This behavior occurs in Ag(111) at Γ, where atomic effects should dominate. Atomic Ag spectra[28] do show a distinct increase in cross section magnitude over the energy range of $h\nu$ = 17–20 eV. The results over the range of $h\nu$ = 20–27 eV are too incomplete to dismiss the possibility of an atomic cross section resonance occuring there. Nevertheless, the resonance is not observed at lower exposures of the c(10x2)Ag system and the effect is seen to grow stronger with increasing exposure.

CONSTANT KINETIC ENERGY FEATURE

Another feature identified with Ag(111) is the constant kinetic energy peak at 17eV with respect to the Fermi level. This is also due to the flat region of Band 7 of Ag(111), near the center of the the bulk Brillouin Zone. Electrons scatter into it, producing a peak that appears to move across the spectra at $B^F = h\nu - 17eV$ for $h\nu$ = 26–32 eV.[22] At 28eV and 30eV photon energies, this feature is observable at 4 and 5 monolayers, and at $h\nu$= 32eV at 5 monolayers, as shown in Figure 17. This is a strong indication of bulk-like final state behavior in the silver overlayer.

SURFACE STATE

At lower photon energies, $h\nu$ = 6–12 eV, the Ag(111) surface state

is present near the Fermi level. At some of these photon energies, copper features obscure this spectral region but for $h\nu$ = 7-9eV the development of a precursor surface state is easily seen. Table IV contains a summary of surface state data taken from the $h\nu$ = 8eV spectra. (The $h\nu$ = 8eV spectra have a flat Cu substrate background.) The binding energies were determined by visual inspection. The widths were found by fitting the Fermi edge step and surface peak with a gaussian step and a lorentzian peak function multiplied by a Fermi occupation function (T = 300°K). The gaussian step and occupation function were set to the value of the Fermi energy determined by visual inspection and the lorentzian mean was set to the peak energy, also found by visual inspection. The listed widths are the FWHM of the unabridged lorentzians. The Ag(111) values were taken from Chapter IV. Fitting the Ag(111) $h\nu$ = 8eV spectrum with the functions used on the overlayer spectra produced values consistent with those from Chapter IV. Also, despite the obstruction of substrate peaks, the B^F values of the overlayer peak determined at nearby photon energies were consistent with those from $h\nu$ = 8eV. The state has roughly the same binding energy as for Ag(111) but is much wider owing to the asymmetric tail on the higher binding energy side. This may be due to s-d interaction between the adsorbate and substrate[8] or the spatial localization effect described above.

At 3 and 5 monolayer exposures, the angular dependence of the precursor surface state was investigated at $h\nu$ = 8eV. All spectra were taken with the same parameters as shown in Figure 1, save that

the ARP analyzer was rotated off normal to obtain nonzero values of $k_{(x,y)}$. While no clean Cu(001) substrate off-normal spectra were available for direct comparison, the general appearance of the adsorbate spectra remained much the same and the intensity of the precursor state was estimated by linearly extrapolating the diminishing background back up to the Fermi edge.

At 3 monolayers, rotating in the $\bar{\Gamma}$-$\bar{T}$-$\bar{K}$ plane above and below the light polarization, the state was evident at $\theta_e = \pm 2^\circ$ ($k_{(x,y)} = \pm 0.032$ Å^{-1}) and at $\theta_e = \pm 5^\circ$ ($k_{(x,y)} = \pm 0.079$ Å^{-1}). In the $\bar{\Gamma}$-$\bar{\Sigma}$-$\bar{M}$ plane, the state was present at $\theta_e = \pm 2^\circ$, $\pm 5^\circ$, and $\pm 10^\circ$ ($k_{(x,y)} = \pm 0.158$ Å^{-1}), both towards and away from the light polarization. Rotating the analyzer in the $\bar{\Gamma}$-$\bar{\Sigma}$-$\bar{M}$ plane toward the polarization of the synchrotron radiation ($\theta_e > 0$), at $\theta_e = 15^\circ$ ($k_{(x,y)} = 0.236$ Å^{-1}) the precursor peak disappeared. At $\theta_e = 20^\circ$ ($k_{(x,y)} = 0.312$ Å^{-1}), the peak reappeared. Within the precision of our measurements, the state does not appear to be dispersing as a function of $k_{(x,y)}$. At an exposure of 5 monolayers, rotating in the $\bar{\Gamma}$-$\bar{\Sigma}$-$\bar{M}$ plane and toward the light polarization, the state was present at $\theta_e = 0^\circ$ and 2° but not at 5°. Again, there seems to be no dispersion with $k_{(x,y)}$.

The behavior at 5 monolayers is consistent with that observed by Hansson and Flodstrom[20] in Ag(111) at $h\nu = 10.2$eV ($k_{(x,y)} \leq 0.103$Å^{-1}). However, the three monolayer precursor seems to extend much further in $k_{(x,y)}$ space. It appears that the precursor state may be restricted to a smaller area of the

2-dimensional Surface Brillouin Zone as the overlayer becomes thicker and the valence bands become more 3-dimensional.

SP PLATEAU

The ratio of the sp plateau height to the valence band maximum is dependent upon the valence electronic structure of the system, as discussed in Chapter IV. The indirect transitions contributing to the sp plateau intensity are dependent upon the position of the bands near E_F, e.g. Band 6 of Ag(111). Figure 25 shows this ratio versus photon energy for clean Cu(001), 1-5 ML of c(10x2)Ag/Cu(001), and Ag(111). As the exposure is increased the behavior of the ratio converges toward that of Ag(111). This is yet another indication of the development of Ag(111)-like behavior in the metal overlayer. This specifically suggests that Band 6 is indeed developing in the silver overlayers.

SPECTRAL APPEARANCE

Finally, it is of interest to note the significant similarities between the spectra of Ag(111) and those of 5ML c(10x2)Ag/Cu(001). As an example, those at 23eV bear a striking resemblance if the Cu features are neglected. Qualitatively, this is strong evidence for the asymptotic approach of the c(10x2) Ag system toward bulk Ag(111).

E. CONCLUSIONS

Based upon the results of the LEED/AES calibration of Chapter II and the previous work discussed therein, the c(10x2)Ag/Cu(001) adlayer is assumed to be geometrically two-dimensional at coverages near 1 monolayer. It has been shown in the off-normal angle-resolved

photoemission experiment of Chapter II that the monolayer structure is also electronically two-dimensional. Here, conclusive evidence is presented to document the development of the valence bands of the c(10x2)Ag from a two-dimensional to three-dimensional electronic structure. The three monolayer results demonstrate the importance of developing a crystal field similar to that of the bulk. Higher coverages are necessary to acquire sufficient periodicity in real space to observe dispersion in the third dimension. By an exposure of 5 ML, the spectral behavior of the overlayer valence (and conduction) bands is very similar to that of Ag(111). This includes dispersion as a function of k_z, the Band 7 resonance, the constant kinetic energy feature, the Ag(111)-like surface state, the sp-plateau intensity profile and finally the detailed visual appearance of the spectra themselves.

Appendix 1

A MODEL FOR Ag-ADSORBATE/Cu-SUBSTRATE PHOTOEMISSION RATIOS

ASSUMING A LAYER-BY-LAYER GROWTH PATTERN[29]

SUBSTRATE

$$i_{Cu} = i^{o}_{Cu}\, e^{-z/z_o} \qquad (1)$$

i_{Cu}: photoemission intensity of the copper features including attenuation from the overlayer

i^{o}_{Cu}: photoemission intensity of the clean copper, bulk Cu(001)

z: overlayer thickness

z_o: escape depth of the substrate photoelectrons, through the adsorbate

NOTE: no correction for light attenuation

ADSORBATE

$$j_{Ag} = \sum_{k=1}^{n} j^{k}_{Ag} \qquad (2)$$

j_{Ag}: photoemission intensity from the silver overlayer

j^{k}_{Ag}: photoemission intensity from the kth monolayer of an overlayer slab n monolayers thick

$$j^{k}_{Ag} = j^{1}_{Ag}\, e^{-(k-1)t/t_o} \qquad (3)$$

j^{1}_{Ag}: photoemission intensity from the topmost monolayer of the overlayer, k=1

t: thickness of one monolayer

(k-1)t: thickness of the overlayer above the kth monolayer

t_o: escape depth of the adsorbate electrons, through the adsorbate

NOTE: $z = nt$ (4)

$$R_n = \frac{j_{Ag}}{i_{Cu}} = \frac{j^1_{Ag}}{i^o_{Cu}} \quad \frac{\sum_{k=1}^{n} e^{-(k-1)t/t_o}}{e^{-z/z_o}} \qquad (5)$$

In the case of a overlayer only one monolayer thick: k=n=1, z=t

$$R_1 = \frac{j^1_{Ag}}{i^o_{Cu}} \quad \frac{1}{e^{-t/z_o}} \qquad (6)$$

Defining a ratio normalized to the ratio at 1ML:

$$R'_n = \frac{R_n}{R_1} = \frac{\sum_{k=1}^{n} (e^{-(k-1)t/t_o}) \ (e^{\ z/z_o})}{e^{t/z_o}} \qquad (7)$$

Substituting z=nt and setting $t_o = z_o$ (same kinetic energy range)

$$R'_n = \frac{\sum_{k=1}^{n} e^{-(k-1)t/z_o}}{e^{-(n-1)t/z_o}} \qquad (8)$$

Eq. (8) was used to calculate the theoretical values of Table III.

REFERENCES

1. D. E. Eastman and W. D. Grobman, Phys. Rev. Lett. 30, 177 (1973).
2. I. Abbati, L. Braichovich, C. M. Bertoni, C. Calandra and F. Manghi, Phys. Rev. Lett. 40, 469 (1978); I. Abbati, L. Braichovich, A. Fasana, C. M. Bertoni, F. Manghi, C. Calandra, Phys. Rev. B23, 6448 (1981).
3. S.-L. Weng and M. El-Batanouny, Phys. Rev. Lett., 44, 612 (1980).
4. L. Gonzalez, R. Miranda, M. Salmeron, J. A. Verges, and F. Yndurain, Phys. Rev. B24, 3245 (1981).
5. G. C. Smith, C. Norris, C. Binns and H. A. Padmore, J. Phys. C 15, 6481 (1982).
6. R. Miranda, F. Yndurain, C. Chandesris, J. Lecante, and Y. Petroff, Phys. Rev. B25, 527 (1982); Surf. Sci. 117, 319 (1982).
7. M. El-Batanouny, D. R. Hamann, S. R. Chubb and J.W. Davenport, Phys. Rev. B27, 2575 (1983); M. El-Batanouny, M. Strongin and G. P. Williams, Phys. Rev. B27, 4580 (1983).
8. J. Tersoff and L. M. Falicov, Phys. Rev. B25, 2959 (1982).
9. D.-S. Wang, A. J. Freeman, H. Krakauer, Phys. Rev. B26, 1340 (1982).
10. B. R. Cooper, Phys. Rev. Lett. 26, 1316 (1973).
11. J. G. Gay, J. R. Smith, and F. J. Arlinghaus, Phys. Rev. Lett. 38, 561 (1977); Phys. Rev. B20, 1332 (1979); Phys. Rev. B21, 2055 (1980); Phys. Rev. B21, 2201 (1980); Phys. Rev. B22, 4757 (1980); Phys. Rev. B25, 643 (1982).
12. G. S. Painter, Phys. Rev. B17, 3848 (1978).

13. C. S. Wang and A. J. Freeman, Phys. Rev. B18, 1714 (1978); Phys. Rev. B19, 793 (1979); Phys. Rev. B21, 4585 (1980); Phys. Rev. B24, 4364 (1981).

14. O. Jepsen, J. Madsen and O. K. Andersen, Phys. Rev. B26, 2790 (1982).

15. P. D. Loly and J. B. Pendry, J. Phys. C 16, 423 (1983).

16. T. Mandel, G. Kaindl, W. D. Schneider, and W. Fischer, Submitted to Phys. Rev. Lett.

17. J. G. Tobin, S. V. Robey, L. E. Klebanoff and D. A. Shirley, LBL 14187, submitted to Phys. Rev. Lett.

18. J. G. Tobin, S. W. Robey, and D. A. Shirley, LBL-15133.

19. H. F. Roloff and H. Neddermeyer, Solid State Commun. 21, 561 (1977).

20. G. V. Hansson and S. A. Flodstrom, Phys. Rev. B17, 473 (1978).

21. D. Liebowitz and N. J. Shevchik, Phys. Rev. B17, 3825 (1978).

22. P. S. Wehner, R. S. Williams, S. D. Kevan, D. Denley and D. A. Shirley, Phys. Rev. B19, 6164 (1979).

23. D. P. Spears, R. Melander, L. G. Petersson and S.B.M. Hagstrom, Phys. Rev. B21, 1462 (1980).

24. J. G. Tobin, S. W. Robey, D. A. Shirley, W. J. Gignac, J. G. Nelson, and R. S. Williams, LBL-15135.

25. S.D. Kevan and D.A. Shirley, Phys. Rev. B22, 542 (1980).

26. N. E. Christensen, Phys. Status Solidi(B) 54, 551 (1972).

27. S.-T. Lee, G. Apai, M.G. Mason, R. Benbow, and Z. Hurych, Phys. Rev. B23, 505 (1981).

28. M. O. Krause, P. R. Woodruff and T. A. Carlson, J. Phys. B 14, L673 (1981); M. O. Krause, J. Chem. Phys. 72, 6474 (1980).

29. G. Ertl and J. Kuppers, "Low Energy Electrons and Surface Chemistry," Verlag Chemie, 1974, Pages 39-40.

30. P. S. Wehner, Ph.D. Thesis, Univ. of Cal.-Berk., 1978, unpublished.

TABLE CAPTIONS

Table I This is a summary of the resolution of the experiment. Contributions to the total resolution were assumed to add in quadrature. For $h\nu \leq 18$eV and $h\nu \geq 28$eV, the entrance and exit slits of the monochromator were the same and the monochromator resolution was taken directly from SSRL literature. For $20 \leq h\nu \leq 26$eV, the 2.5Å bandpass entrance and 0.8Å bandpass exit slit were used. The resolution was determined by mapping the entrance slit onto exit slit. The result was essentially an averaging of the 2.5Å and 0.8Å bandpasses.

Table II The spectrometer work functions for the adlayer systems and Ag(111).

Table III This is a summary of the observed and predicted Ag/Cu photoemission intensity ratios. They are normalized to the 1 ML value, such that $R'_n = R_n/R_1$ with $R_n = (j_{Ag}/i_{Cu})_n$. The subscript n represents the exposure in ML. The thickness of a monolayer is defined as t and assumed to be approximately 2.5Å. The escape depth of an electron of a given kinetic energy is z_o. These were taken from the "Universal Curve" of electron escape depths.[30] Appendix 1 is a derivation of the attenuation model.

Table IV Comparison of the binding energies with respect to the Fermi energy and the full widths at half maximum (FWHM) of the Ag(111) surface state and its precursor observed in c(10x2)Ag/Cu(001). All overlayer measurements were derived from data collected at normal emission for $h\nu$ = 8eV. The Ag(111) data is from Chapter IV.

Table I
Resolution

$h\nu$(eV)	ΔE_{MONO}(meV)	ΔE_{AN}(meV)	ΔE_{TOT}(meV)
6	25	60	65
7	34	60	69
8	45	60	75
9	57	60	83
10	70	60	92
12	29	60	67
14	40	60	72
16	52	60	79
18	65	60	88
20	55	60	81
21	60	60	85
22	66	60	89
23	73	60	94
24	79	60	99
26	93	60	111
28	158	60	169
30	181	60	191
32	206	60	215

Table II
Spectrometer Work Functions

Exposure (ML)	AVE ϕ_{AN}(eV)	± Stan. Dev.(eV)
0	4.53	±0.03
1	4.52	±0.02
2	4.49	±0.08
3	4.57	±0.06
4	4.53	±0.02
5	4.52	±0.02
AVE ± S.D.	4.53	±0.03
Ag(111)	4.55	±0.02

Table III
Ag/Cu Photoemission Ratios

$h\nu$(eV)	z_0(Å)	t/z_0		R'_1	R'_2	R'_3	R'_4	R'_5
16	15	1/6	Th.	1	2.2	3.6	5.2	7.2
			Exp.	1	2.9	3.9	4.6	6.3
21	10	1/4	Th.	1	2.3	3.9	6.0	8.8
			Exp.	1	2.9	4.7	5.5	8.7
32	7.5	1/3	Th.	1	2.4	4.3	7.1	10.9
	5	1/2	Th.	1	2.6	5.4	9.8	17.2
			Exp.	1	3.6	6.2	5.2	7.4

Table IV
Surface State

	B^F(eV)	Width (eV)
Ag(111)[24]	0.065 ± 0.004	0.111 ± 0.007
	Monolayers of c(10x2)Ag/Cu(001)	
5	0.10	0.7
4	0.11	1.0
3	0.14	1.2
2	0.11	1.4

FIGURE CAPTIONS

Figure 1. The geometry of the photoemission experiment is illustrated here: top - the real space relationships; bottom - the Surface Brillouin Zones in reciprocal space and their relationship to the plane containing the polarization A. The surface normal, n, the surface vector, v, the light polarization and the Poynting vector of the light are all in the horizontal plane.

Figure 2. The ARP spectra taken at $h\nu$= 6, 7, and 8eV are plotted versus the binding energy (B^F) with respect to the Fermi Level (E_F). The spectra are normalized to the largest feature in each spectrum. Cu(001) is at the bottom, followed sequentially upward by the spectra of c(10x2)Ag/Cu(001) of 1/2, 1, 2, 3, 4, and 5 monolayer exposure. The bulk, single-crystal Ag(111) spectrum is topmost. All of the data was collected at normal emission, either parallel to [001] of Cu(001) or [111] of Ag(111). In some of the plots, the Ag(111) spectra are expanded to more fully illustrate the surface state near E_F.

Figure 3. Same as Figure 2 with $h\nu$= 9, 10 eV.

Figure 4. Same as Figure 2 with $h\nu$= 12 eV.

Figure 5. Same as Figure 2 with $h\nu$= 14 eV.

Figure 6. Same as Figure 2 with $h\nu$= 16 eV.

Figure 7. Same as Figure 2 with $h\nu$= 18 eV.

Figure 8. Same as Figure 2 with $h\nu$= 20 eV.

Figure 9. Same as Figure 2 with $h\nu$= 21 eV.

Figure 10. Same as Figure 2 with $h\nu$= 22 eV.

Figure 11. Same as Figure 2 with $h\nu$= 23 eV.

Figure 12. Same as Figure 2 with $h\nu$= 24 eV.

Figure 13. Same as Figure 2 with $h\nu$= 26 eV.

Figure 14. Same as Figure 2 with $h\nu$= 28 eV.

Figure 15. Same as Figure 2 with $h\nu$= 30 eV

Figure 16. Same as Figure 2 with $h\nu$= 32 eV.

Figure 17. ARP spectra of 4 and 5 monolayer c(10x2)Ag/Cu(001) and Ag(111) at $h\nu$= 28, 30 and 32eV. Note the constant kinetic energy feature moving across the spectra at $B^F = h\nu - 17eV$.

Figure 18. This is a plot of the binding energy (B^F) with respect to the Fermi Level (E_F) of the silver overlayer features at one monolayer exposure versus the photon energy.

Figure 19. Same as Figure 18 but for an exposure of 2 monolayers.

Figure 20. Same as Figure 18 but for an exposure of 3 monolayers.

Figure 21 Same as Figure 18 but for an exposure of 4 monolayers.

Figure 22 Same as Figure 18 but for an exposure of 5 monolayers.

Figure 23 Same as Figure 18 but for Ag(111).

Figure 24 The ratio of the intensity of the high B^F half of the silver valence bands to the intensity of the low B^F half of the silver valence bands, plotted as a function of photon energy for the samples Ag(111) (filled circles) and 5 (filled triangles) and 4 monolayers (filled squares) of c(10x2)Ag/Cu(001). The ratio of the 5 ML values (including the RMS deviation) to the Ag(111) values is 0.57 ± 0.09.

The ratio of the 4 Ml values to the Ag(111) values is 0.52 ± 0.09 and to the 5 ML values is 0.92 ± 0.07.

Figure 25 The ratio of the sp plateau height to the valence band maximum, versus photon energy, for Cu(001), 1, 2, 3, 4, and 5 ML of c(10x2)Ag/Cu(001), and Ag(111).

ARP Diagram

$\theta_e = 0°$

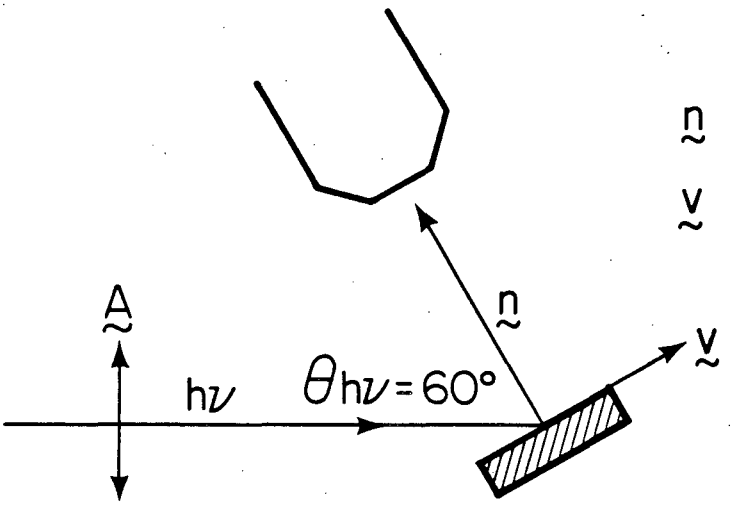

	Cu(001)	Ag(111)
n	001	111
v	110	$\bar{1}2\bar{1}$

Surface Brillouin Zones

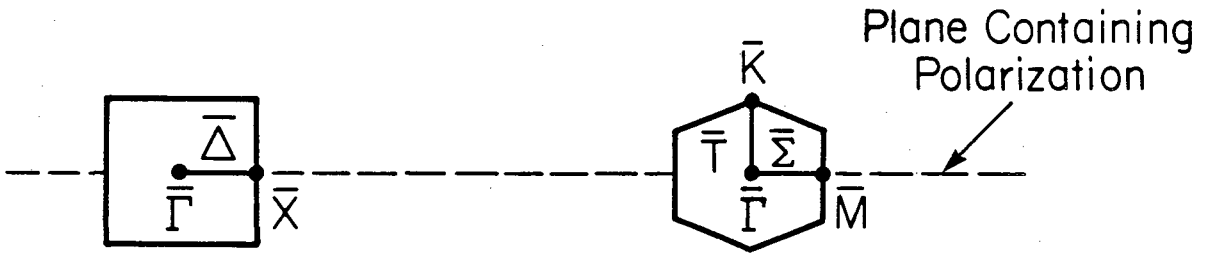

Cu (001)
$\bar{X} = 1.23 Å^{-1}$

c(10x2)Ag And Ag(111)
$\bar{M} = 1.25 Å^{-1}$

XBL837-981

Fig. 1

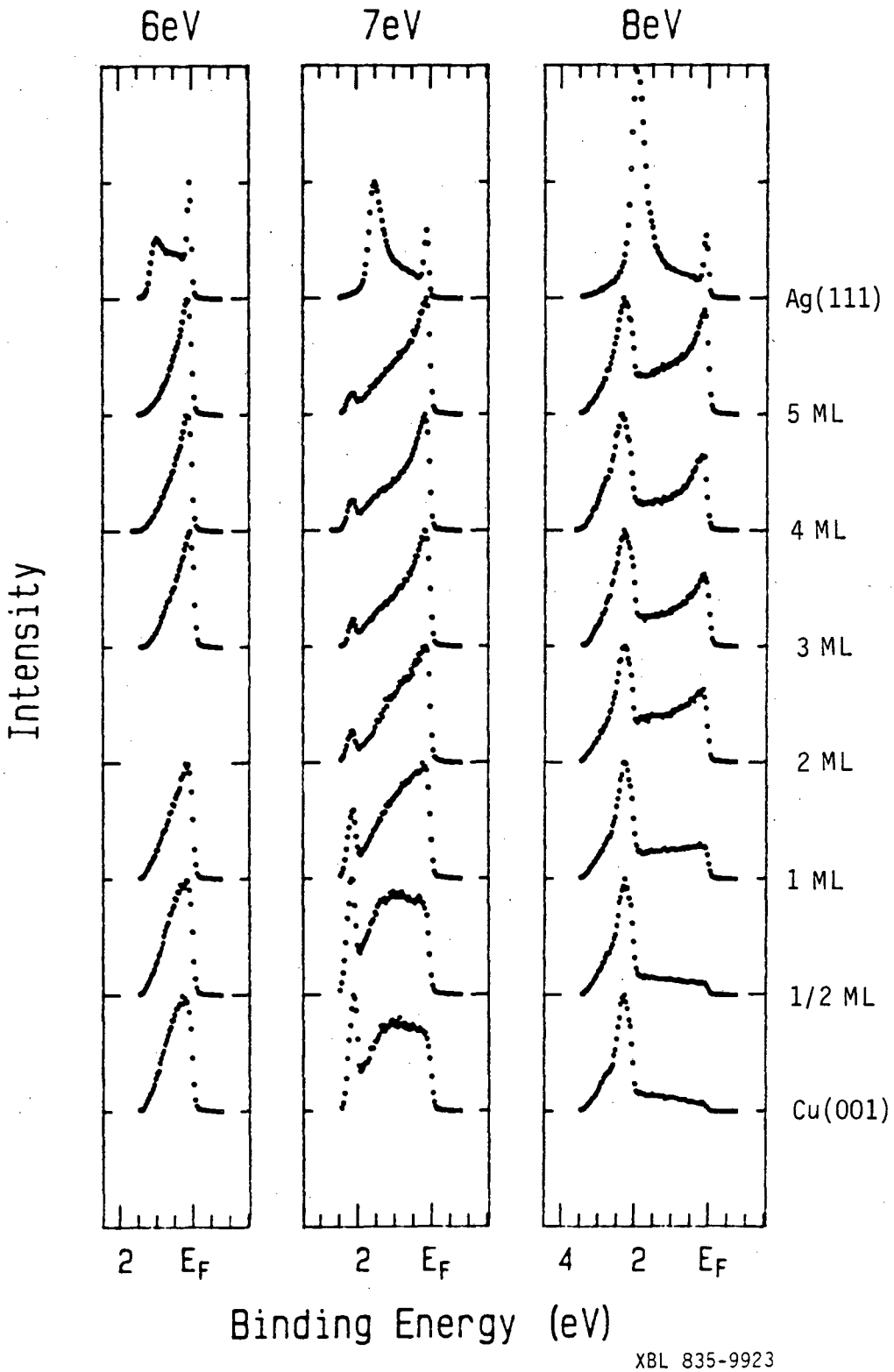
6eV
7eV
8eV
Ag(111)
5 ML
4 ML
3 ML
2 ML
1 ML
1/2 ML
Cu(001)
Intensity
2 E_F
2 E_F
4 2 E_F
Binding Energy (eV)
XBL 835-9923

Fig. 2

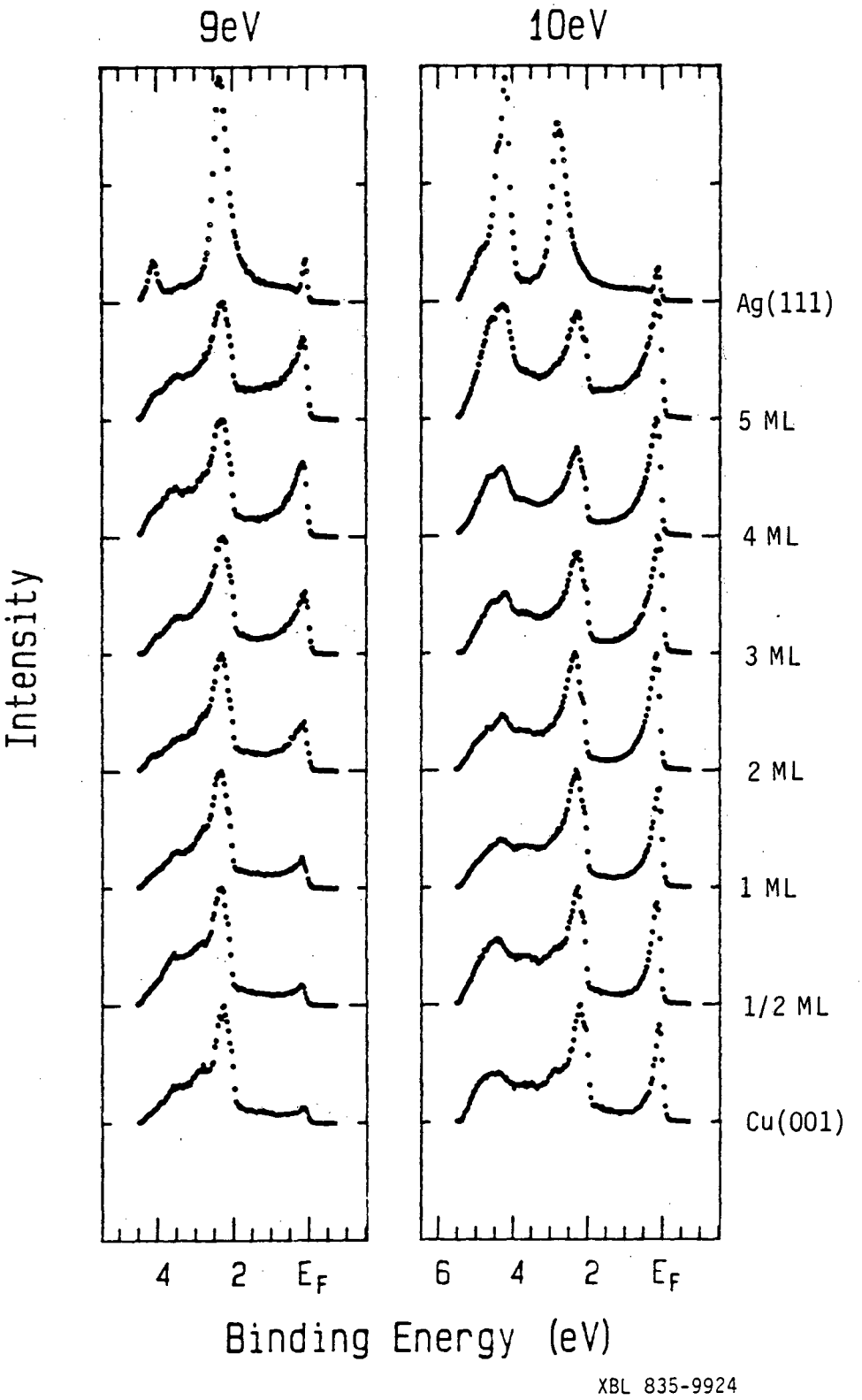
9eV
10eV
Ag(111)
5 ML
4 ML
3 ML
2 ML
1 ML
1/2 ML
Cu(001)
Intensity
4
2
E_F
6
4
2
E_F
Binding Energy (eV)
XBL 835-9924

Fig. 3

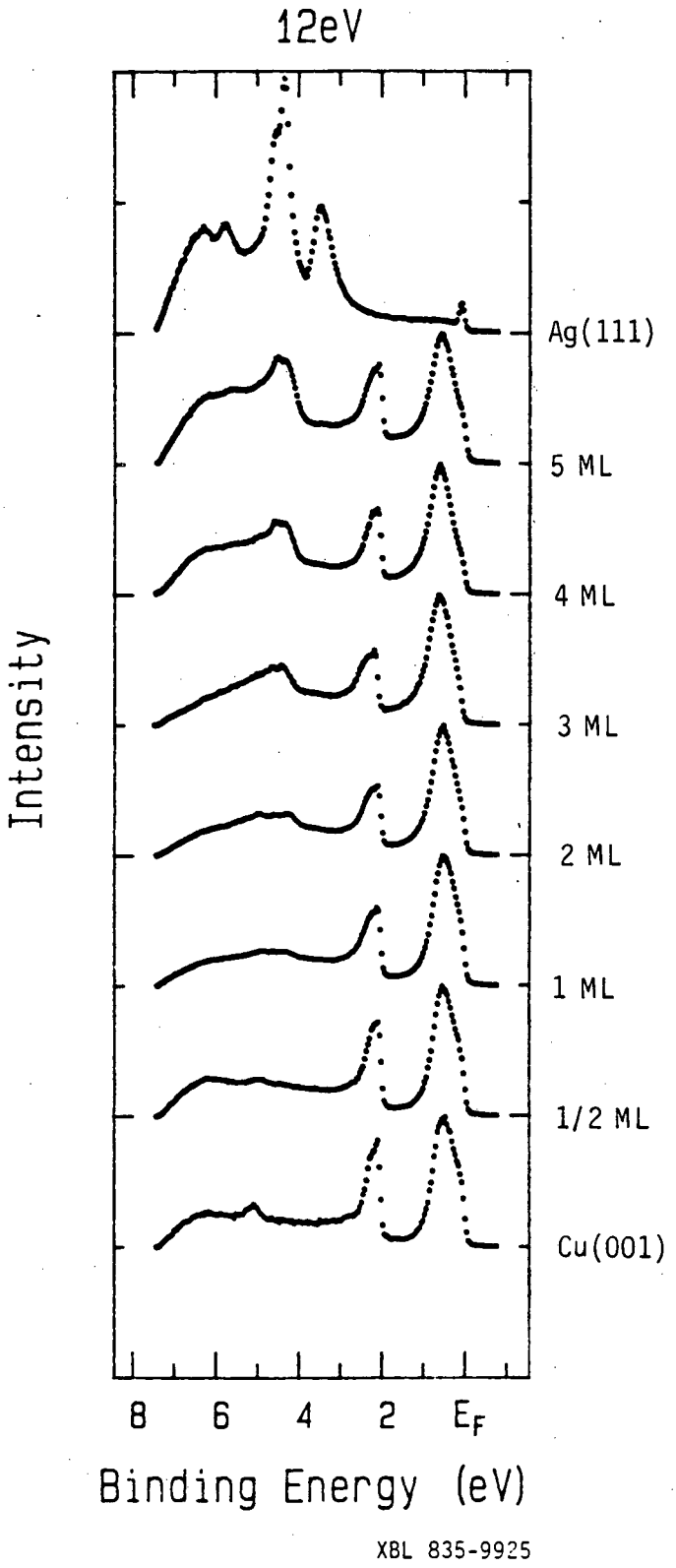
12eV
Ag(111)
5 ML
4 ML
3 ML
2 ML
1 ML
1/2 ML
Cu(001)
Intensity
8
6
4
2
E_F
Binding Energy (eV)
XBL 835-9925

Fig. 4

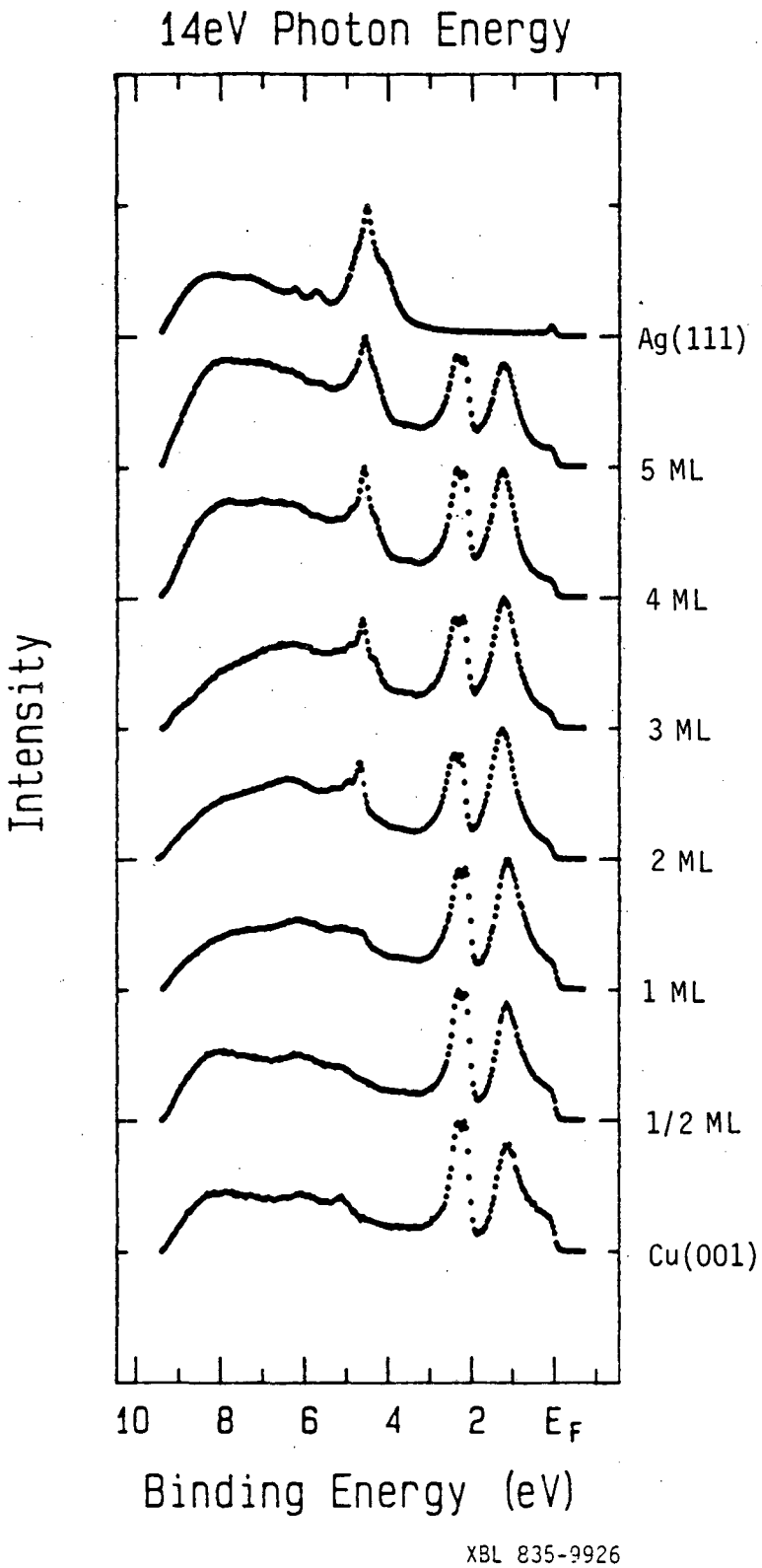
14eV Photon Energy
Intensity
Ag(111)
5 ML
4 ML
3 ML
2 ML
1 ML
1/2 ML
Cu(001)
10
8
6
4
2
E_F
Binding Energy (eV)
XBL 835-9926

Fig. 5

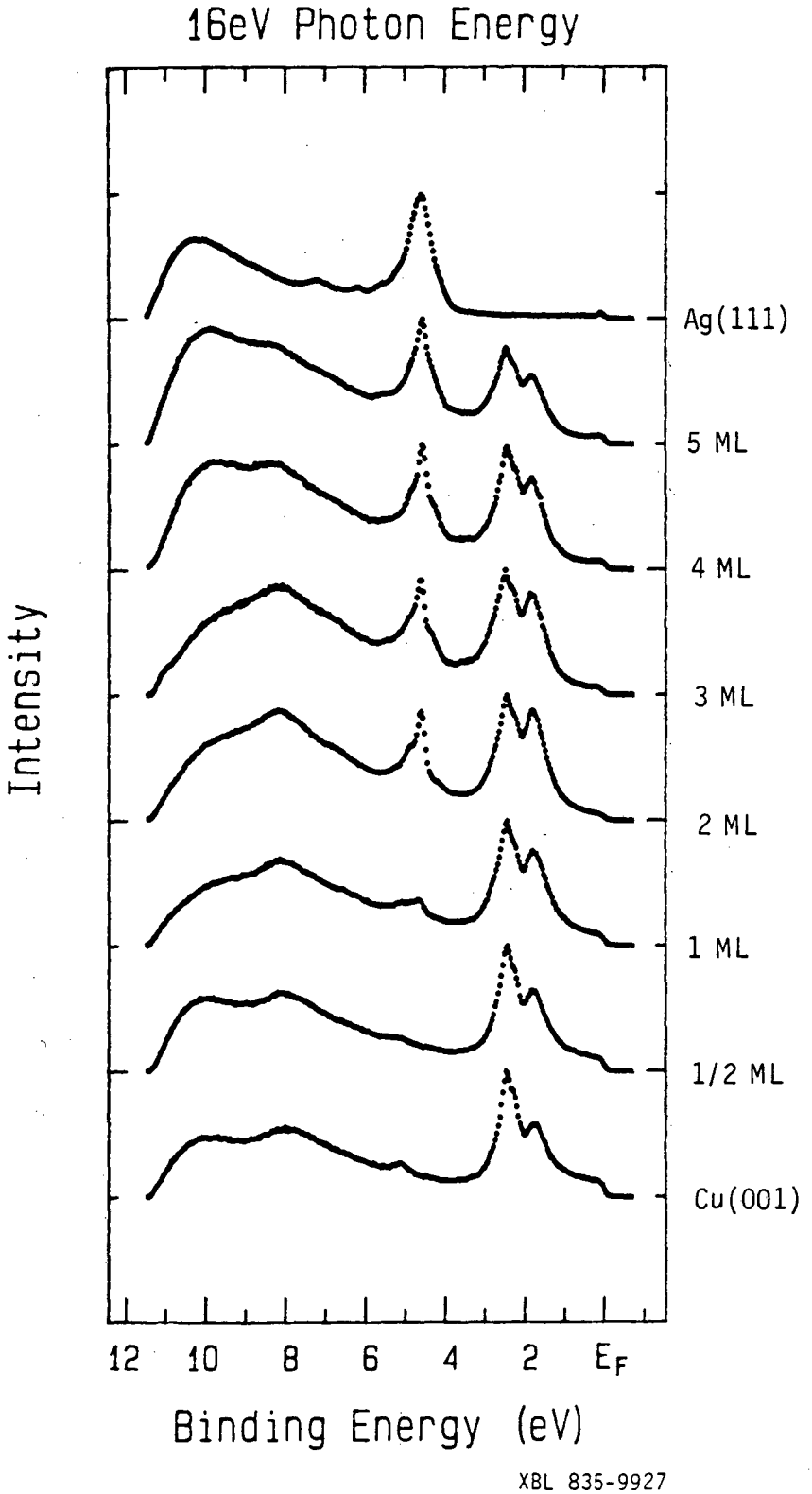
16eV Photon Energy
Ag(111)
5 ML
4 ML
3 ML
2 ML
1 ML
1/2 ML
Cu(001)
Intensity
12
10
8
6
4
2
E_F
Binding Energy (eV)
XBL 835-9927

Fig. 6

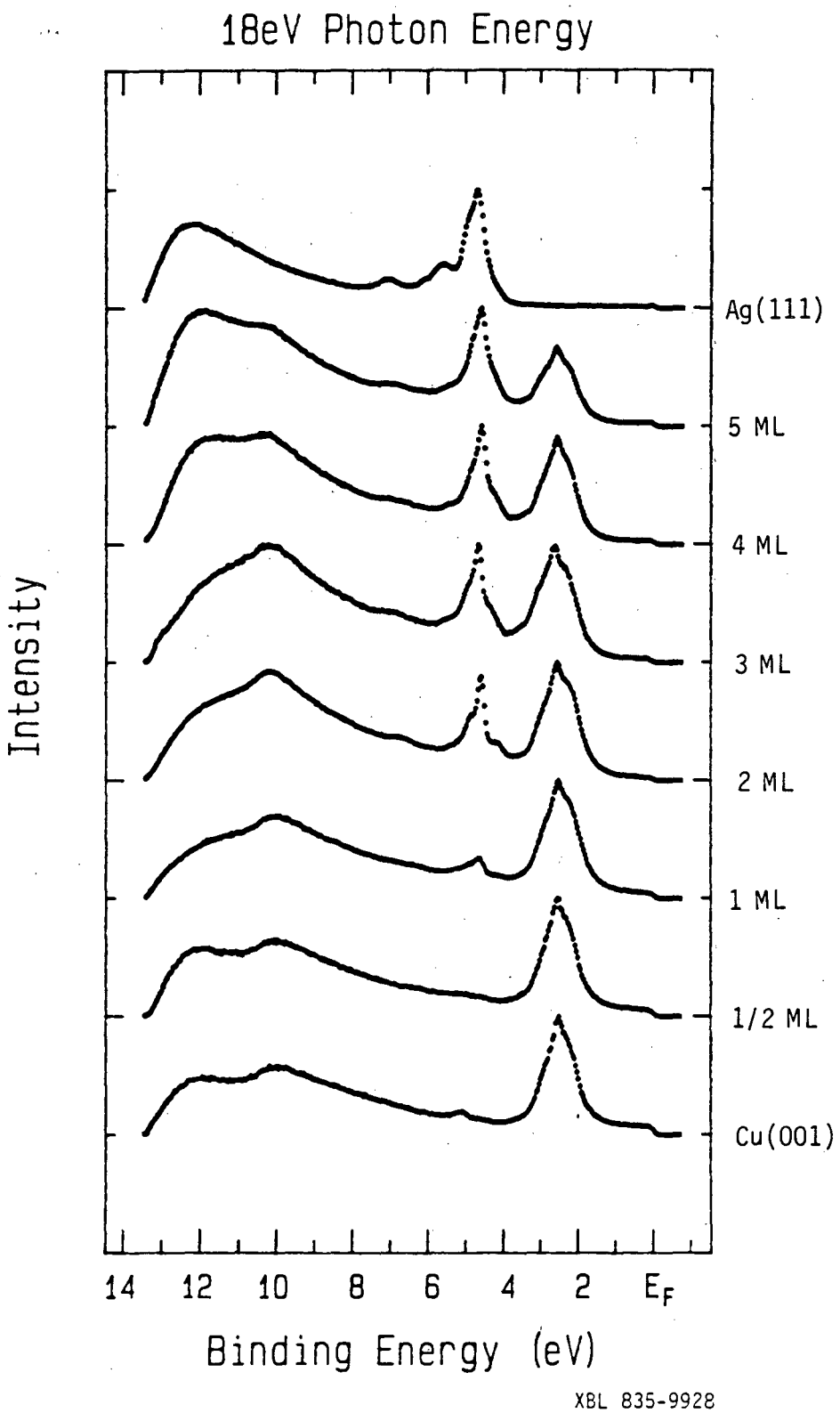
18eV Photon Energy
Intensity
Ag(111)
5 ML
4 ML
3 ML
2 ML
1 ML
1/2 ML
Cu(001)
14
12
10
8
6
4
2
E_F
Binding Energy (eV)
XBL 835-9928

Fig. 7

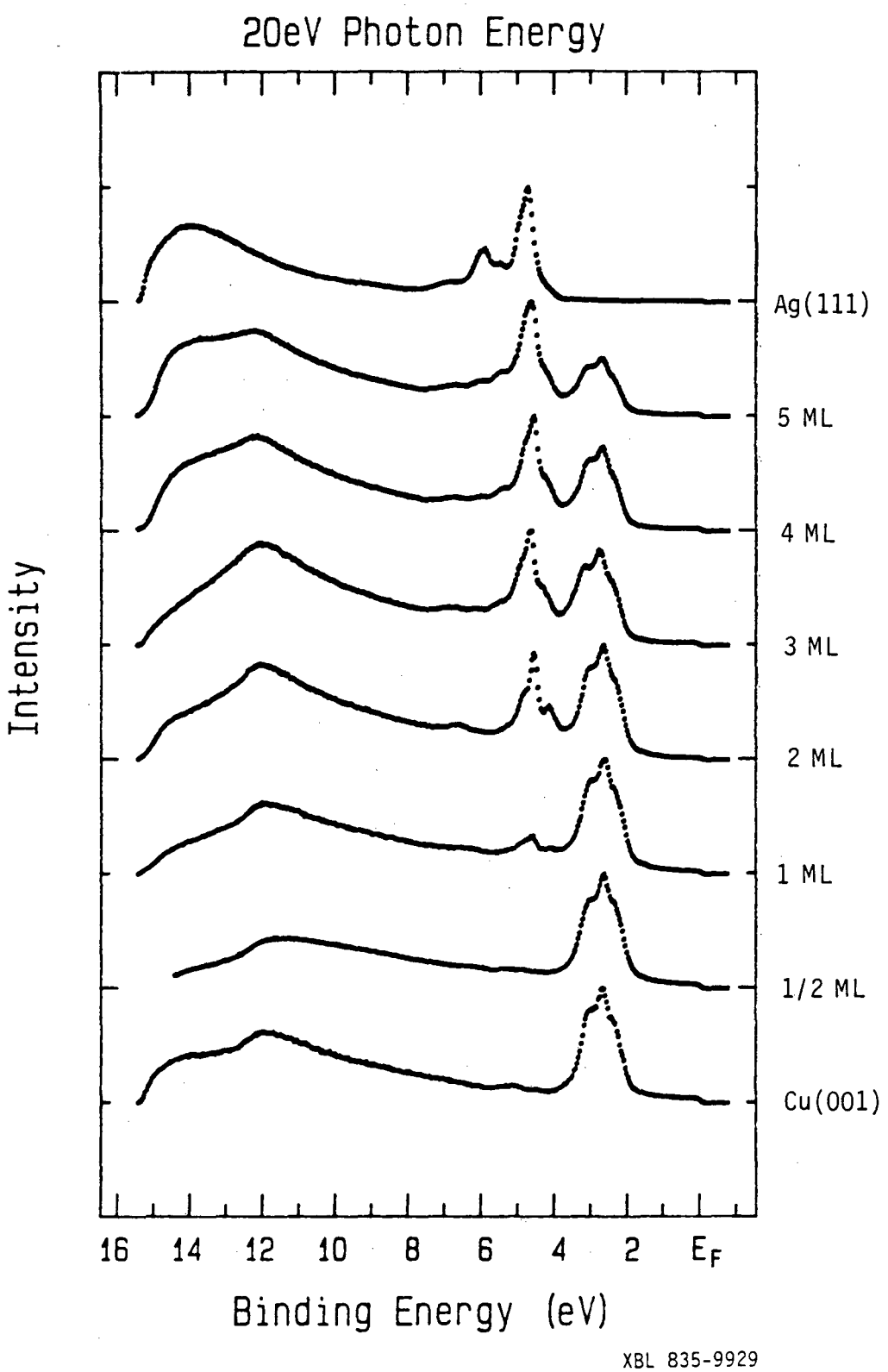
20eV Photon Energy
Intensity
Ag(111)
5 ML
4 ML
3 ML
2 ML
1 ML
1/2 ML
Cu(001)
16
14
12
10
8
6
4
2
E_F
Binding Energy (eV)
XBL 835-9929

Fig. 8

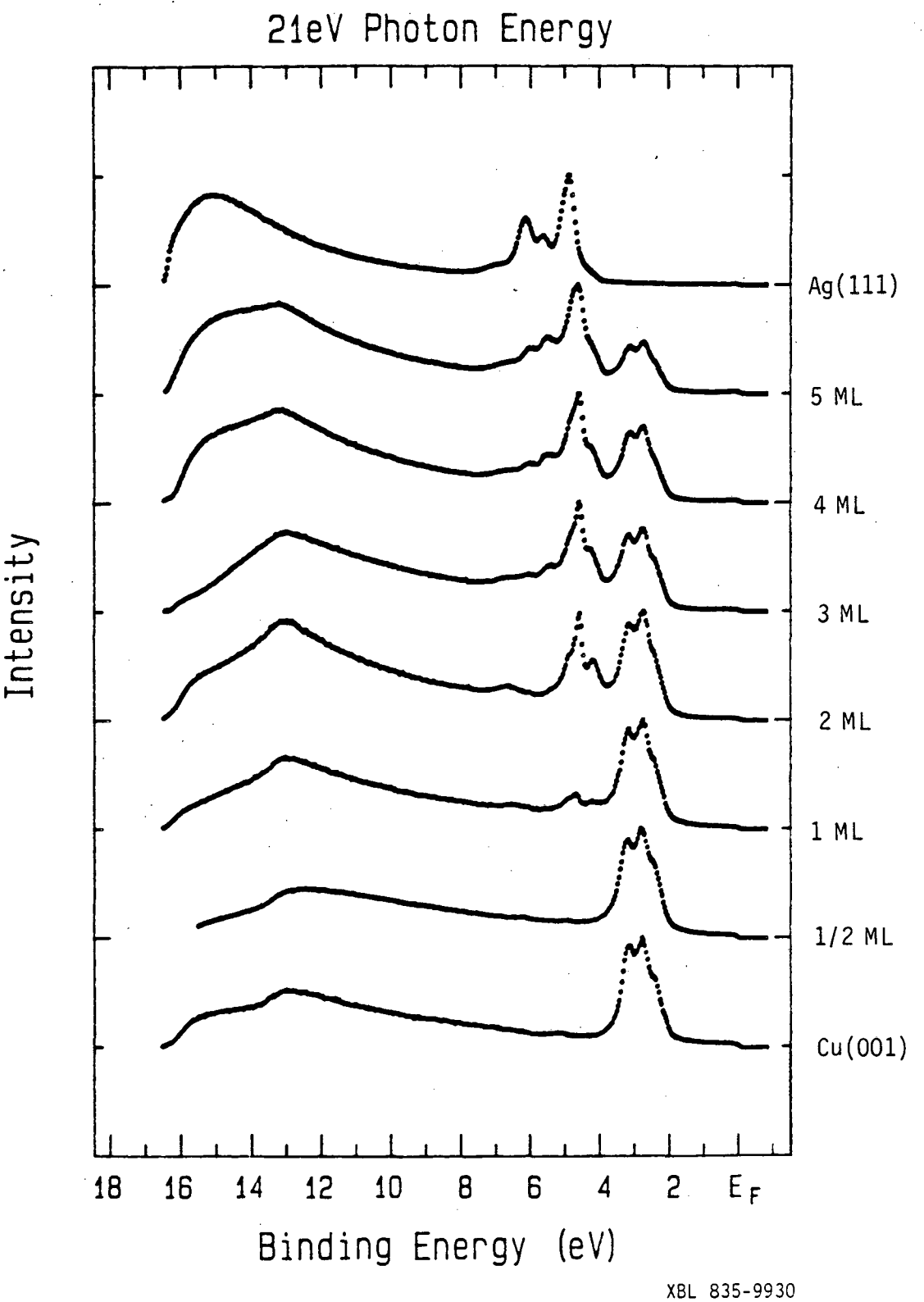
21eV Photon Energy
Intensity
Ag(111)
5 ML
4 ML
3 ML
2 ML
1 ML
1/2 ML
Cu(001)
18
16
14
12
10
8
6
4
2
E_F
Binding Energy (eV)
XBL 835-9930

Fig. 9

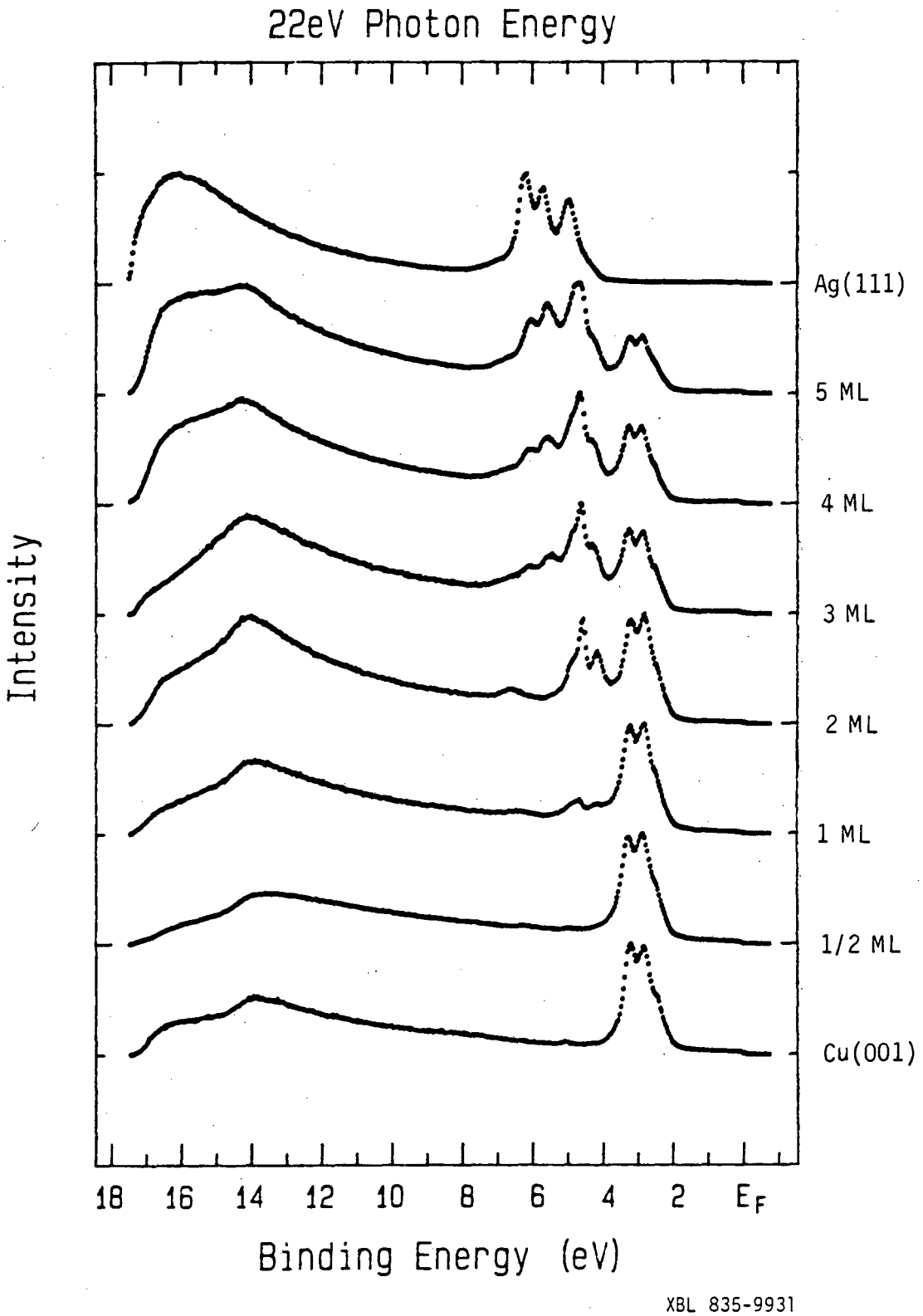
22eV Photon Energy
Intensity
Ag(111)
5 ML
4 ML
3 ML
2 ML
1 ML
1/2 ML
Cu(001)
18
16
14
12
10
8
6
4
2
E_F
Binding Energy (eV)
XBL 835-9931

Fig. 10

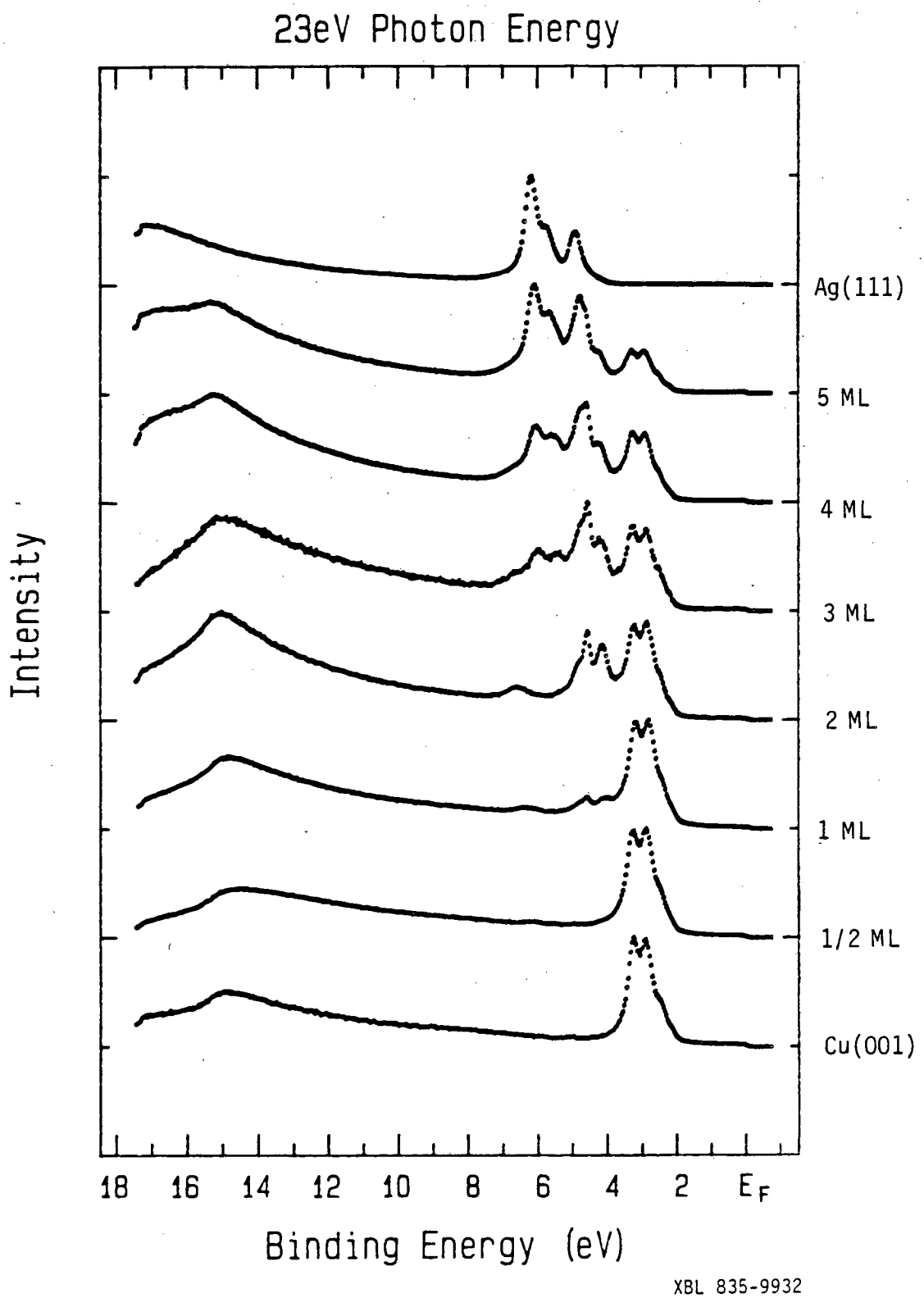
23eV Photon Energy
Intensity
Ag(111)
5 ML
4 ML
3 ML
2 ML
1 ML
1/2 ML
Cu(001)
18
16
14
12
10
8
6
4
2
E_F
Binding Energy (eV)
XBL 835-9932

Fig. 11

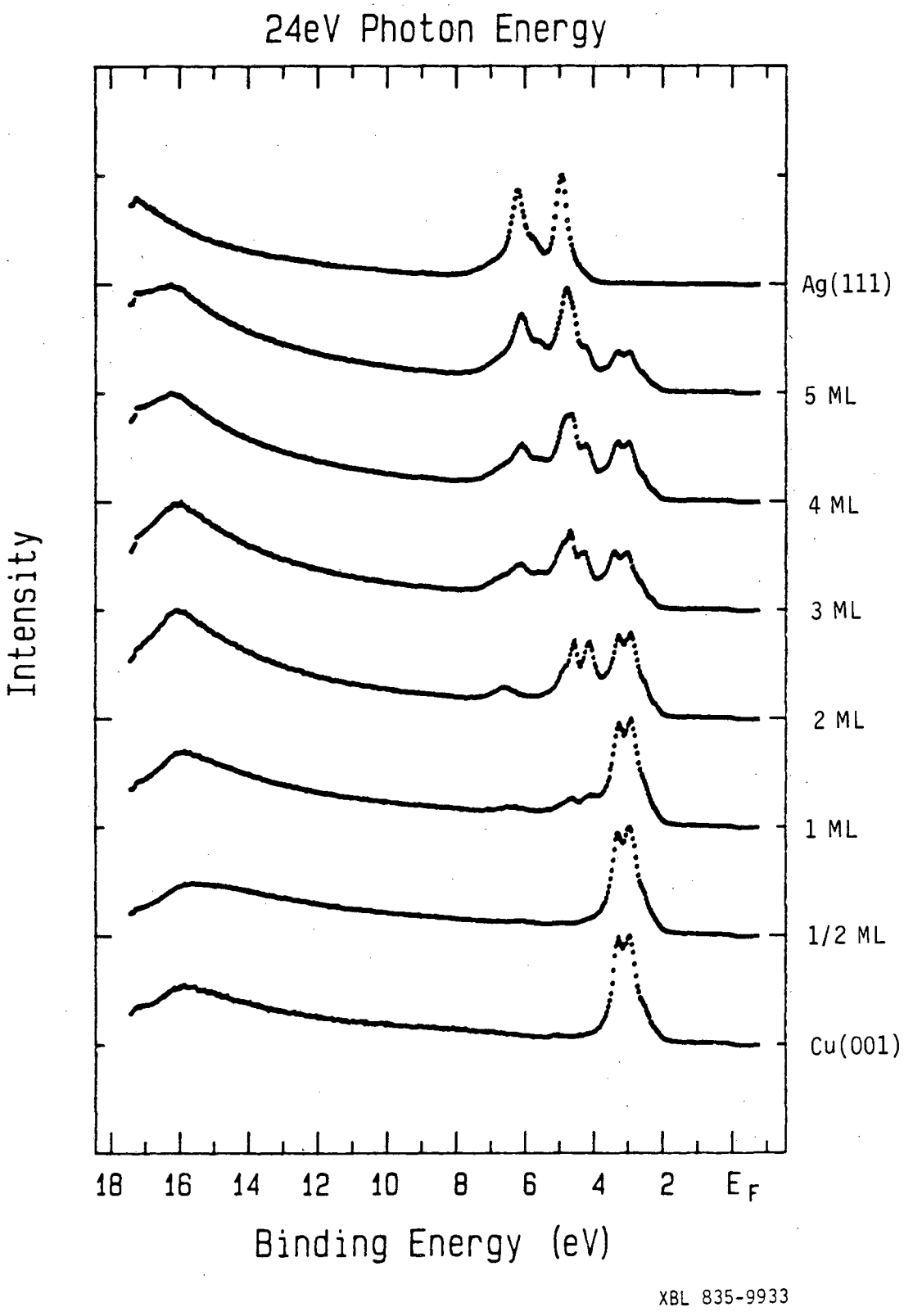
24eV Photon Energy
Intensity
Ag(111)
5 ML
4 ML
3 ML
2 ML
1 ML
1/2 ML
Cu(001)
18
16
14
12
10
8
6
4
2
E_F
Binding Energy (eV)
XBL 835-9933

Fig. 12

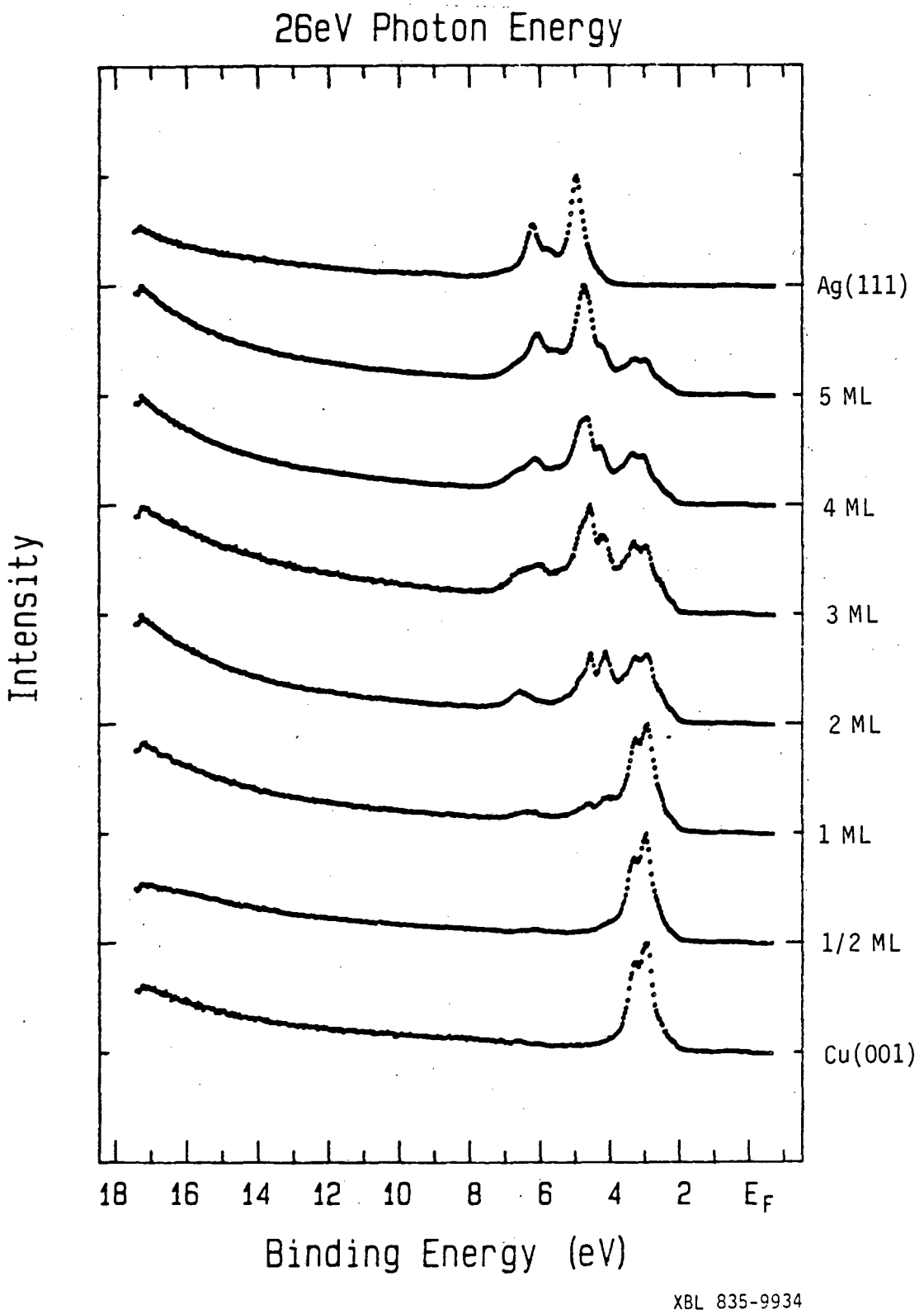
26eV Photon Energy
Intensity
Ag(111)
5 ML
4 ML
3 ML
2 ML
1 ML
1/2 ML
Cu(001)
18
16
14
12
10
8
6
4
2
E_F
Binding Energy (eV)
XBL 835-9934

Fig. 13

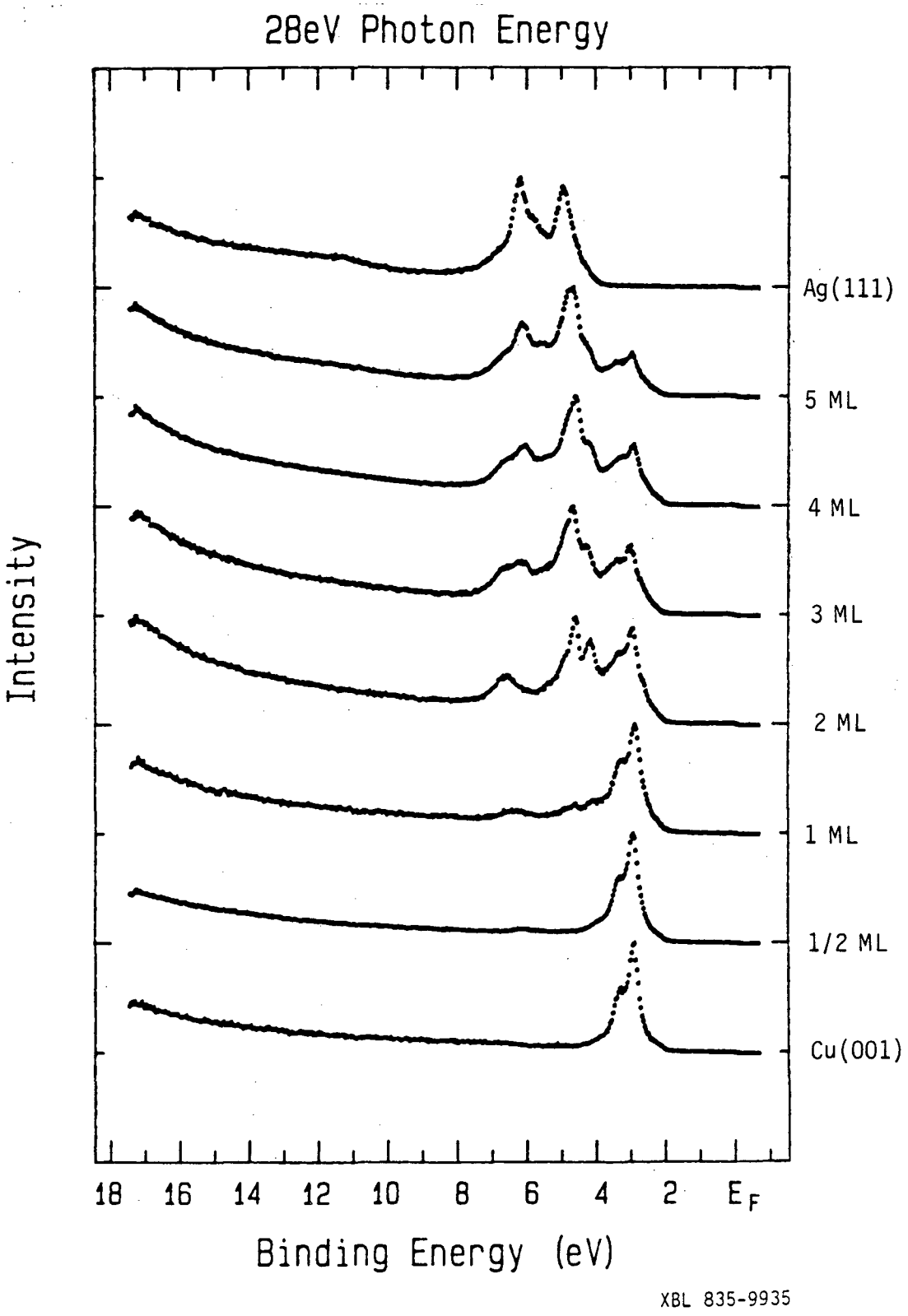
28eV Photon Energy
Intensity
Ag(111)
5 ML
4 ML
3 ML
2 ML
1 ML
1/2 ML
Cu(001)
18
16
14
12
10
8
6
4
2
E_F
Binding Energy (eV)
XBL 835-9935

Fig. 14

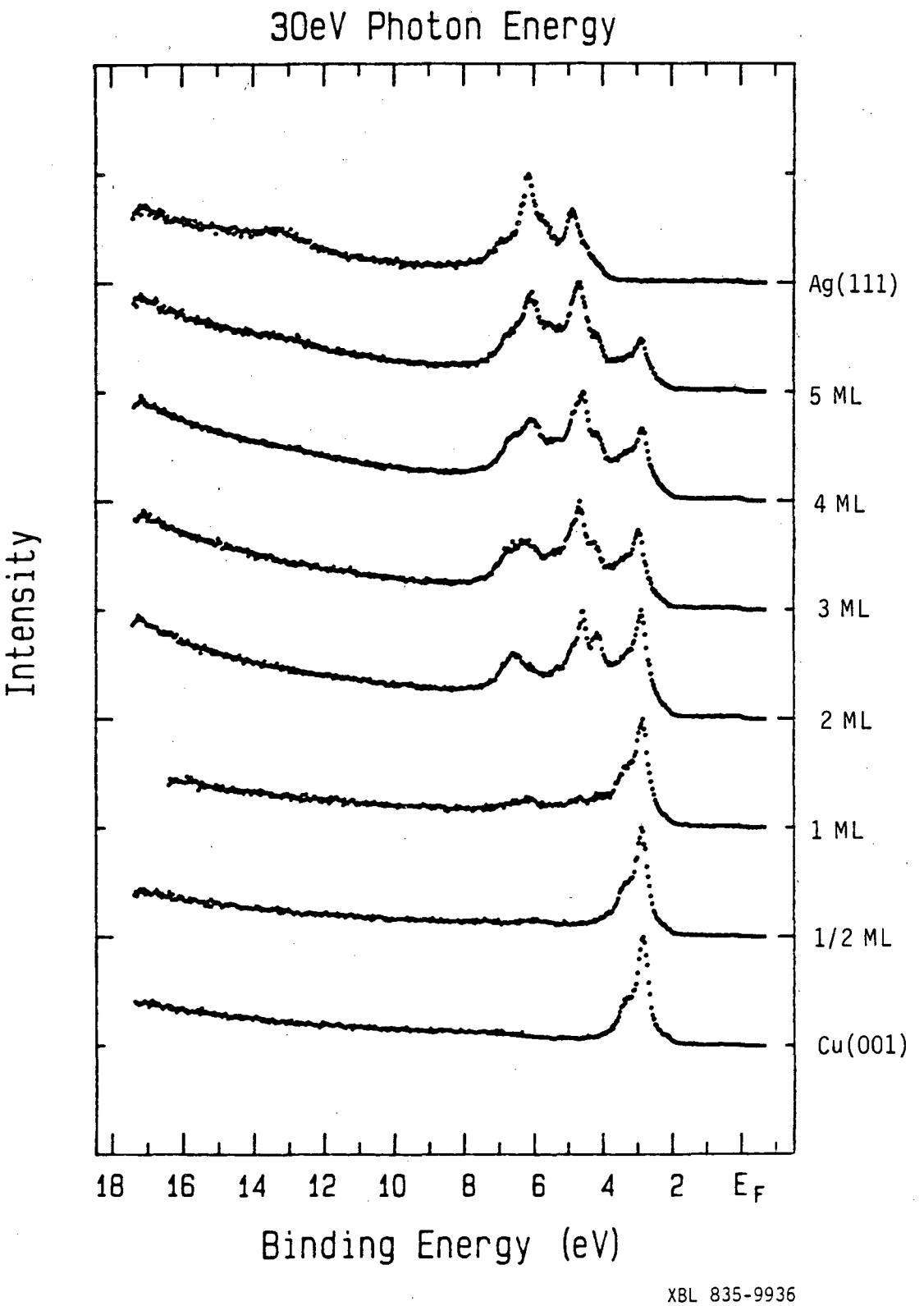
30eV Photon Energy
Intensity
Ag(111)
5 ML
4 ML
3 ML
2 ML
1 ML
1/2 ML
Cu(001)
18
16
14
12
10
8
6
4
2
E_F
Binding Energy (eV)
XBL 835-9936

Fig. 15

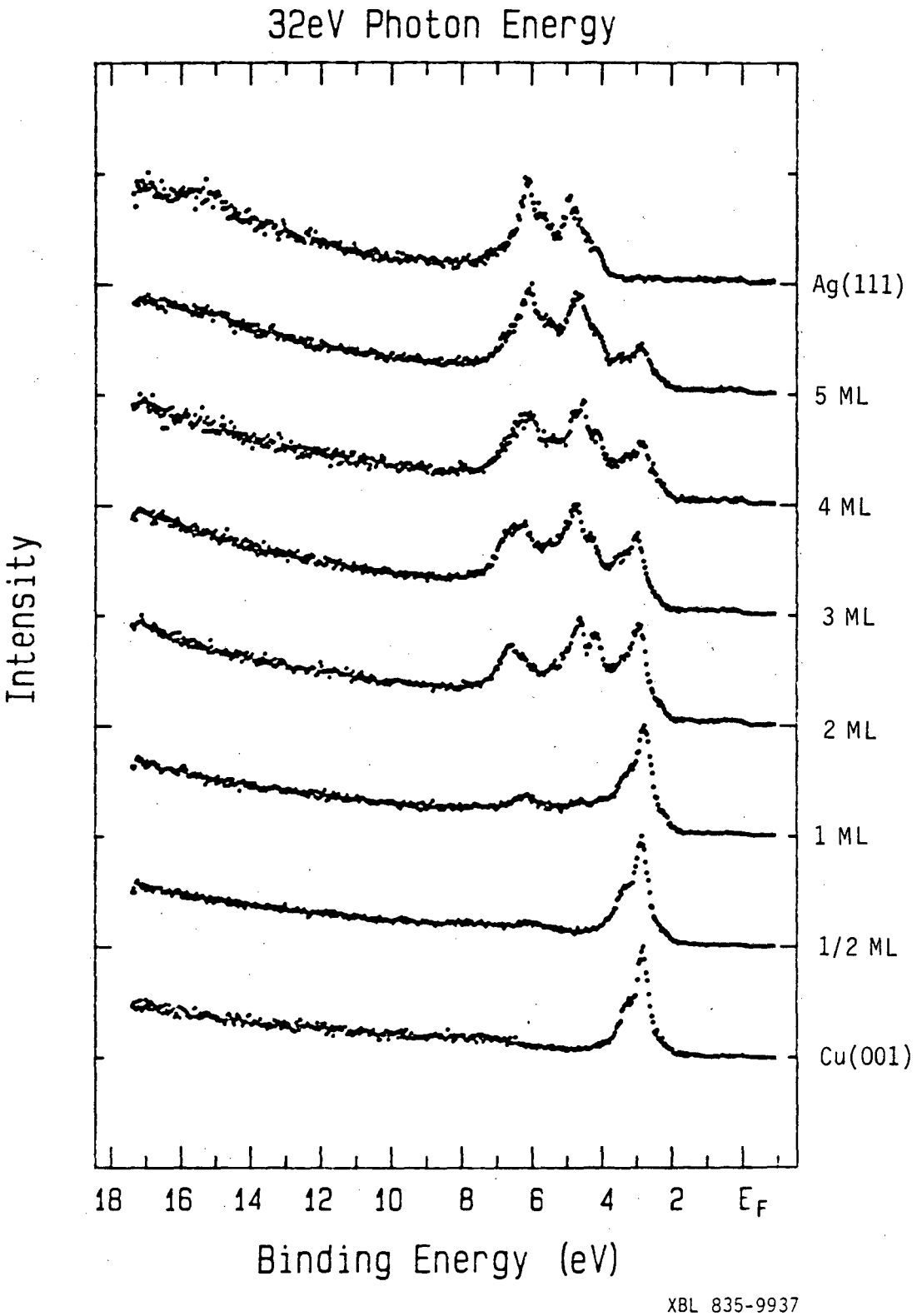
32eV Photon Energy
Intensity
Ag(111)
5 ML
4 ML
3 ML
2 ML
1 ML
1/2 ML
Cu(001)
18
16
14
12
10
8
6
4
2
E_F
Binding Energy (eV)
XBL 835-9937

Fig. 16

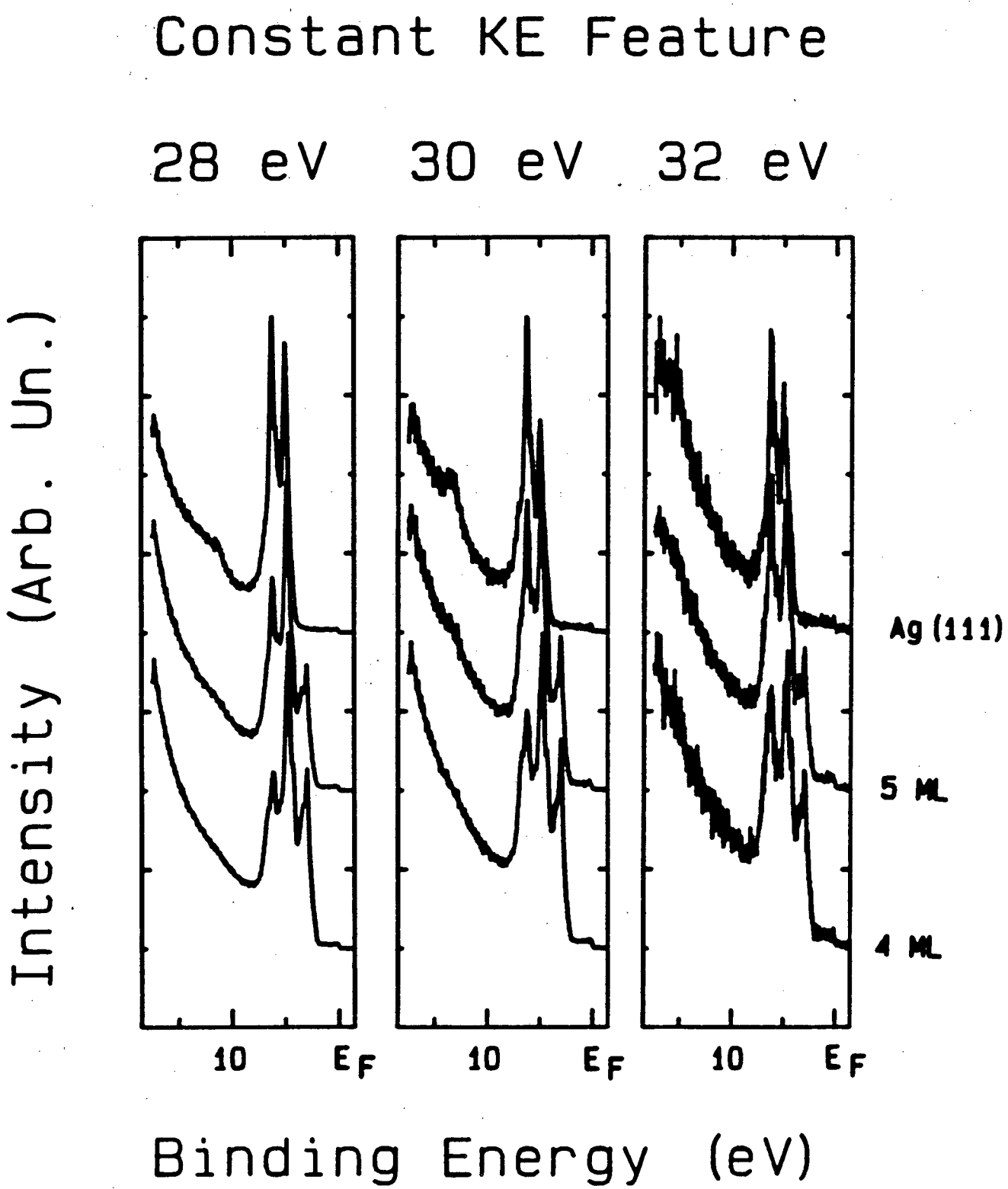
Constant KE Feature
28 eV
30 eV
32 eV
Intensity (Arb. Un.)
Ag (111)
5 ML
4 ML
10
E_F
10
E_F
10
E_F
Binding Energy (eV)

Fig. 17

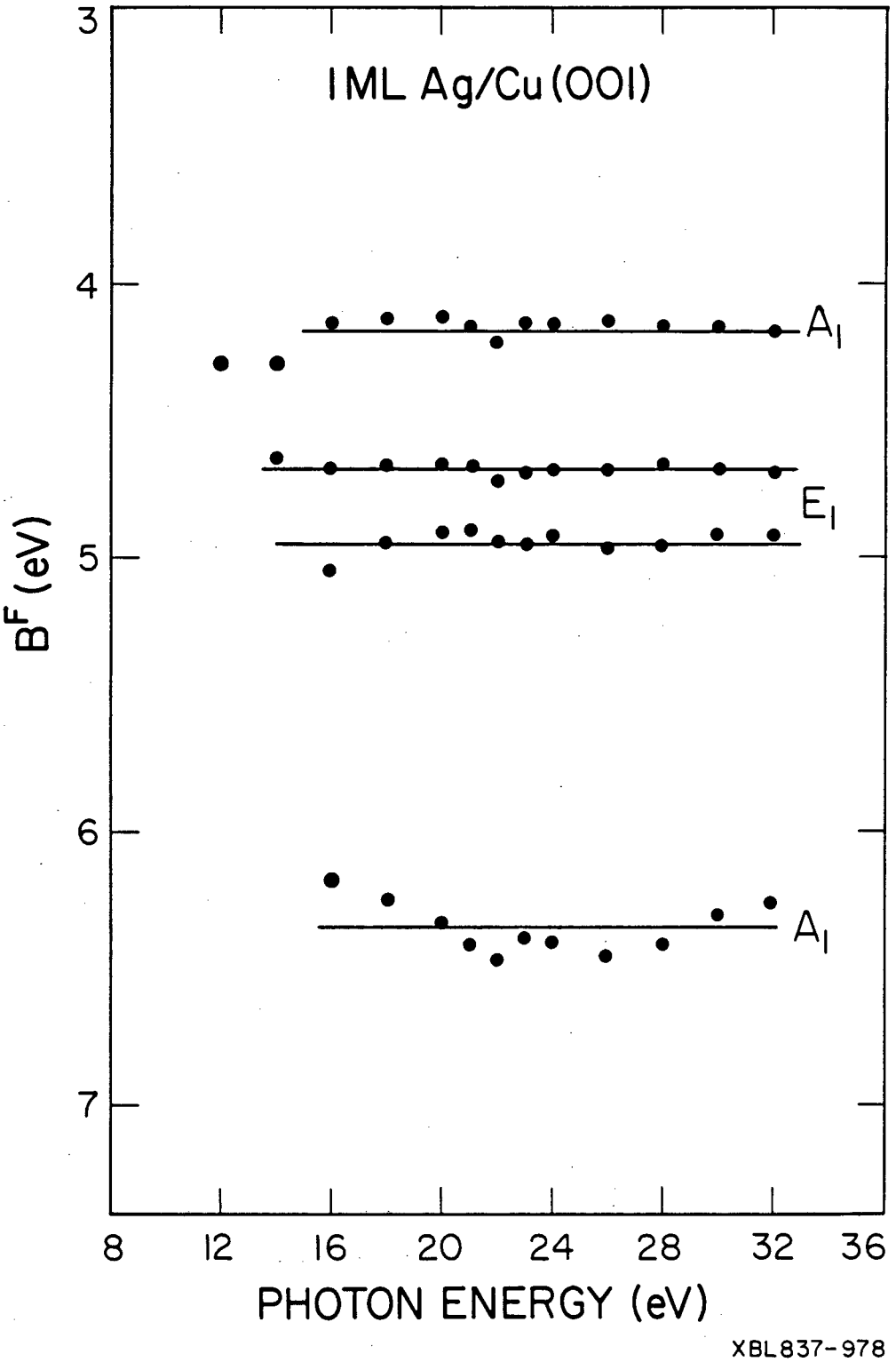
1ML Ag/Cu(001)
A_1
E_1
A_1
B^F (eV)
3
4
5
6
7
8
12
16
20
24
28
32
36
PHOTON ENERGY (eV)
XBL837-978

Fig. 18

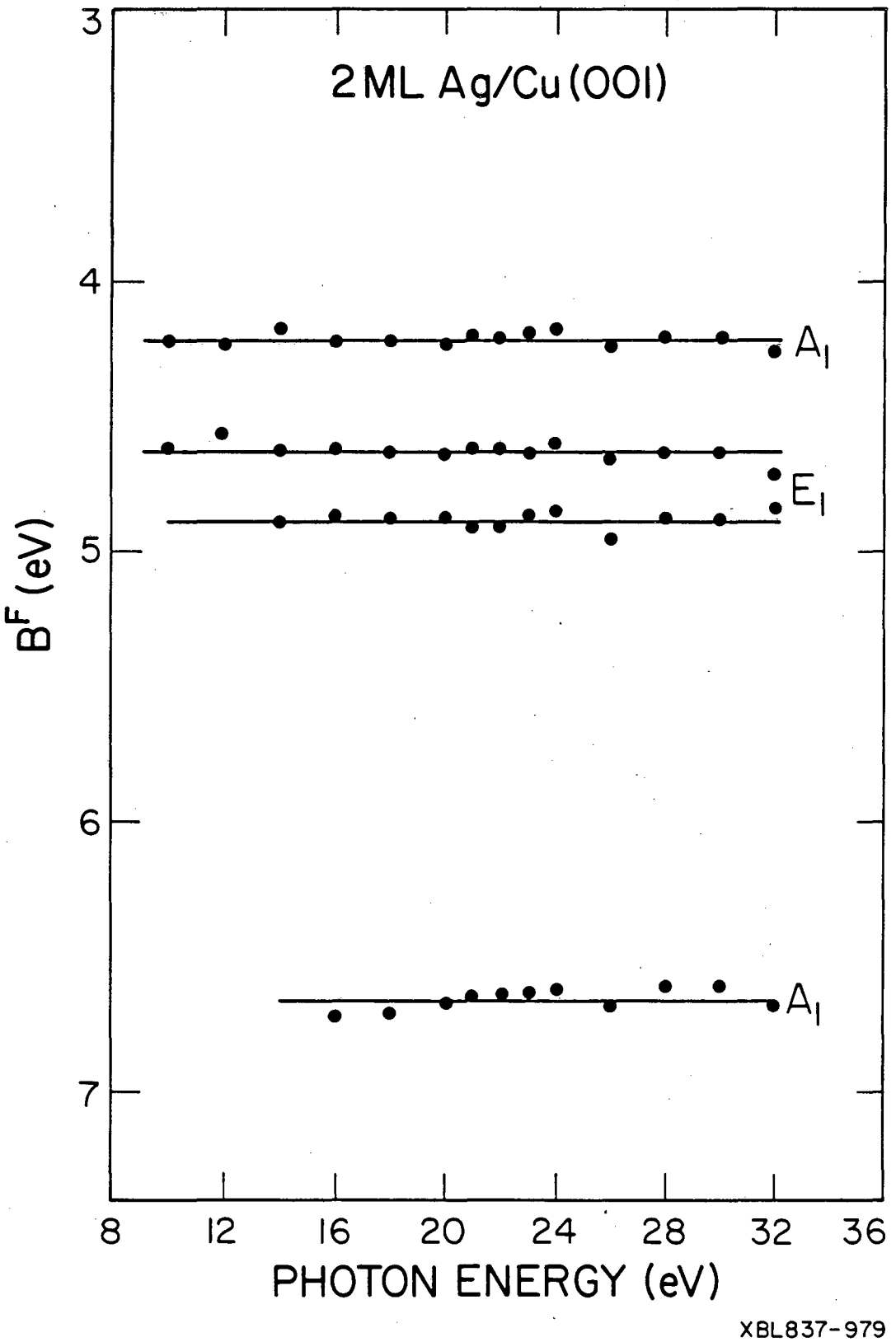
2ML Ag/Cu(001)
B^F (eV)
3
4
5
6
7
A_1
E_1
A_1
8
12
16
20
24
28
32
36
PHOTON ENERGY (eV)
XBL837-979

Fig. 19

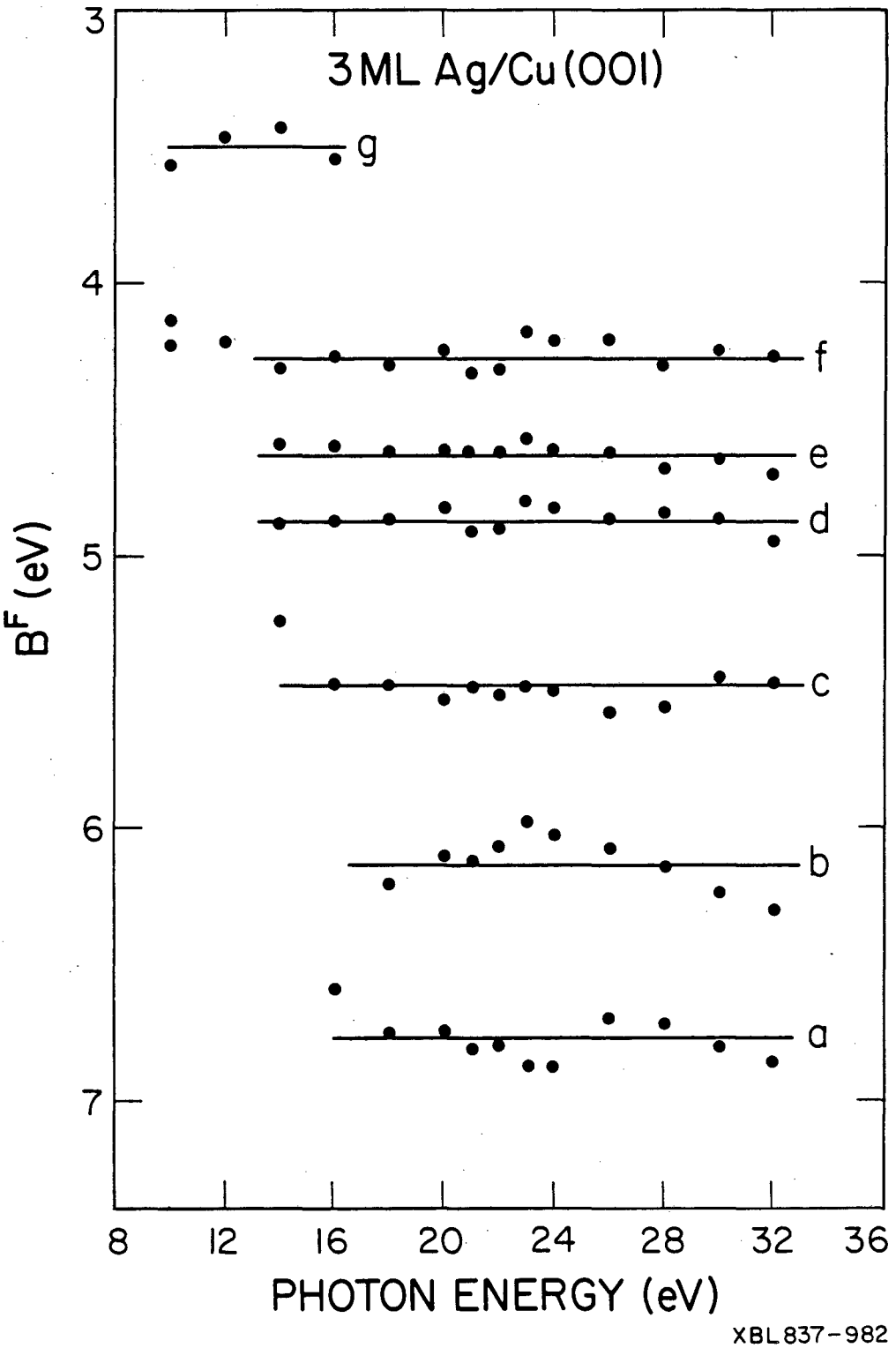
3ML Ag/Cu(001)
g
f
e
d
c
b
a
3
4
5
6
7
B^F (eV)
8
12
16
20
24
28
32
36
PHOTON ENERGY (eV)
XBL837-982

Fig. 20

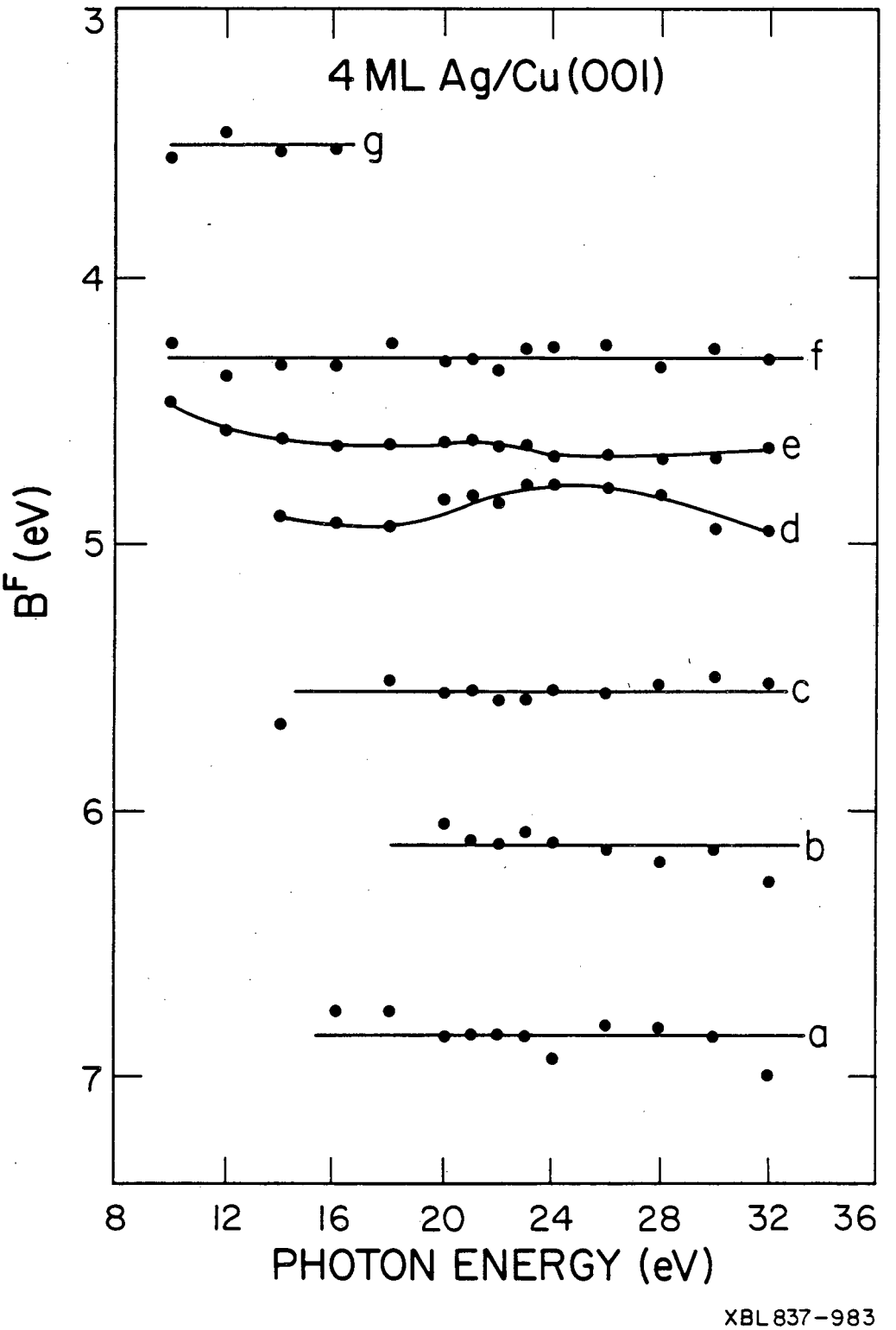
4 ML Ag/Cu(001)
g
f
e
d
c
b
a
3
4
5
6
7
B^F (eV)
8
12
16
20
24
28
32
36
PHOTON ENERGY (eV)
XBL837-983

Fig. 21

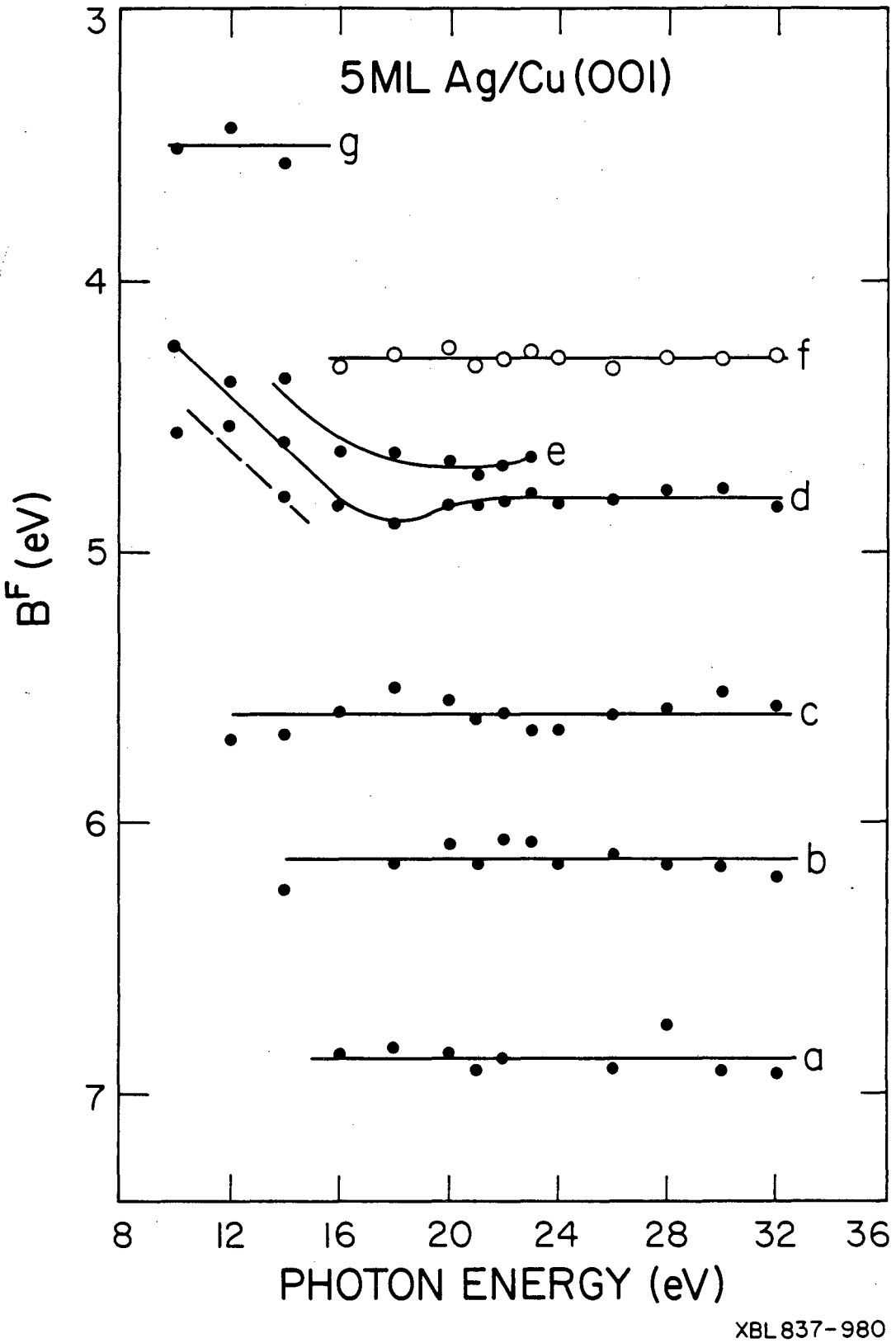
5ML Ag/Cu(001)
g
f
e
d
c
b
a
B^F (eV)
3
4
5
6
7
8
12
16
20
24
28
32
36
PHOTON ENERGY (eV)
XBL837-980

Fig. 22

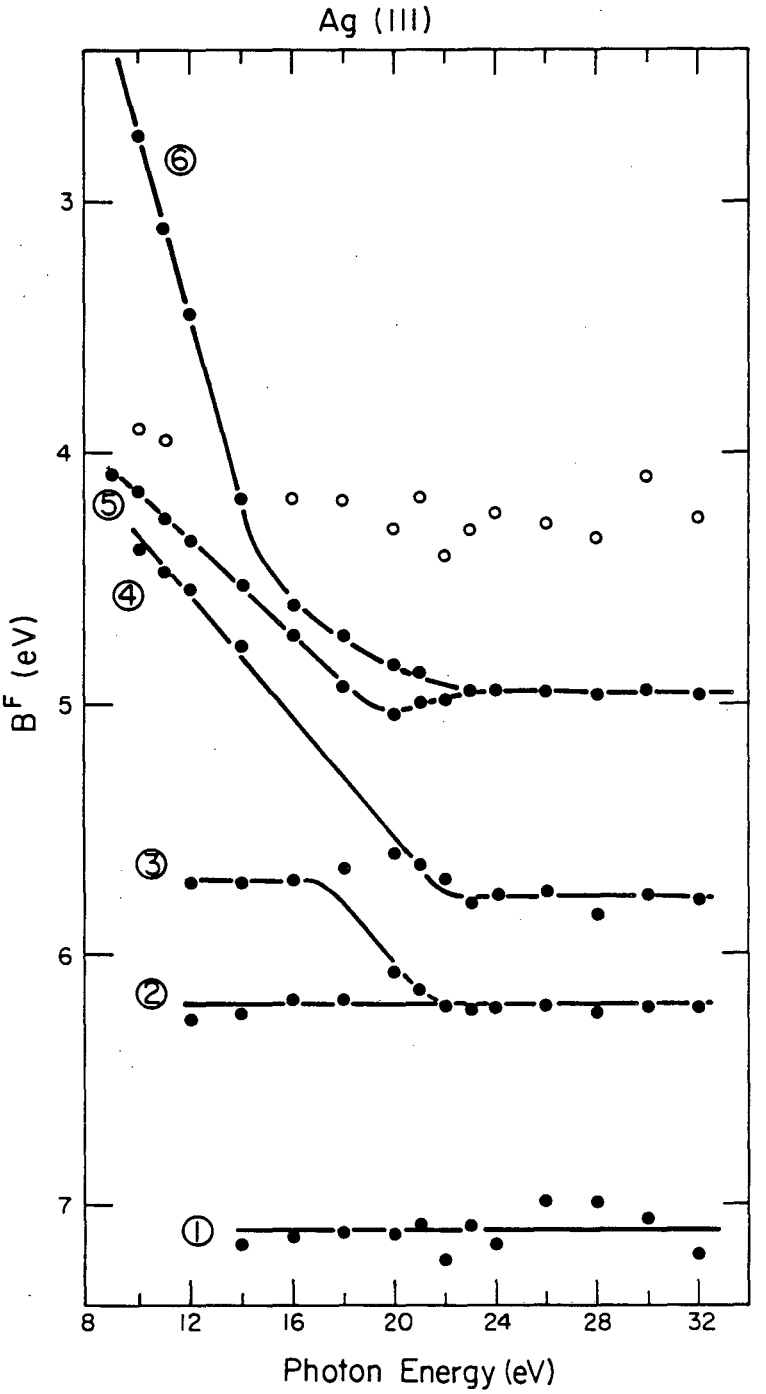

XBL 837-976

Fig. 23

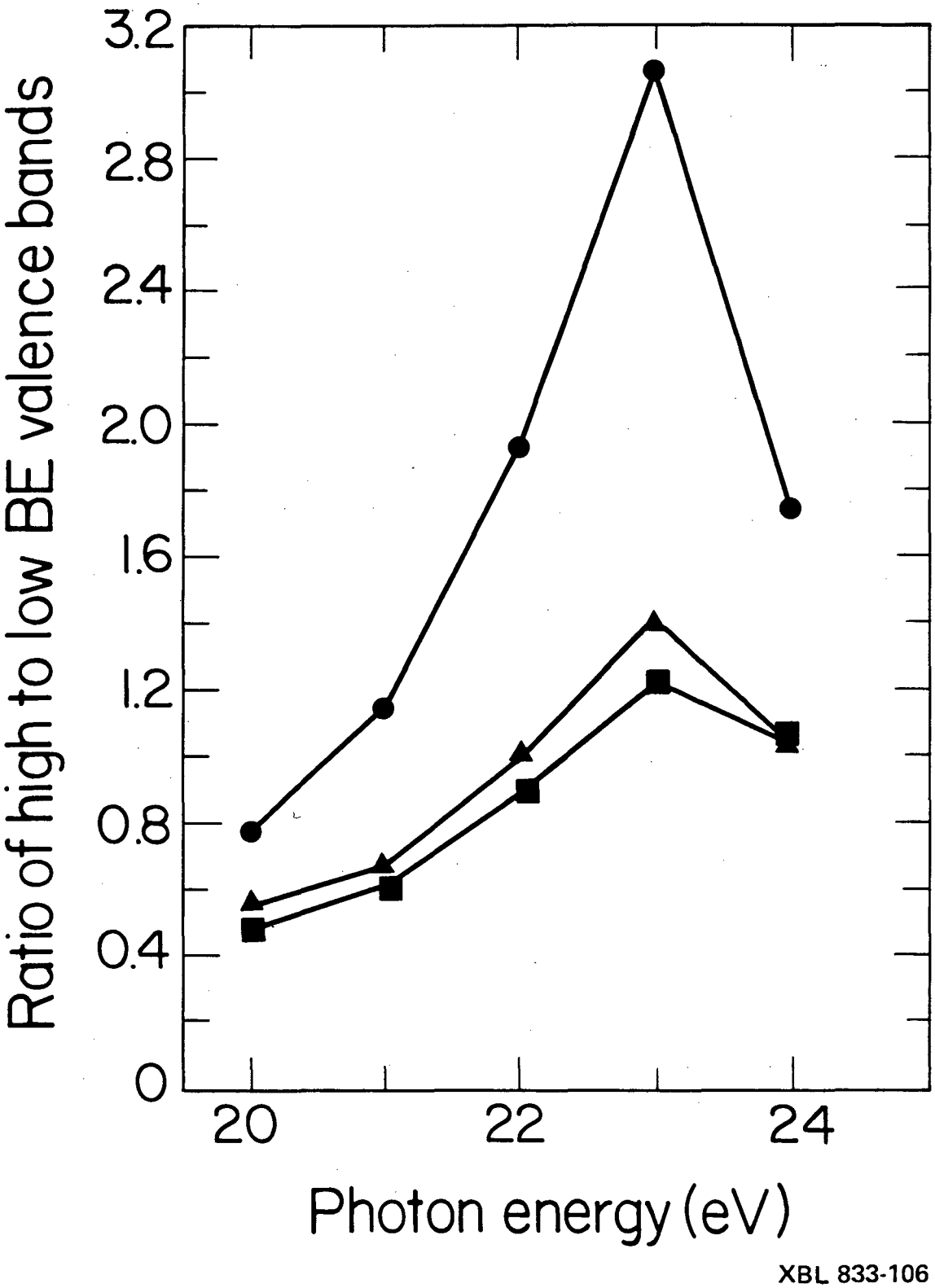
Ratio of high to low BE valence bands
3.2
2.8
2.4
2.0
1.6
1.2
0.8
0.4
0
20
22
24
Photon energy (eV)
XBL 833-106

Fig. 24

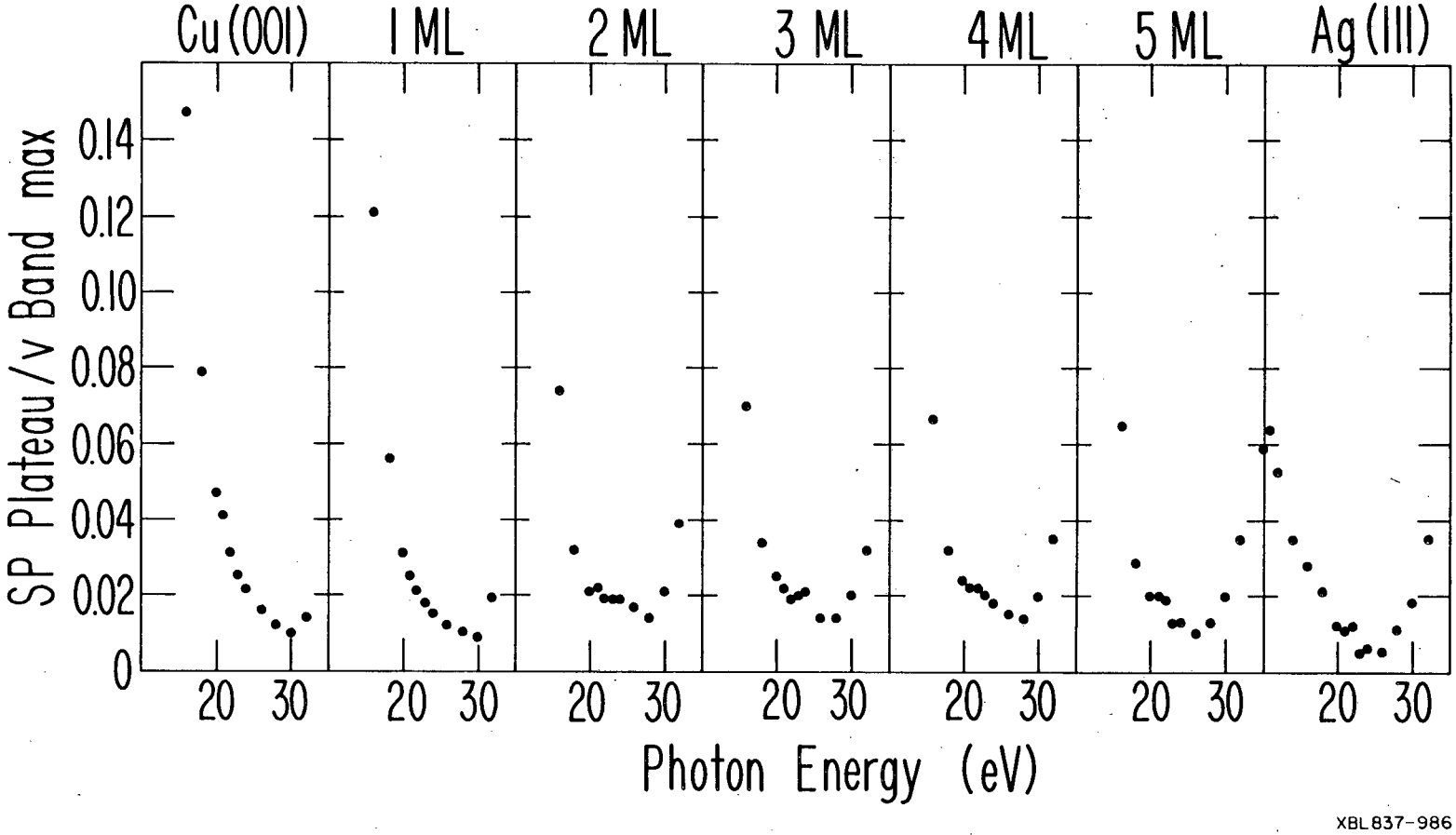
Cu(001)
1 ML
2 ML
3 ML
4 ML
5 ML
Ag(111)
SP Plateau/v Band max
0.14
0.12
0.10
0.08
0.06
0.04
0.02
0
20
30
Photon Energy (eV)
XBL837-986

Fig. 25

IV. HIGH RESOLUTION ANGLE-RESOLVED PHOTOEMISSION STUDY OF THE VALENCE-BAND STRUCTURE OF Ag(111)

A. INTRODUCTION

The electronic structure of three-dimensional bulk single-crystals continues to be of great interest in condensed phase material science. Advances in photon sources and spectrometers have allowed increasingly improved resolution to be achieved in angle-resolved photoemission (ARP), which is the technique of choice to investigate the electronic band structure of solids. Assuming a reasonable understanding of the final state, ARP can be used as a direct probe of the dispersion relations of the valence bands, i.e. the dependences of the binding energies upon the crystal momenta. In the case of Ag(111) and the photon energy range of the experiment reported here, there is a particularly simple final state for normal emission.[1,2] Here results are presented which are an extension of a previous experiment (Ref. 2). Included are higher resolution data collected at normal emission along the Γ to L line in the 3-dimensional Brillouin Zone ($h\nu$= 6-32 eV) and off-normal data collected at $h\nu$ = 14 and 21 eV.

The total resolution of the experiment was typically better than 100 mV and the angular resolution $\pm 3^{\circ}$ or better. This improved resolution contributed to the observation of previously experimentally undetected but theoretically predicted peaks: general agreement was found between the calculated valence bands of Reference 1 and the experimental data. Also because of the improved resolution, the

Ag(111) surface state was seen to persist to photon energies of 22eV.

The remainder of the chapter is organized as follows: Section B contains the experimental details; Section C has the experimental photoemission results; Section D is a discussion of these results and a comparison with theory; and Section E has the summary and final conclusions.

B. EXPERIMENTAL

The experiment was performed at the Stanford Synchrotron Radiation Laboratory during dedicated running time on Beam Line 1-2, which has an effective photon energy range of 6-32 eV. The chamber is an ultra-high vacuum, angle-resolved photoemission spectrometer which is discussed in detail elsewhere.[3] During the experiment, analyzer resolution was set at 60 meV and the analyzer had a half-angle acceptance of $\pm 3^{\circ}$. The total resolution was less than or equal to 100 meV for 6 eV $\leq h\nu \leq$ 24 eV, 110 meV for $h\nu$ = 26 eV, 170 meV for $h\nu$ = 28 eV, 190 meV for $h\nu$ = 30 eV, and 210 meV for $h\nu$ = 32 eV. These are the full-width-at-half-maximum values (FWHM) obtained assuming that the analyzer and monochromator contributions add in quadrature. At beam currents of near 35 mA and with $h\nu$ = 21 eV, these spectra typically took 20 minutes to collect, with maximum accumulated counts equal to 16000 for a .039 eV wide channel.

The sample was cleaned by continuous Ar ion sputtering during cycles of heating (15 m) and cooling (30 m). The pressure was 10^{-5} torr, backfilled with Ar, and the maximum temperature during sputtering was above 500°C. After sputtering, the sample was

annealled to 400°C for five minutes to ensure a well-ordered surface, as confirmed by Low Energy Electron Diffraction (LEED) observations. Surface cleanliness was checked using LEED-optics Auger Electron Spectroscopy (AES). Sulfur levels were below detection and the possible carbon line was obscured by a silver Auger peak near 260 eV kinetic energy. The O(510 eV)/Ag(355 eV) Auger derivative ratio was less than 0.005. Moreover, the presence and sharpness of the Ag(111) photoemission surface state confirmed the ordering and cleanliness of the surface. The base pressure was 8×10^{-10} torr.

For the photoemission experiment, the crystal was aligned via in-situ laser autocollimation, the in-situ LEED and prior X-ray diffraction. The [111] normal direction and the [010] off-normal bulk vector were both in the horizontal plane containing the polarization and Poynting vector of the light, as shown in Figure 1. The [010] direction was between the polarization and Poynting vector. For the normal emission experiment, the angle of incidence of the light was 60° with respect to the surface normal ($\theta_{h\nu}$). In the off-normal experiment, the rotations of the analyzer and sample were all in the horizontal plane, as shown in Figure 1. The angle of incidence of the light was 60° for $\theta_e \leq 30°$ and $\theta_{h\nu} = 50°$ for $\theta_e = 40°$.

C. PHOTOEMISSION RESULTS

The normal emission spectra taken with $h\nu$ = 6-32 eV are shown in Figures 2, 3, and 4. One of the important features of Figure 2 ($h\nu$= 23-32 eV) is the constant kinetic energy peak at KE = 17 eV (with respect to the Fermi level). It can be seen moving across the spectra

of $h\nu \geq 26$ eV, at $B^F = h\nu - 17$eV. The remaining structure in Figure 2, save for the leading shoulder near $B^F = 4.2$ eV, can be attributed to direct transitions from the initial state Bands 1-6. The low B^F shoulder in these and the following spectra has been assigned in Chapters 2 and 3 to the $3z^2-r^2$ state of the topmost Ag layer. The improved resolution allows for easy identification of the weaker features in Figure 2. The variations of the spectral intensities will be discussed in the next section.

In Figure 3 ($h\nu$ = 14-22 eV), the features at 4.5 eV $\leq B^F \leq$ 7 eV are again associated with Bands 1-6 and the leading shoulder is again present near $B^F = 4.2$ eV, for $h\nu \geq 16$eV. Band 6 is starting its rise toward E_F in the $h\nu = 14$eV spectrum: it envelops the $3z^2-r^2$ state near $B^F = 4.2$eV. The surface state near the Fermi edge is also apparent, particularly at the lower photon energies. There is possibly a very weak feature at $B^F = 9$ eV at $h\nu = 20$ and 21 eV, which could be due to extremely slight CO/CO_2 contamination.

Figure 4 contains the spectra taken at $h\nu$ = 6-12 eV. The surface state at the Fermi edge is very strong here and the dispersion of the bulk bands is obvious from the movement of the low B^F feature from $B^F = 3.5$eV at $h\nu = 12$eV to $B^F = 1.5$ eV at $h\nu = 7$ eV. It becomes increasing difficult to properly assign the structures as they drift into the low kinetic energy tail, particularly since the low KE cutoff function of this analyzer starts near KE = 2 eV. The worst example is the is weak structure at $B^F = 5$ eV in the $h\nu = 11$ eV spectrum which is conceivably a photoemission peak but is completely inconsistent

with the analysis done in the next section.

In Figures 5 and 6, the off-normal spectra taken with $h\nu$ = 21 eV and 14 eV, respectively, are shown. All of the off-normal rotations were between the [111] normal vector and the [010] bulk direction at 54.7° off-normal. The spectra shown in Figure 5 and 6 demonstrate the breakdown of degeneracy and broadening of the band width associated with moving away from the high symmetry lamba (Γ-L) direction. The attenuation of the low kinetic energy tail at higher θ_e may be due to the deflection of the electrons from the charging of sample plate insulators which becomes noticeable at grazing take-off angles and the lowest kinetic energies. Note the abundance of easily observable sharp features in both figures and the rapid dispersing of the low binding energy peak toward the Fermi edge at nonzero angles, especially at $h\nu$ = 14 eV.

D. DISCUSSION

Valence Band Dispersion

The experimentally determined parameters are B^F and the external exit angle. If a knowledge of the final state exists, it is possible to work within the Direct Transition Model[2] and determine the crystal momenta of the final and initial states.

In the case of Ag(111),[1,2] the final state for normal emission is well understood. Fitting a parabola centered at k = 0 to the calculated final state of Reference 1 and assuming primary cone emission, the results shown in Figure 7 were obtained. The gap at Γ in the final state has been neglected. Also shown in Figure 7 are the

calculated initial states along the Γ to L line from Ref. 1. Band 1 is unshifted, Bands 2 and 3 are rigidly shifted downward 0.3 eV, and Bands 4, 5 and 6 are rigidly shifted downward 0.2 eV. As is evident in Figure 7, the agreement between calculation and experiment is quite good, except for Band 1. The disagreement seen at Band 1 may very well explain the necessity of shifting the Bands 2-6 downward: clearly, the bottom of the valence bands is not well-defined. In fact, in Ref. 1 the bottom of the valence bands is placed at 1.46 eV below the muffin tin zero, which is an inconsistency.

In traversing the interface between the crystal and free space, the momentum of the photoelectron parallel to the surface is conserved. Assuming primary cone emission and no umklapping parallel to the surface,

$$\underline{k}_{(x,y)} = \underline{q}_{(x,y)} = \underline{q} \sin(\theta_e) \qquad (1)$$

where $\underline{k}_{(x,y)}$ is the crystal momentum parallel to the surface, $\underline{q}_{(x,y)}$ is the external momentum parallel to the surface, $\underline{q}$ is the total external momentum and θ_e is the external emission angle relative to the surface normal. Only a knowledge of the work function of the surface of interest is necessary to determine the parallel momentum from B^F and the external exit angle:

$$KE = \hbar^2 q^2/2m = h\nu - B^F - \phi. \qquad (2)$$

Using the value of ϕ = 4.74 eV[4], the results of the off-normal experiment are plotted in Figure 8. The bands shown are merely smooth curves drawn through the points and based upon the assignments at $k_{(x,y)}$= 0, i.e. normal emission, and the premise that no band crossing will occur. Band crossing is forbidden because they are all of the two degenerate double-group representations (spin up and spin down) in the low symmetry (C_s) region off of the high symmetry direction.

INTERPOLATION

In order to check our experimentally determined results, the interpolation scheme of Hodges et al.[5] was used to calculate the bands along Γ to L and in the off-normal study. Using the parameters of N. V. Smith[6] and a program previously implemented in this group,[7] the following results were obtained.

Figure 9 shows a comparison of the the normal emission experimental results with the interpolation scheme values along Γ to L. Here the agreement between the interpolation program and the experimentally determined values is moderately good. Band 1 is again in disagreement but otherwise there is reasonable concurrence. This serves primarily as a confirmation of the possible utility of the interpolation scheme.

In the normal emission experiment the final state is well defined, but in the off-normal experiment determination of the crystal momentum is more difficult. Figure 10 shows the approximate paths taken through the Brillouin Zones in the off-normal study. The crystal

momentum parallel to the surface is determinable from Equations 1 and 2 above, but to calculate k_z, the crystal momentum perpendicular to the surface, the final state and inner potential must be known. A free-electron-like final state was used in the off-normal crystal momenta calculations, with a correction for the refraction at the surface. The free-electron-like final state dispersion relation was obtained by fitting a parabola centered at k = 0 to the calculated final state in the [111] direction, Band 7 of Ref. 1. This can be summarized in the following form:

$$k_z = [(2m^*/\hbar^2)(h\nu - B^F + E_F - \Delta E) - k^2_{(x,y)}]^{1/2}, \qquad (3)$$

where E_F is the Fermi energy and is taken as 7.49eV (Ref. 1). The effective mass is m^*, with $m^*/m = 1.092$, and $\Delta E = 4.520$eV is the energy offset of the parabola from the bottom of the bands. To determine the initial state, the final state was then umklapped back into the first zone by using $\underline{G} = \underline{G}(111)$, with the exception that for $h\nu = 21$eV and $\theta_e = 40^\circ$, Band 6 required $\underline{G} = \underline{G}(020)$. The crystal momenta thus determined were used as input for the interpolation program, the output of which was then compared with the experimental results.

To attempt to overcome the inherent limitations of this free-electron-like final state approximation, eigenvalues were calculated with the interpolation scheme for a range of values of k_z associated with different possible values of B^F. For while the

essential experimental parameters are B^F and θ_e, varying B^F has the effect of changing E_F and ΔE, both of which were taken from [111] direction calculations. For consistency, this change in B^F was also implemented into the calculation of $k_{(x,y)}$, but it has only a small effect on $k_{(x,y)}$, as can be seen in Figures 11 and 12. Three integer binding energies were chosen around each experimental band or point, with $B^F \geq 0$. Thus a cluster of points in a range of k-space associated with a given angle were determined which were then used as input for the interpolation scheme. An implicit assumption here is that the reduced mass is correct. Since m^*/m is so close to unity this seemed reasonable. Moreover, a limited attempt using a true free-electron final state was made, with the rest mass of an electron and an energy offset of zero being used. The results of the interpolation program using these momenta were qualitatively the same as for the final state from Ref. 1, but of slightly poorer agreement with experiment.

Figure 11 compares the experimental and interpolation results for the off-normal study at $h\nu$ = 21eV. It is obvious that the agreement is semi-quantitative at best. The worst disagreement occurs for Bands 4 and 5, away from the [111] direction. This is not surprising, since the interpolation scheme treats the d-orbitals in a tight-binding approximation and the use of a [111] final state would be increasingly dubious at the larger angles. The limitations of the tight-binding approximation would be most significant at the Brillouin Zone boundaries and at lower binding energies. Band 6 is reasonably

approximated by the plane-wave-state as it rises toward the Fermi energy, but Bands 4 and 5 will be composed of mainly d-orbitals. The repulsion observed experimentally between Bands 4 and 5, and also Bands 2 and 3, is not properly mimicked by the interpolation bands.

In Figure 10, it can be seen that at $h\nu = 21eV$, an L point is being approached at $\theta_e = 40^\circ$. As a test of consistency, the interpolation values at L and the experimental points closest to L from the normal-emission study are compared with these off-normal results in Figure 11. The interpolation off-normal bands are converging very smoothly upon the values from L, while the experimental values agree reasonably well but are not undergoing such a convergence. This suggests several observations: (1) The limited splitting near L can be attributed to spin-orbit splitting in the interpolation program. In fact, if the spin-orbit parameter is set to zero, Bands 4 and 5 are degenerate and Bands 2 and 3 are degenerate across the second half of the Γ to L direction, after the hybridization caused by the crossing of the plane-wave state. This supports the assertion of insufficient d-d interaction near the zone boundary in the interpolation program. (2) The interpolation scheme is insensitive to the small changes in k and tends to vary too smoothly. This is supported by the small effect of varying B^F within the free-electron-like final state model and the similarity of the results of that final state model and those of the true free-electron final state model. (3) The inaccuracies observed at normal emission are amplified off-normal. Bands 2 and 3 of the interpolation program rise

incorrectly in the high-symmetry lambda (Γ to L) direction and also in the off-normal data. (4) These final state models are incorrect and $\theta_e = 40^\circ$ is not near L. This seems unlikely because the small disagreement between the normal-emission and off-normal-emission bands can be attributed to their being only near but not at L.

Figure 12 shows the $h\nu = 14$eV off-normal study. Again the agreement is only semi-quantitative. In this case Band 5 shows the best agreement of the d-bands. Considering that the deviation of the fitting is on the order of the 0.1eV,[5] the observed quality of the match is understandable.

CROSS SECTION AND FINAL STATE EFFECTS

The flat region of near Γ of Band 7 of Ref. 1 gives rise to two interesting phenomena. First, while a parabolic fit crossing the band gap provides an accurate means of analyzing the dispersion relations at $h\nu > 24$eV, the intensity variations at $h\nu = 20$-26eV are best described in terms of a resonance into this flat region of Band 7. As the photon energy increases from 20 to 24eV, it sequentially matches the energy separation between the flat initial states near Γ and Band 7 near Γ. This gives rise to a very noticeable modulation of the d-band peak intensities. The second effect is the constant kinetic energy feature discussed previously at $B^F = h\nu - 17$eV at $h\nu \geq 26$eV.

The above effects are attributed to the lower band bordering upon the bandgap at Γ. It is reasonable to expect that similar behavior should be observed for the upper boundary. There are two pieces of evidence to suggest just that.

The first is the appearance of the spectra (Fig. 2 and 3). There are striking similarities between the pairs $h\nu$ = 20 and 26, $h\nu$ = 22 and 28, $h\nu$ = 24 and 30 and $h\nu$ = 26 and 32eV. The degraded resolution at $h\nu \geq$ 26eV has the effect of smearing out some of the features but the resemblance is very strong. Secondly, in the $h\nu$ = 32eV spectrum a weak feature at B^F = 9eV is observed. This could be another constant kinetic energy feature at $B^F = h\nu - 23$eV. Both of these would correspond to a flat final state at 23eV above the Fermi energy. This provides an experimental determination of the band gap at Γ. The gap is 6eV wide with flattened boundaries at 17eV and 23eV above the Fermi energy. These results are consistent with an augmented-plane-wave calculation[8] which found a gap of 8eV with boundaries at 17eV and 25eV above the Fermi energy at Γ.

It should be noted that this resonance may be some type of residual atomic effect involving a d-f transition near Γ. Experimental atomic cross section measurements[9] are not sufficient to exclude this possibility but, as discussed in Chapter III, the effect is observed in a silver metal overlayer system only at higher exposures, not at all coverages.

SURFACE STATE

The Ag(111) normal emission surface state was observed over the photon energy range of 6 to 22 eV. Previously, it had been observed with synchrotron radiation at photon energies from 6 to 12 eV[2] and with higher resolution and using line sources up to $h\nu$ = 21.2 eV.[10,11] Table 1 and Figure 13 show a summary of the surface state

data from this experiment.

Column 2 of Table 1 contains the binding energies determined by visual inspection. Column 3 has the binding energies determined by fitting a gaussian step, a gaussian peak and a constant background to the Fermi edge region. The means of each pair were constrained to be the same value, as well as the widths of each pair. This causes the slight downward shift in B_2^F relative to B_1^F. Note that in both cases the peak moves to higher binding energy with increasing photon energy. The measured width (Column 4), from the gaussian fitting, shows the same behavior, and this is also seen in the lifetime estimates (Column 6) corrected for the total resolution (Column 5). In general, the values below $h\nu$ = 12 eV are smaller than those above 12 eV, as illustrated by Figure 13 and by the averages at the bottoms of the columns of Table 1. It should be noted that for $h\nu \leq$ 10eV a LiF window and smaller slits were used while for $h\nu \geq$ 11eV no window and larger slits were used. No discontinuities stand out between 10 and 11eV. However, the binding energy values for $h\nu$ = 21eV are inconsistent with those around it. Several $h\nu$ = 21eV spectra have the same appearance. It seems that the error is related to the determination of the Fermi energy. The RMS deviation for this is 0.02eV, which is usually very good but constitutes a significant error on the scale of these effects.

If a constant angular acceptance is assumed, then the width of parallel momentum, $k_{(x,y)}$, accepted increases with photon energy. Column 7 shows the half width corresponding to a half angle of $\pm 3^\circ$.

The binding energy and energy width both increase significantly as $dk_{(x,y)}$ increases above 0.1 Å. In a previous paper,[10] the maximum $k_{(x,y)}$ of the surface state was determined to be .103 $Å^{-1}$, which was less than the calculated extension of the band gap of .115 $Å^{-1}$. Hence, it appears that the shift and broadening may be due to contributions from bulk bands off-normal. It is also possible, that the larger angular collection is averaging over a region of $k_{(x,y)}$ in which the surface state disperses. S. Kevan[12] has documented the effect in the Cu(111) surface state, and it seems plausible that it is also occurring here. However, the curvature of the dispersion relation would have to be reversed relative to that of the Cu(111) surface state. Regardless of the source of the broadening, it appears then that the lower photon energies (lower $dk_{(x,y)}$ values) provide the most accurate measurement of the binding energy and energy widths.

Thus, for energy and lifetime determination, the values for 6 eV $\leq h\nu \leq$ 12 eV will be used. The binding energy of 0.065 ± .004 eV is less than the value of B^F = 0.13eV determined in Reference 2 but that may be due to improved resolution. (Ref. 2 had a total resolution of 260 meV and half-angle acceptance of ±5° as compared with the values of Column 5, all of which are less than 100 meV, and a half-angle acceptance of ±3°.) The lifetime width was 0.111 ± .007 eV, which is consistent with that observed for Cu(111).[12]

SP-PLATEAU

Indirect transitions are a commonly invoked explanation for the

sp-plateau observed in ARP. If the indirect transitions correspond to a thermal broadening around a direct transition, then the region of the Brillouin Zone contributing to transitions into the final state will be limited and variations of intensity will be expected as the photon energy and thus wavevector are varied. These phonon-assisted transitions were observed in Ag(111) in Ref. 2 and in this experiment. Figure 14 shows a plot from this experiment of the ratio of the sp-plateau height to either the valence band integrated intensity or the valence band maximum. The effect is the same: the ratios are at a minimum at $h\nu = 25eV$ and increases in either direction with a larger maximum at the lower photon energies. The minimum corresponds to sampling near Γ and the intensity increases as the sampling region moves away from Γ toward L, picking up intensity from Band 6 above the other valence bands. Figure 15 is taken from Ref. 13 and demonstrates the same effect in Cu(111), in both the second and third Brillouin Zones. Figure 16 is again the ratio of sp-plateau height to either the valence band integrated intensity or the valence band maximum, this time for Cu(001). In this case, Band 6 crosses the Fermi energy near $h\nu = 14eV$ and Γ corresponds to approximately $h\nu = 32eV$. As described in Ref. 2, the broadening can either be one or more dimensional since Band 6 rises in any direction away from Γ.

E. CONCLUSIONS

The value of improved energy- and angular-resolution is obvious from the above discussions. Experimental determination of the Ag(111) bands were expanded and of improved accuracy. The leading shoulder of

the Ag(111) d-bands is now understood to be due to a surface $3z^2-r^2$ state, as discussed in Chapter III. Only semi-quantitative agreement has been achieved between the results of an experimental determination of the dispersion relations and of an interpolation scheme when rotating off-normal, away from the high-symmetry [111] direction. It appears that either the final state is incorrect or the the tight binding approximation is limiting the accuracy near the zone boundaries. The effect of the band gap in the final state at Γ has been observed as a marked variation of spectral intensities. The binding energy of the Ag(111) surface state has been accurately measured and its lifetime determined. Phonon-assisted momentum broadening and thus indirect transitions have been shown to be the source of the sp-plateau in the ARP of Ag(111), Cu(111) and Cu(001).

REFERENCES

1. N. E. Christensen, Phys. Stat. Sol. (b) 54, 551 (1972).
2. P. S. Wehner, R. S. Williams, S. D. Kevan, D. Denley and D. A. Shirley, Phys. Rev. B 19, 6164 (1979).
3. S. D. Kevan and D. A. Shirley, Phys. Rev. B22, 542 (1980); S. D. Kevan, University of California, Ph. D. Thesis, 1980, unpublished.
4. J. Holzl, F. K. Schulte and H. Wagner, "Solid Surface Physics", Springer-Verlag, 1979.
5. L. Hodges, H. Ehrenreich and N. D. Lang, Phys. Rev. 152, 505 (1966).
6. N. V. Smith, Phys. Rev. B3, 1862 (1971).
7. R. F. Davis, Ph. D. Thesis, Univ. of Cal., 1981, unpublished.
8. S. Bhatnagar, Phys. Rev. 183, 657 (1969).
9. M.O. Krause, P.R. Woodruff and T.A. Carlson, J. Phys. B 14, L673 (1981); M.O. Krause, J. Chem. Phys. 72, 6474 (1980).
10. G. V. Hansson and S. A. Flodstrom, Phys. Rev. B17, 473 (1978).
11. H. F. Roloff and H. Neddermeyer, Solid State Commun. 21, 561 (1977).
12. S. D. Kevan, Phys. Rev. Lett. 50, 526 (1983).
13. D.A. Shirley, R.S. Williams, P.S. Wehner, R.F. Davis and S.D. Kevan, LBL-9344.

TABLE CAPTIONS

Table 1. This is summary of Ag(111) surface state data.

TABLE 1

-1-	-2-	-3-	-4-	-5-	-6-	-7-
$h\nu$	B^F_1(eV)	B^F_2(eV)	$\Delta E^{(eV)}_{MEAS}$	$\Delta E^{(eV)}_{TOT}$	$\Delta E^{(eV)}_{LIFE}$	$dk_{(x,y)}(\AA^{-1})$
6	.070	.038	.128	.065	.110	±0.03
7	.064	.044	.125	.069	.104	±0.04
8	.070	.054	.128	.075	.104	±0.05
9	.064	.052	.138	.083	.110	±0.06
10	.057	.046	.142	.092	.108	±0.06
11	.064	.044	.133	.065	.116	±0.07
12	.064	.046	.140	.067	.123	±0.07
14	.083	.056	.155	.072	.137	±0.08
16	.076	.050	.146	.079	.123	±0.09
18	.095	.056	.154	.088	.126	±0.10
20	.133	.085	.176	.081	.156	±0.11
21	.076	.036	.170	.085	.147	±0.11
22	.171	.087	.208	.089	.188	±0.11
$6 \leq h\nu \leq 12$						
AVE	.065	.046			.111	
±S.D.	±.004	±.005			±.007	
$6 \leq h\nu \leq 22$						
AVE	.08	.053			.13	
±S.D.	±.03	±.016			±.02	

B^F_1(eV) of Column 2 is the binding energy with respect to the Fermi level determined by visual inspection. B^F_2(eV) of Column 3 is the binding energy determined by the gaussian fitting. ΔE_{MEAS}(eV) is the full-width-at-half-maximum (FWHM) from the gaussian fitting. ΔE_{TOT}(eV) of Column 5 is the total resolution, a convolution of spectrometer (.060eV) and monochromator contributions. ΔE_{LIFE}(eV) is the lifetime width of the surface state determined by subtracting ΔE_{TOT} from ΔE_{MEAS} in quadrature. $dk_{(x,y)}$ ($\AA^{-1}$) is the momentum broadening from the half-angular acceptance of 3°.

FIGURE CAPTIONS

Fig. 1. This is a schematic of the experimental geometry of the photoemission experiment, including sample and analyzer rotation in the off-normal experiment.

Fig. 2. Energy distribution curves (EDC's) for $h\nu$ = 32 (top), 30, 28, 26, 24 and 23 eV (bottom) at normal emission.

Fig. 3. EDC's for $h\nu$ = 22 (top), 21, 20, 18, 16 and 14 eV (bottom) at normal emission.

Fig. 4. EDC's for $h\nu$ = 12 (top), 11, 10, 9, 8, 7 and 6 eV (bottom) at normal emission.

Fig. 5. EDC's for $h\nu$ = 21 eV, θ_e = 0 to 40°. θ_e is the external emission angle relative to the surface normal.

Fig. 6. EDC's for $h\nu$ = 14 eV, θ_e = 0 to 40°. θ_e is the external emission angle relative to the surface normal.

Fig. 7. Plot of binding energy versus final-state wave-vector for the normal emission results (filled and open circles) and the calculations of Ref. 1 (lines). Bands 2 and 3 are shifted down 0.3 eV and Bands 4, 5 and 6 are shifted down 0.2 eV. The filled circles are bulk features and the surface state near E_F. The open circles are due to a top layer $3z^2-r^2$ state. The initial state momentum is $k_i = k_f - G(111)$ with $G(111) = 2.661\text{Å}^{-1}$.

Fig. 8. Plot of B^F(eV) vs $k_{(x,y)}$, the crystal momentum parallel to the surface, for the off-normal results at $h\nu$ = 14 eV and $h\nu$ = 21 eV. Filled symbols are bulk features and the surface

state near E_F. The hollow symbols are the $3z^2-r^2$ surface state.

Fig. 9. Comparison of interpolation and experimental results along Γ to L (normal emission).

Fig. 10 The (1,0,-1) plane cross section of the first and second Brillouin Zones, showing the paths taken in the off-normal studies.

Fig. 11. Comparison of off-normal experimental and interpolation scheme results, at $h\nu$ = 21eV. The crosses represent the normal emission results at L.

Fig. 12. Comparison of off-normal experimental and interpolation scheme results, at $h\nu$ = 14eV.

Fig. 13. Plot of the data from Table 1. The dashed line at $h\nu$ = 10.5eV represents the change in the slits and window.

Fig. 14 Ratio of the sp-plateau to the valence band integrated intensity (filled circles) or the valence band maximum (hollow circles) versus photon energy for Ag(111).

Fig. 15 Intensity ratio of the sp-plateau relative to the d-bands, versus photon energy, with the final state zone positions shown across the top.

Fig. 16 Same as Figure 14 but for Cu(001).

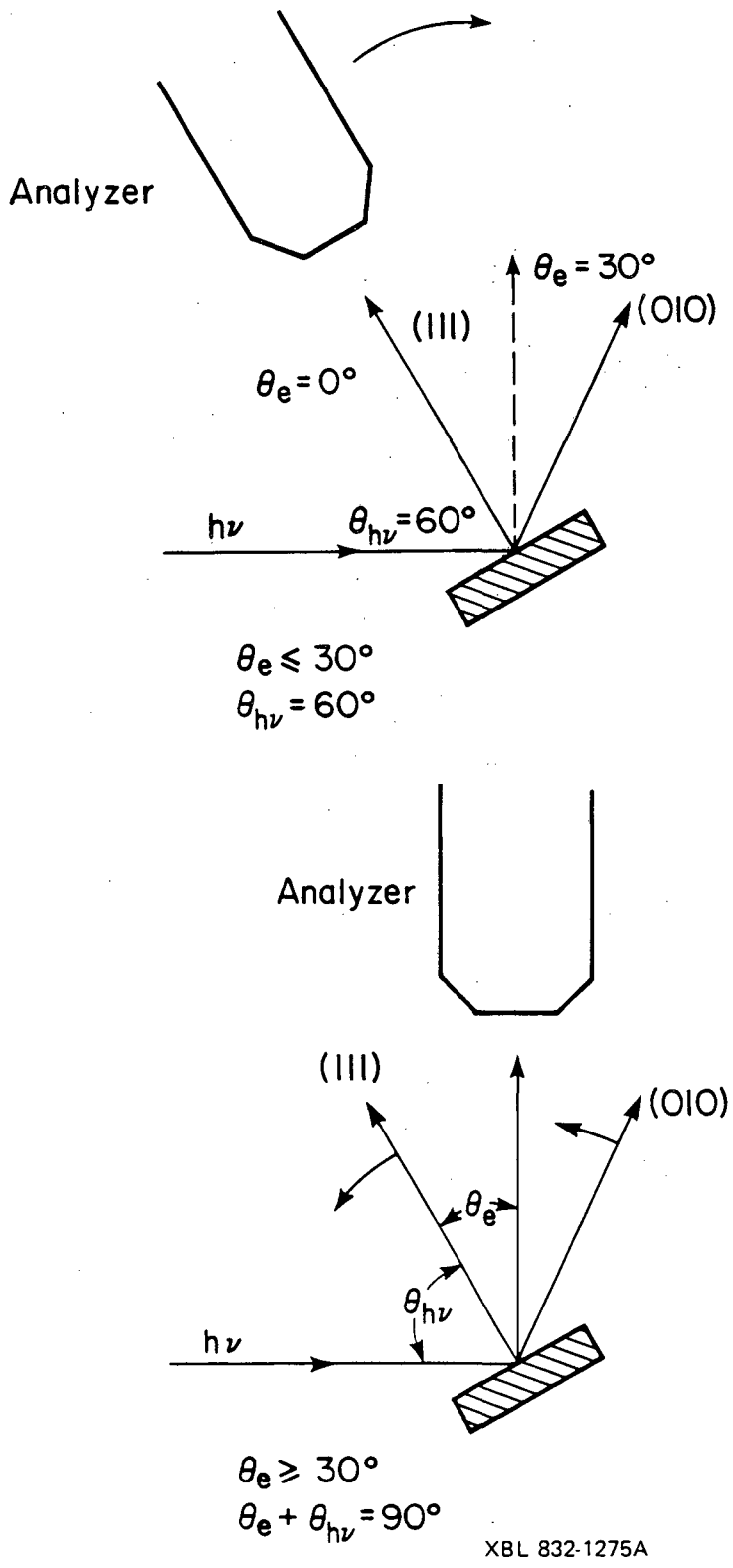
Analyzer
$\theta_e = 30°$
(111)
(010)
$\theta_e = 0°$
$h\nu$
$\theta_{h\nu} = 60°$
$\theta_e \leq 30°$
$\theta_{h\nu} = 60°$
Analyzer
(111)
(010)
θ_e
$\theta_{h\nu}$
$h\nu$
$\theta_e \geq 30°$
$\theta_e + \theta_{h\nu} = 90°$
XBL 832-1275A

Fig. 1

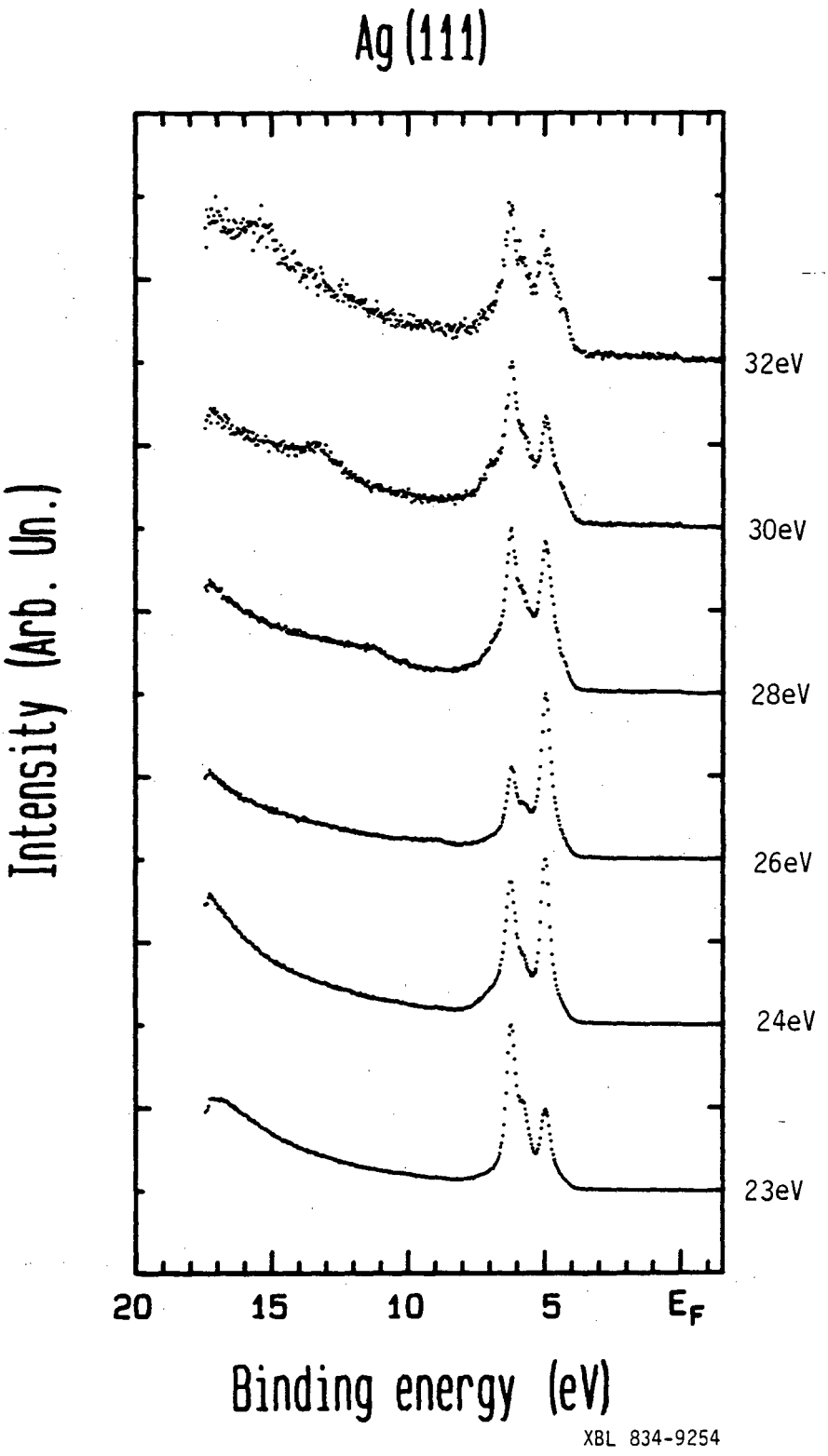
Ag (111)
Intensity (Arb. Un.)
32eV
30eV
28eV
26eV
24eV
23eV
20
15
10
5
E_F
Binding energy (eV)
XBL 834-9254

Fig. 2

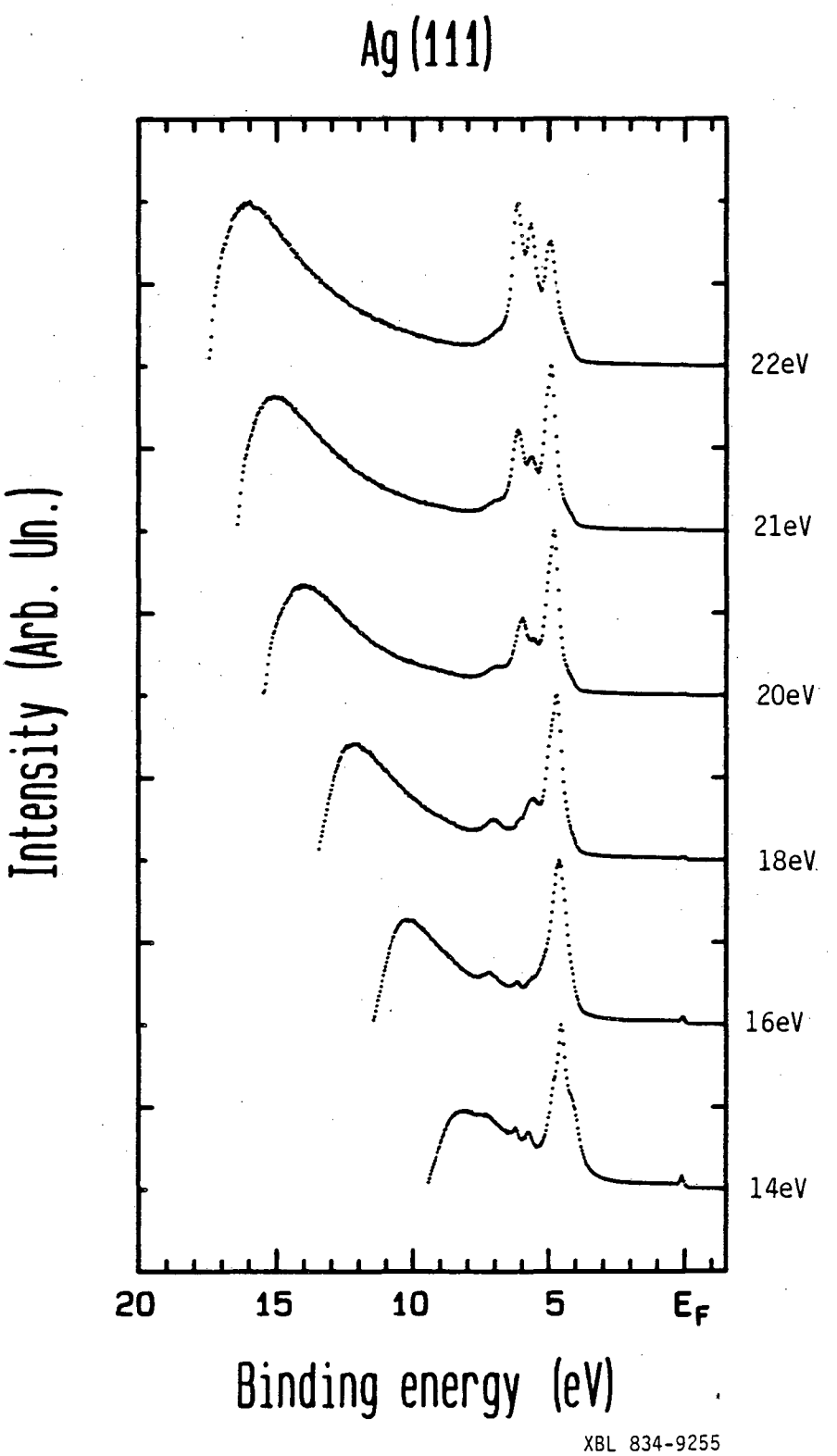
Ag (111)
Intensity (Arb. Un.)
22eV
21eV
20eV
18eV
16eV
14eV
20
15
10
5
E_F
Binding energy (eV)
XBL 834-9255

Fig. 3

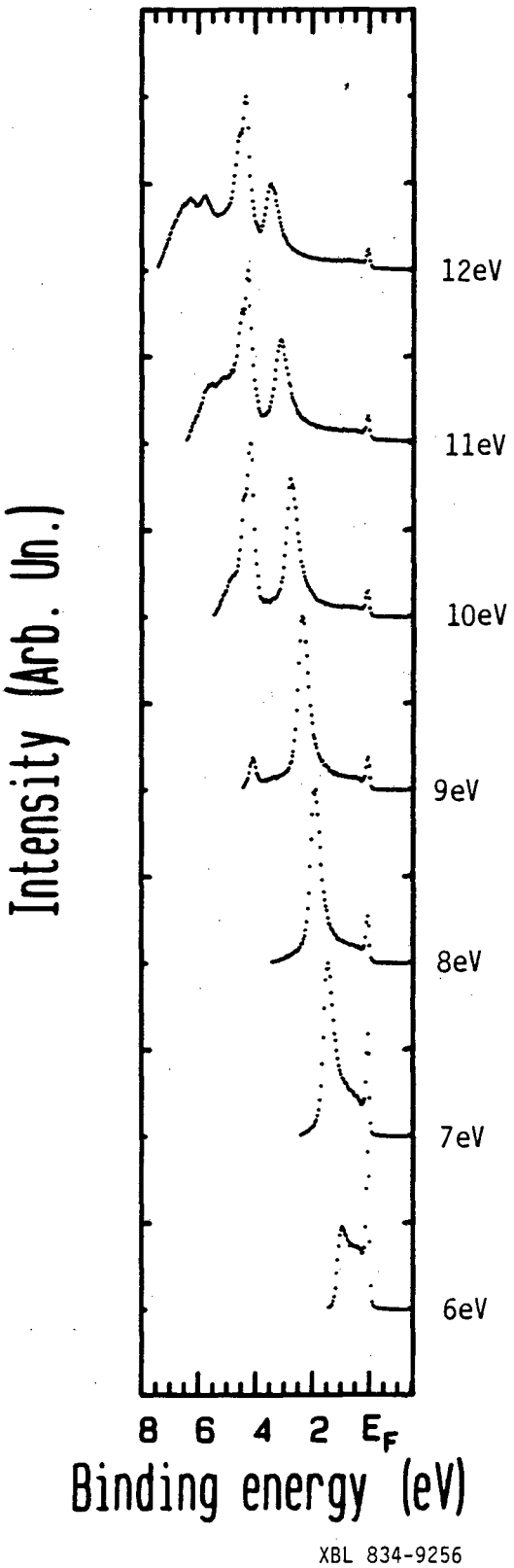
12eV
11eV
10eV
9eV
8eV
7eV
6eV
Intensity (Arb. Un.)
8 6 4 2 E_F
Binding energy (eV)
XBL 834-9256

Fig. 4

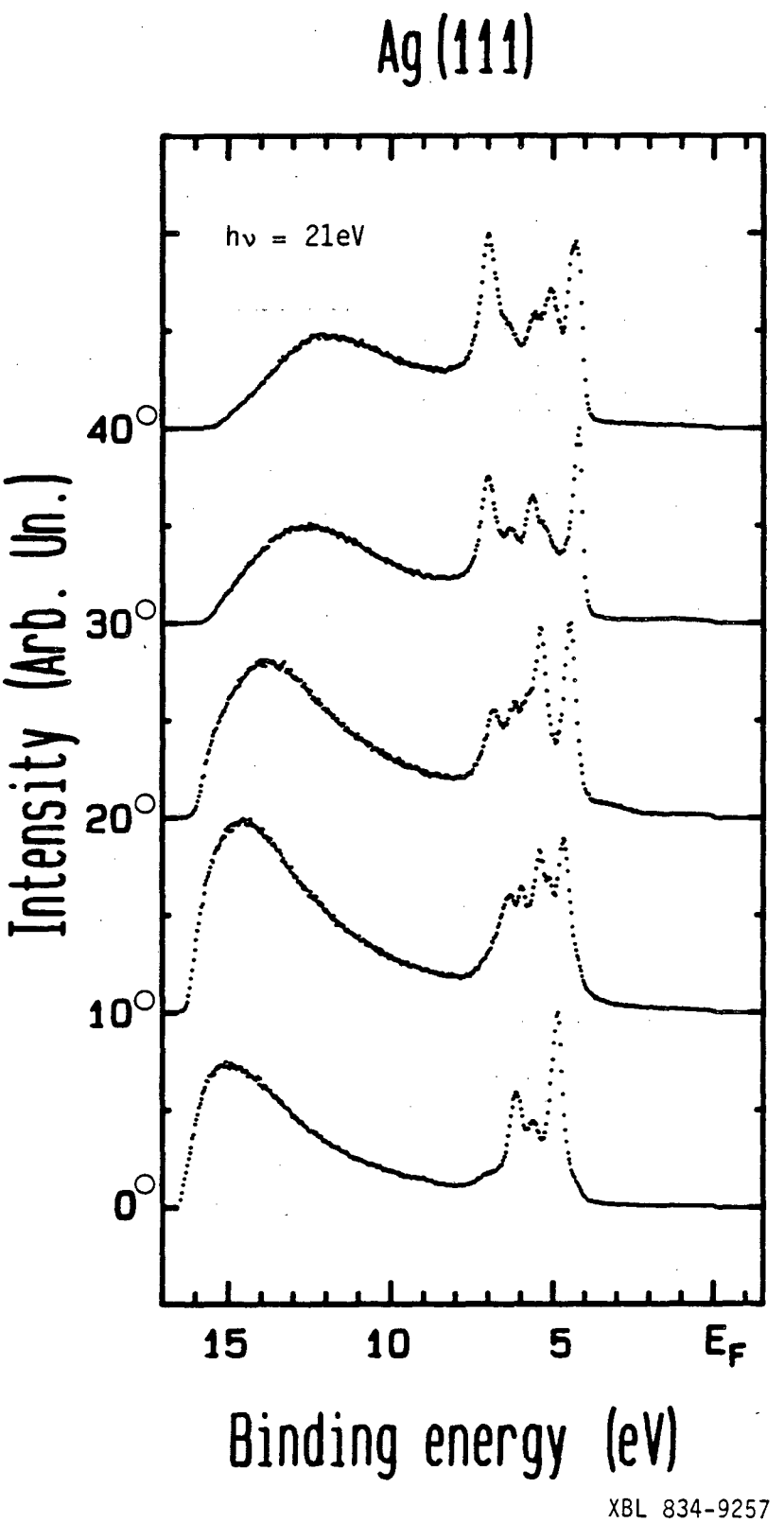
Ag (111)
hν = 21eV
40°
30°
20°
10°
0°
Intensity (Arb. Un.)
15
10
5
E_F
Binding energy (eV)
XBL 834-9257

Fig. 5

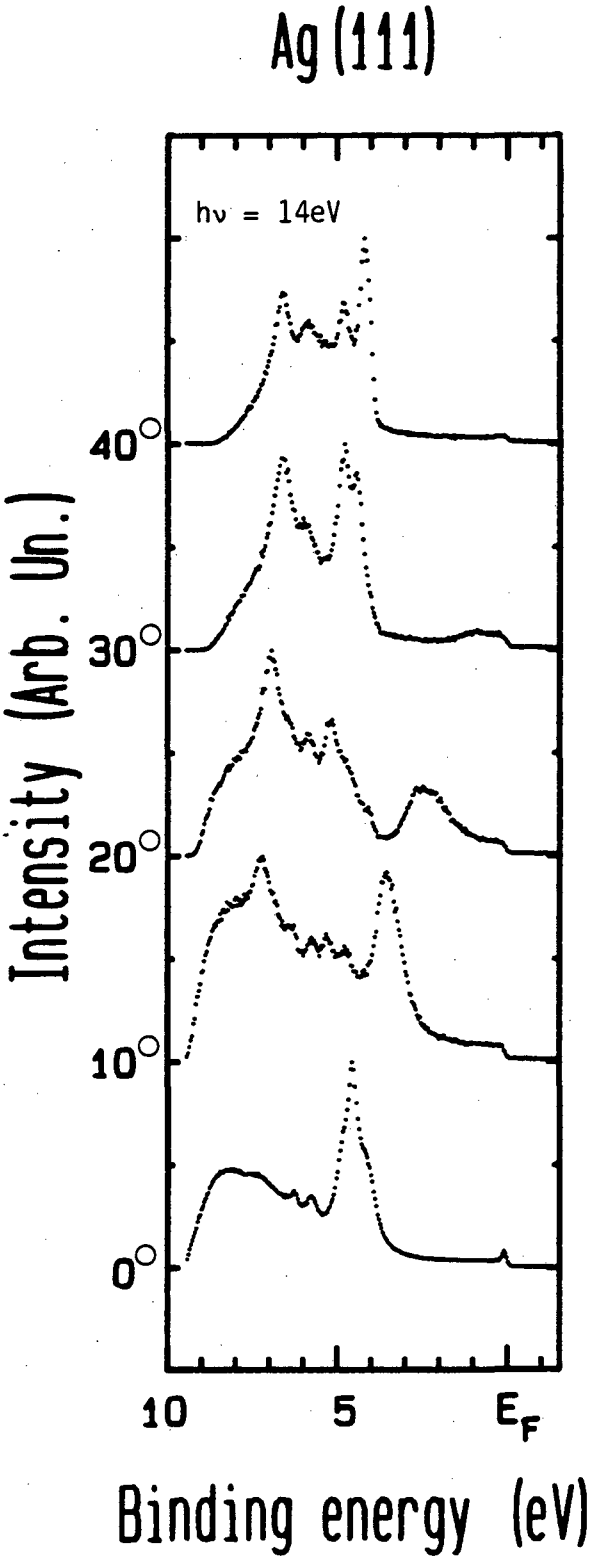

XBL 834-9258

Fig. 6

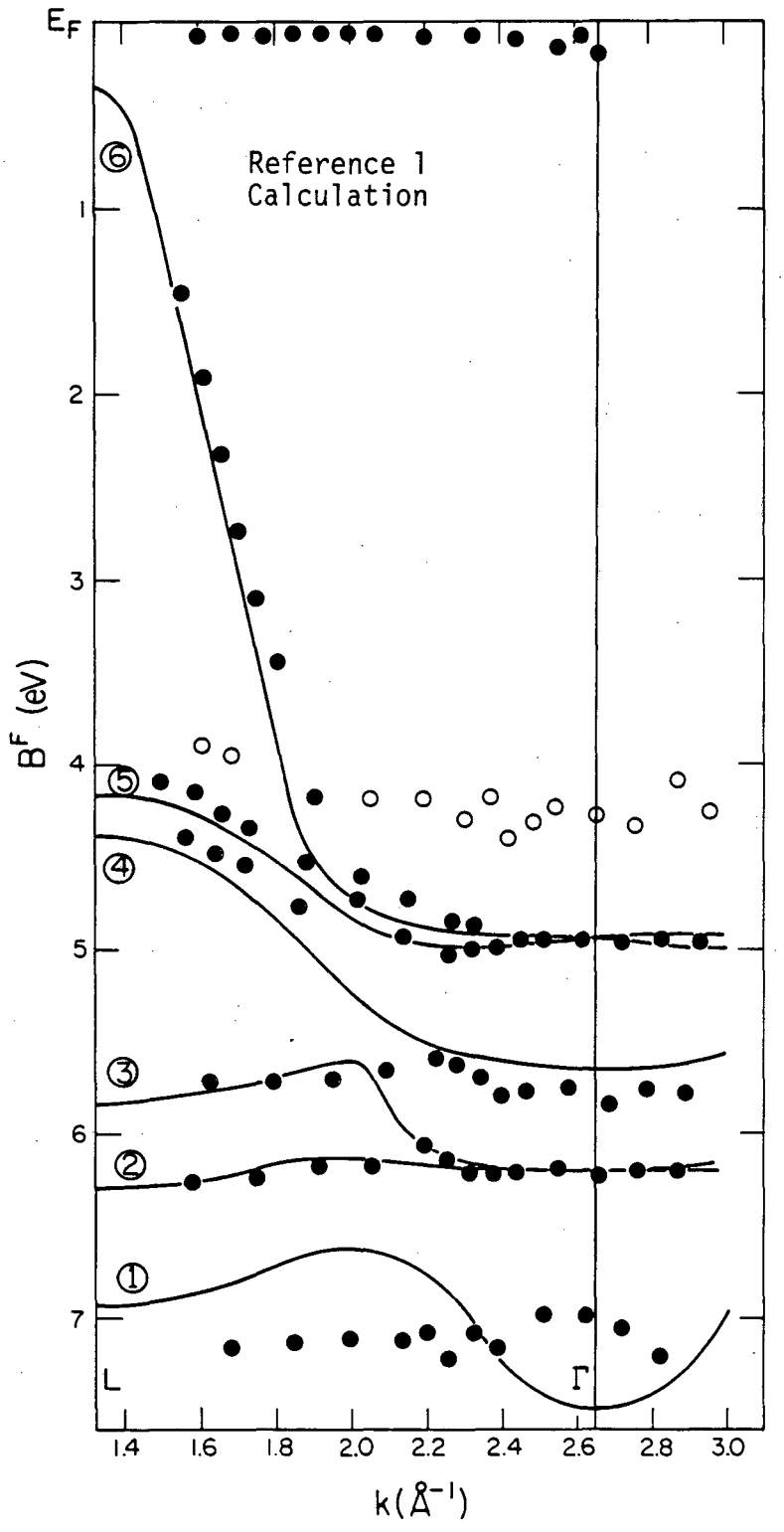
E_F
Reference 1
Calculation
⑥
⑤
④
③
②
①
L
Γ
B^F (eV)
1
2
3
4
5
6
7
1.4
1.6
1.8
2.0
2.2
2.4
2.6
2.8
3.0
k(Å^{-1})
XBL834-152

Fig. 7

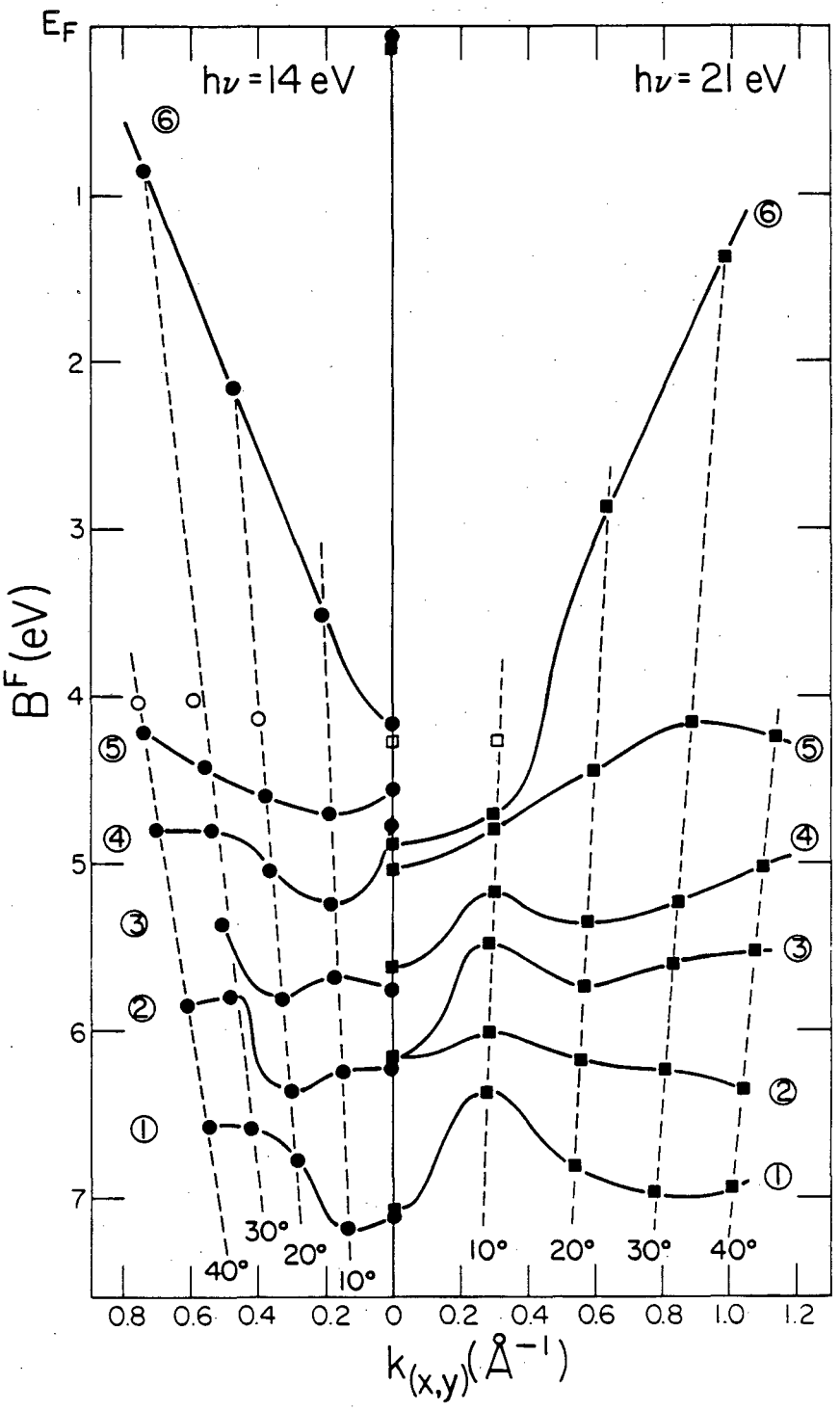
E_F
hν = 14 eV
hν = 21 eV
B^F (eV)
k_(x,y) (Å^-1)
0.8 0.6 0.4 0.2 0 0.2 0.4 0.6 0.8 1.0 1.2
1 2 3 4 5 6 7
⑥ ⑤ ④ ③ ② ①
40° 30° 20° 10° 10° 20° 30° 40°
XBL 834-160

Fig. 8

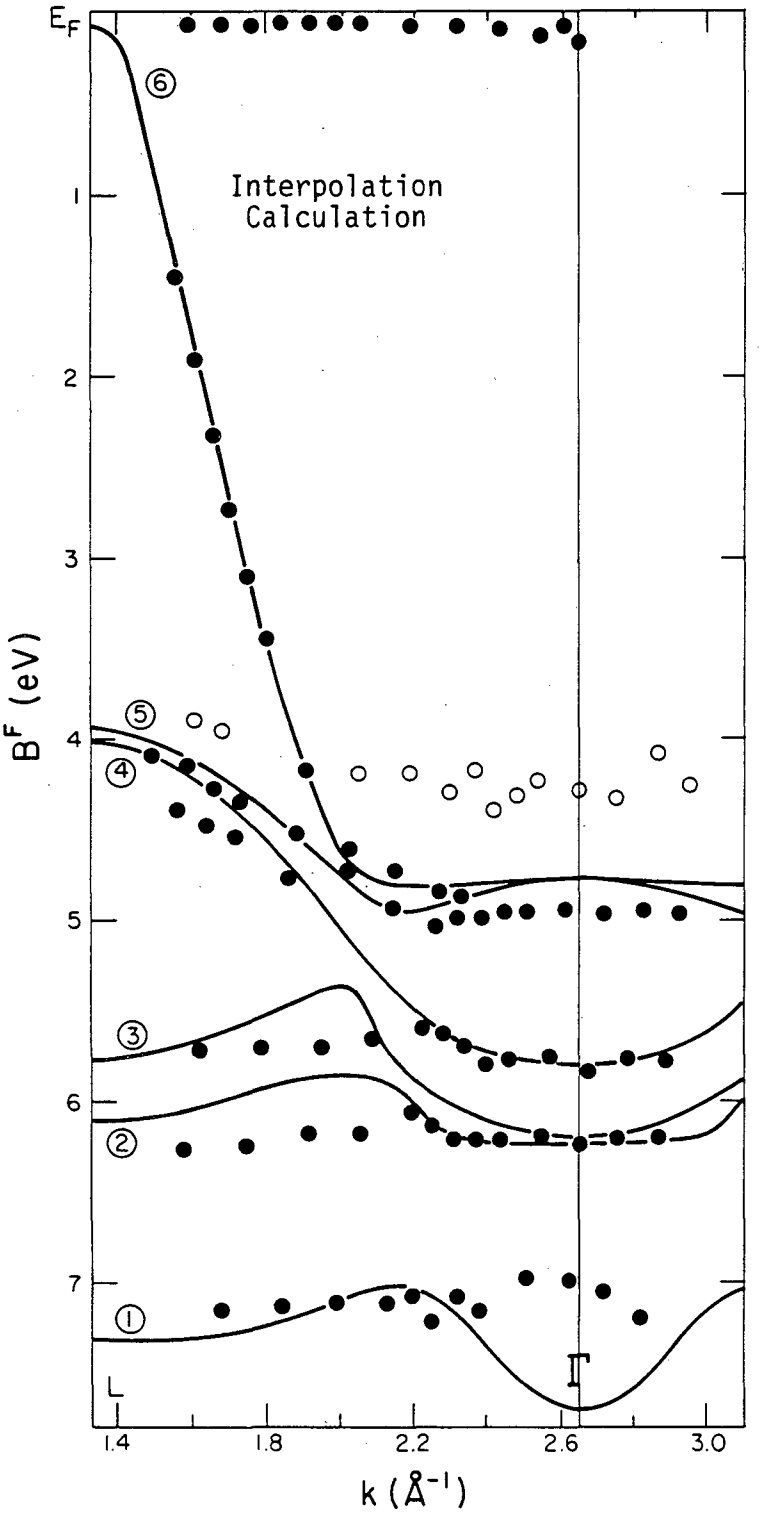
E_F
⑥
Interpolation
Calculation
⑤
④
③
②
①
L
Γ
B^F (eV)
1
2
3
4
5
6
7
1.4
1.8
2.2
2.6
3.0
k (Å^{-1})
XBL 837-987

Fig. 9

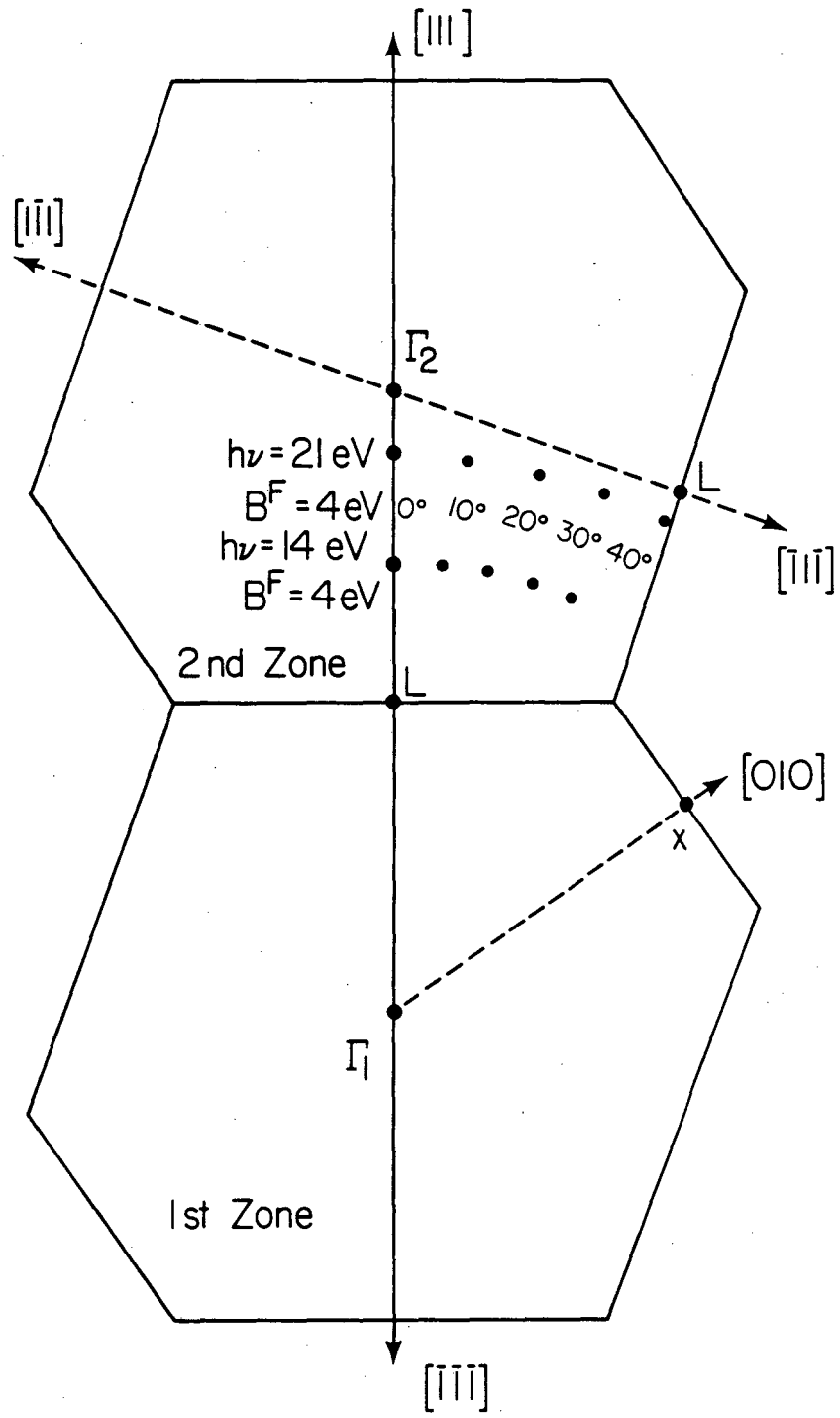

XBL837-990

Fig. 10

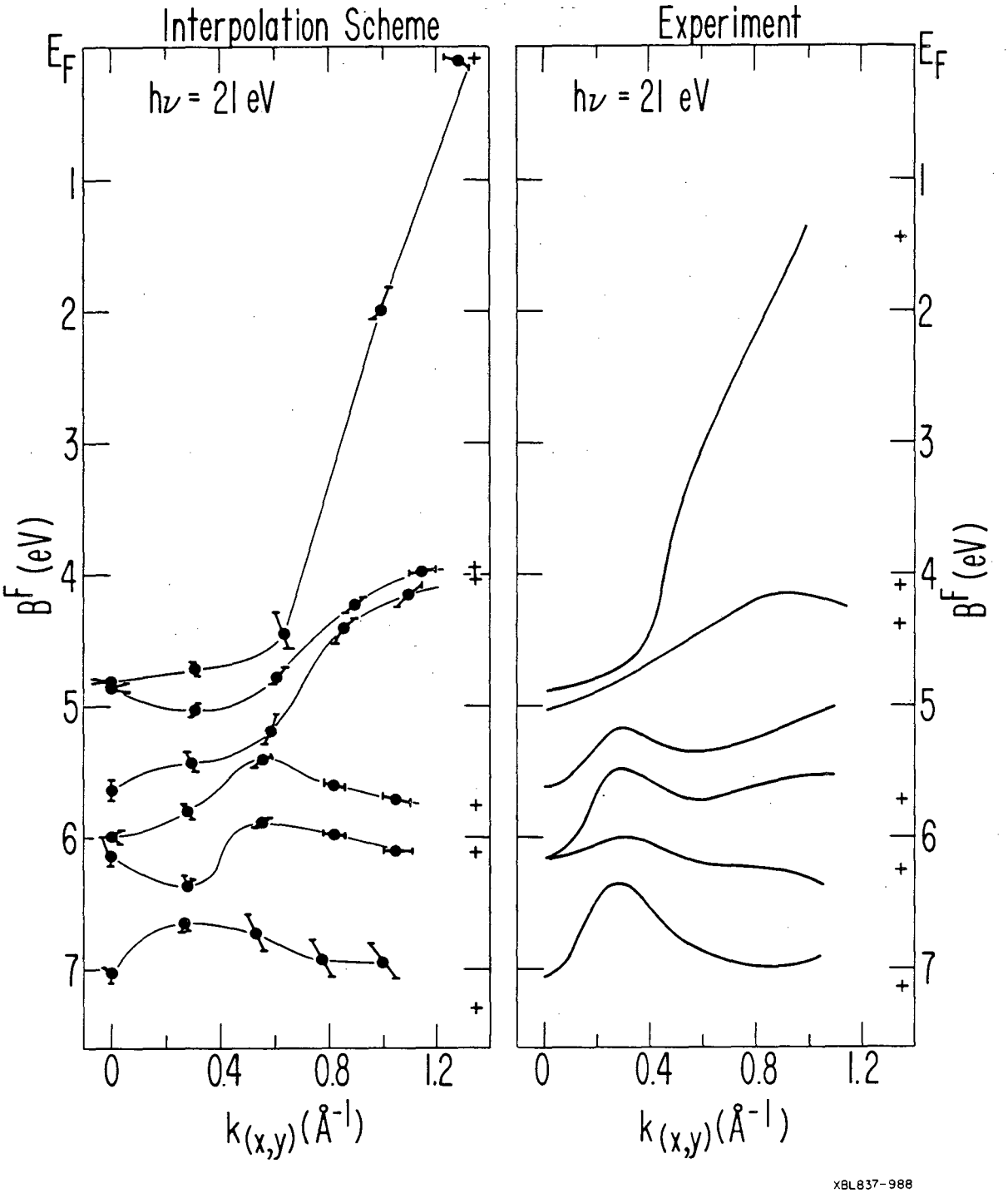
Interpolation Scheme
Experiment
E_F
$h\nu$ = 21 eV
B^F (eV)
1
2
3
4
5
6
7
0
0.4
0.8
1.2
$k_{(x,y)}(Å^{-1})$
XBL837-988

Fig. 11

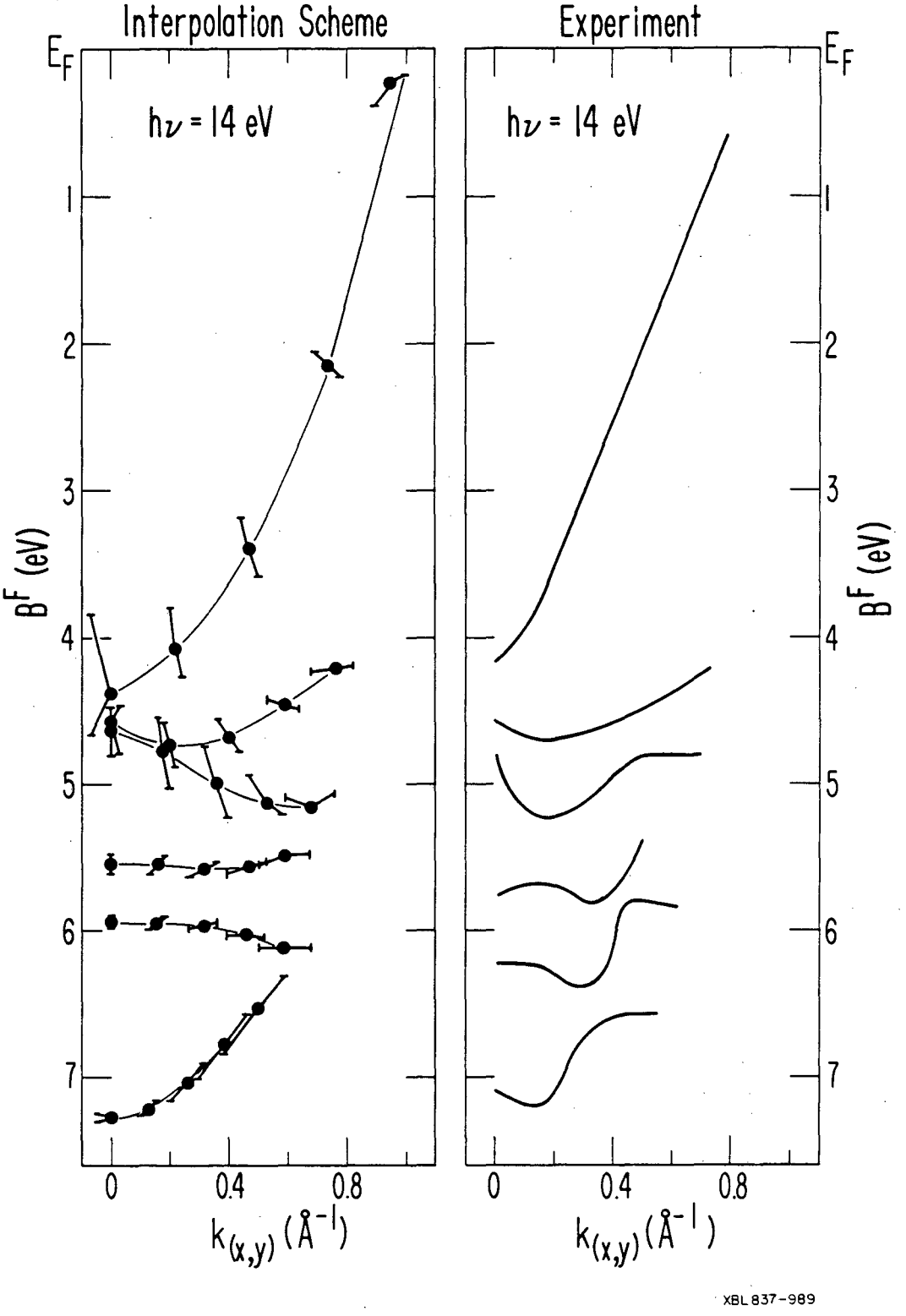
Interpolation Scheme
Experiment
E_F
$h\nu$ = 14 eV
B^F (eV)
1
2
3
4
5
6
7
0
0.4
0.8
$k_{(x,y)}$ ($Å^{-1}$)
XBL 837-989

Fig. 12

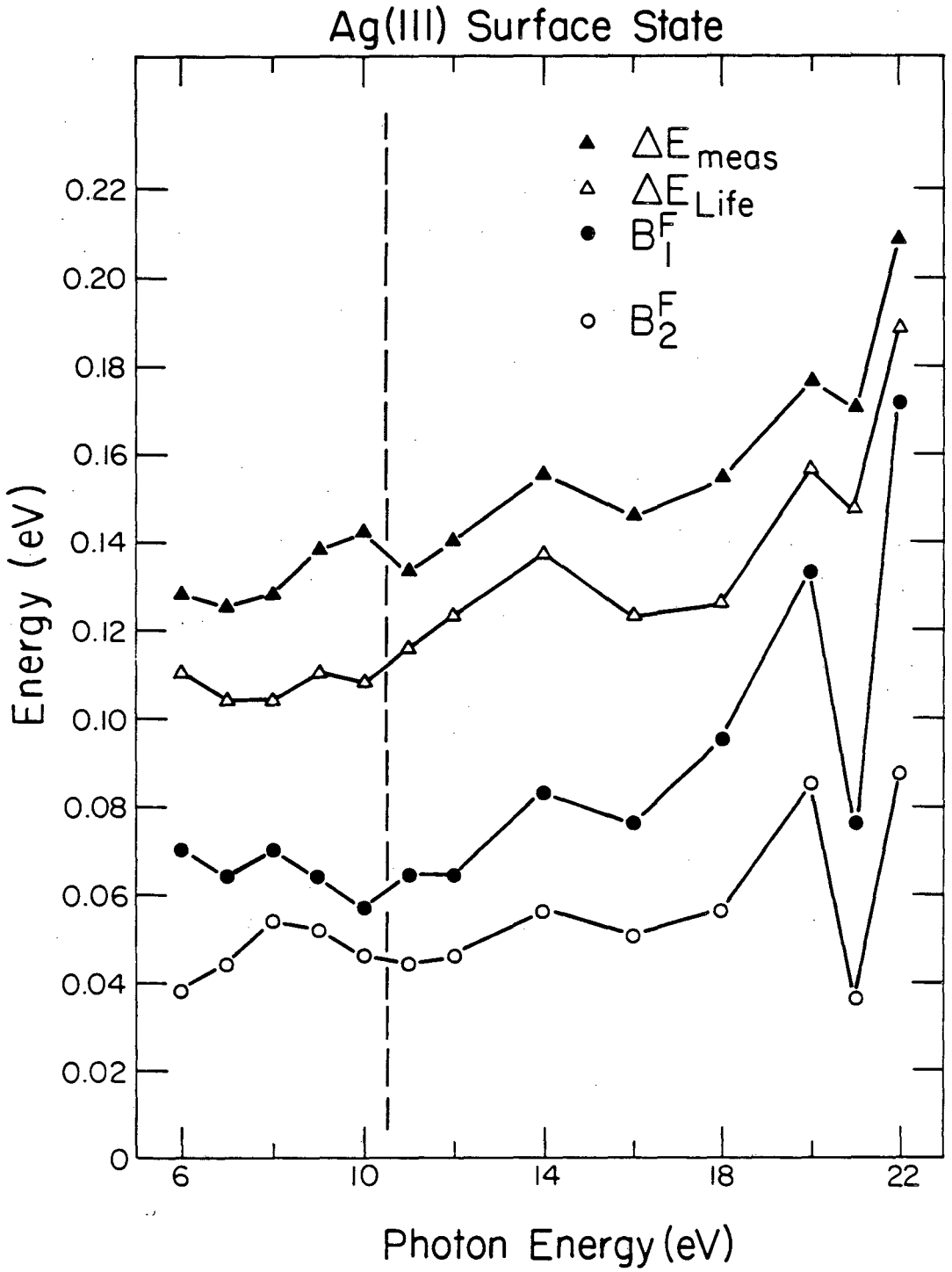
Ag(111) Surface State
ΔE meas
ΔE Life
B F 1
B F 2
Energy (eV)
0.22
0.20
0.18
0.16
0.14
0.12
0.10
0.08
0.06
0.04
0.02
0
6
10
14
18
22
Photon Energy (eV)
XBL837-984

Fig. 13

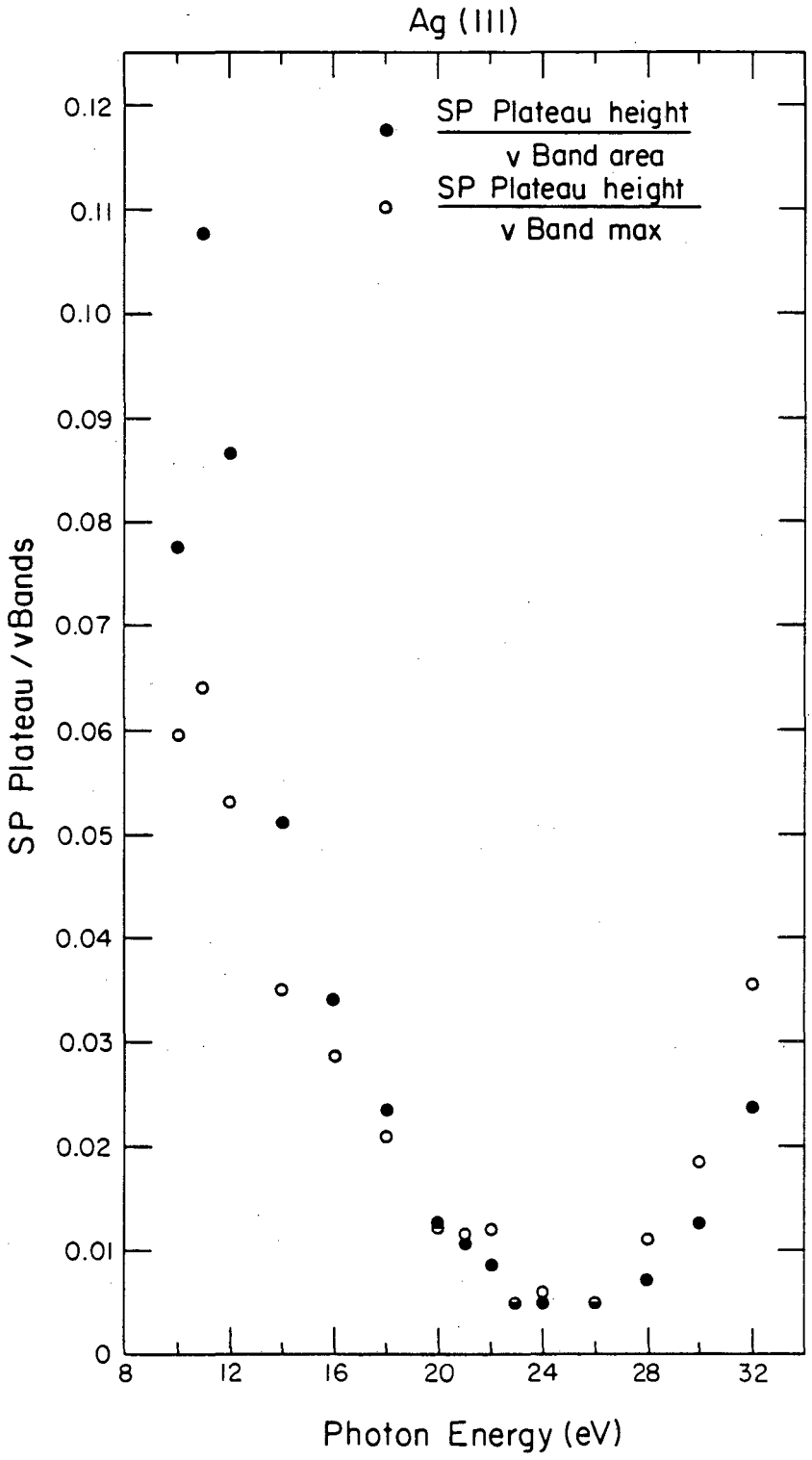

XBL837-977

Fig. 14

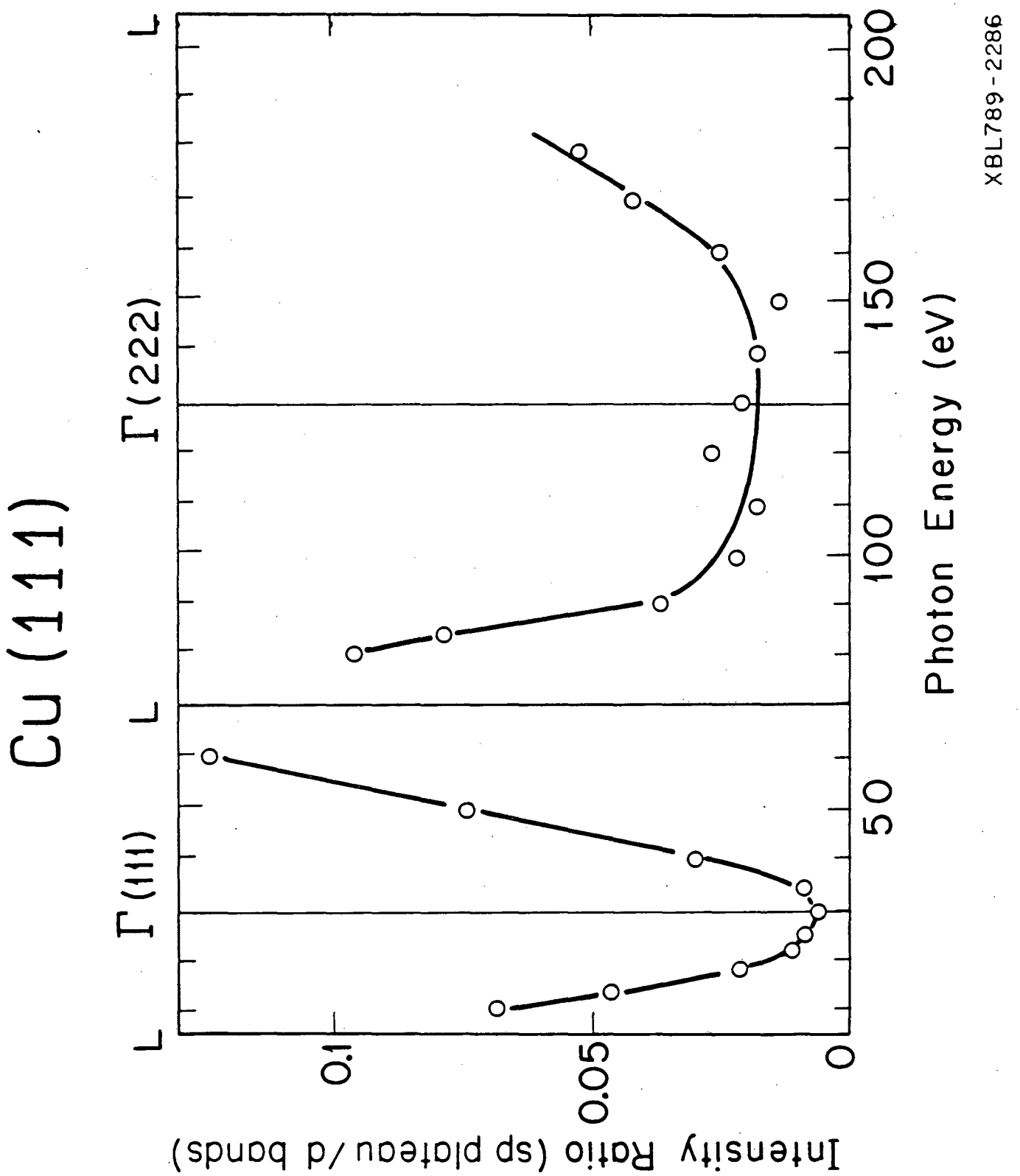
Cu (111)
L
Γ(111)
L
Γ(222)
L
0
0.05
0.1
Intensity Ratio (sp plateau/d bands)
50
100
150
200
Photon Energy (eV)
XBL789-2286

Fig. 15

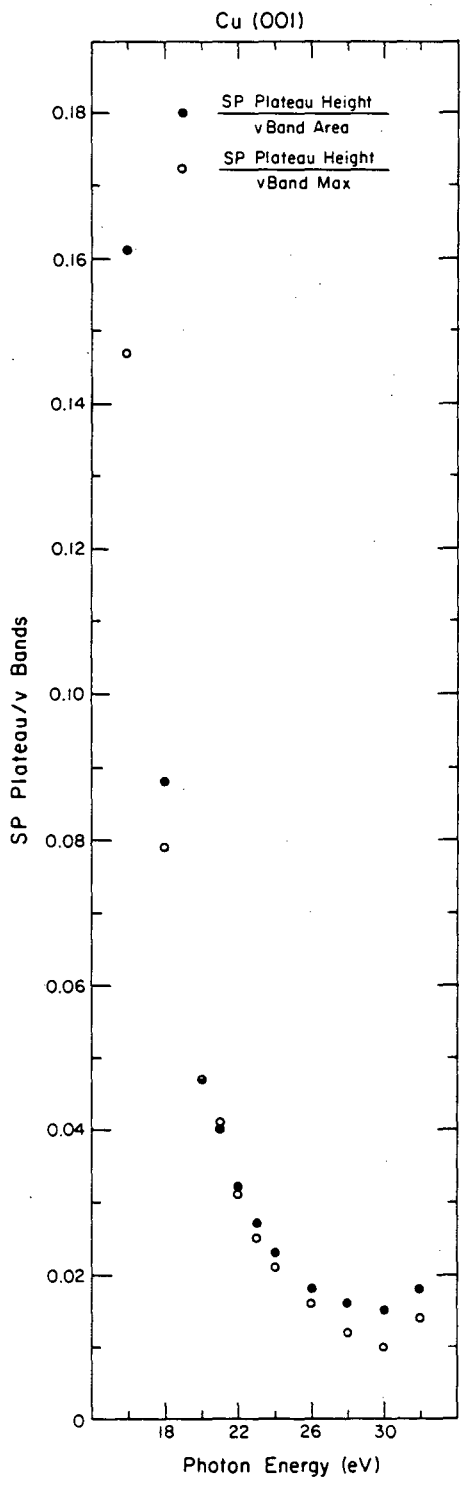
Cu (001)
SP Plateau Height / vBand Area
SP Plateau Height / vBand Max
SP Plateau/v Bands
0.18
0.16
0.14
0.12
0.10
0.08
0.06
0.04
0.02
0
18
22
26
30
Photon Energy (eV)
XBL837-985

Fig. 16

V. Normal Emission Photoelectron Diffraction of c(10x2)Ag/Cu(001)

A. INTRODUCTION

Normal Emission Photoelectron Diffraction (NPD) has been used to determine the surface structure of a number of systems, such as CO/Ni,[1] O/Ni(001)[2,3] and O/Cu(001).[4] The procedure was to measure the cross section of an adsorbate core level as a function of photon, and thus kinetic, energy. These were then compared with multiple scattering calculations performed upon a model of the system that allowed variation of the adsorbate registry and interplanar spacing, $d_\perp$. From a consideration of the basis of these calculations, an analytical expression[5] was derived that suggested that the parameter of importance was $d_\perp$ and that it would be possible to Fourier Transform the NPD curves to determine $d_\perp$.

This implied that it would be feasible to measure the interplanar spacing in c(10 x 2) Ag/Cu(001). As discussed in Chapters 2 and 3, the silver forms a two-dimensional close-packed single layer at one monolayer coverage. From a consideration of a hard sphere model, it seemed plausible that the silver atoms might lie upon the Cu(001) surface with only a limited range of $d_\perp$'s, thus causing an observable modulation in the measured cross sections of the silver core levels.

Unfortunately, it is now believed that this was an overly optimistic appraisal. A more recent evaluation[6,7] of the scattering process suggests that the path length differences, not $d_\perp$, are the important parameters. This does not detract from the validity of the

determinations made by comparison of experiment with scattering calculations but it does have far ranging effects in terms of Fourier transforming scattering curves and the chances of success in using NPD upon an adsorbate system. This will be discussed in more detail in Section C.

The remainder of this chapter deals with cross section measurements made upon the system c(10 x 2) Ag/Cu(001). Section B is a summary of the experimental details. Section C contains the cross section measurements and a discussion of these results.

B. EXPERIMENTAL

The experiment was performed at the Stanford Synchrotron Radiation Laboratory on Beam Line III-3 using the ultra-high vacuum double crystal monochromator. Cross section measurements of the $Ag2p_{3/2}$ level were made over the range of $h\nu$ = 3400 - 3694 eV. The measured binding energy with respect to the Fermi Level was B^F = 3350 eV. The theoretical analyzer resolution was 1eV or less in all of the spectra. The monochromator resolution is approximately 3eV in this range.[8] The contribution from the lifetime should also be on this order in this regime. Thus the measured peak widths of 4-5eV (FWHM) were considered reasonable. The Cu(001) crystal was cleaned by Ar ion etching with continuous sputtering during cycles of heating (550°C) and cooling. A final anneal to 500°C produced an ordered, clean Cu(001) surface, as confirmed by Low Energy Electron Diffraction (LEED) and LEED-optics Auger Electron Spectroscopy (AES). No sulfur, oxygen or silver was observed and the C/Cu derivative Auger intensity

ratio was 0.002. The silver was then evaporated unto the Cu(001) crystal as described in Chapters 2 and 3. A c(10 x 2) Ag/Cu(001) surface was produced which displayed an ordered but incomplete adsorbate LEED pattern and a Ag(355 eV)/Cu(60 eV) derivative Auger ratio that indicated a coverage of 1.4 monolayers of silver. The crystal was then aligned with LEED and laser autocollimation. The crystal was aligned such that the <110> axes of Cu(001) were vertical and horizontal. The angle of incidence of the light was 80° with respect to the surface normal and the Poynting vector and polarization were in the horizontal plane. Unfortunately during this experiment there were vacuum problems and the chamber pressure was 3×10^{-9} torr. Even with the extremely non-reactive metals, silver and copper, this is very high.

C. RESULTS AND DISCUSSION

The Ag $2p_{3/2}$ spectra were fitted with a gaussian using a quadratic background at lower kinetic energies and a gaussian, a gaussian step and constant background at high kinetic energies. In the intermediate regime, the agreement between the two methods was quite good. As an estimate of the photon intensity, the secondary electron intensity at a kinetic energy greater than that of the photoemission peak was measured.[4,6] Dividing the gaussian areas by the secondary electron intensity, the photoemission measurement is normalized to photon intensity, number of scans and analyzer transmission function, approximately. This result is shown in Fig. 1, plotted versus the vacuum kinetic energy (KE) of the ejected Ag

$2p_{3/2}$ electrons. It is necessary to correct for the secondary electron cross section,[4,9] which is approximately proportional to the square of the kinetic energy. This result is shown in Fig. 2.

Figure 2 clearly illustrates that there is no part of the cross section curve that has any modulation or variation that is not overlapped by an Auger feature or edge structure, save the lowest kinetic energies, which are the least reliable due to the steep background. Hence there are no unambiguous NPD modulations. Note particularly the absence of any structure between KE = 175 - 250 eV. It is particularly disturbing that the sulfur 150 eV Auger peak has such a large effect, suggesting that the surface was contaminated.

There are several factors that appear to contribute to the lack of diffraction structure, independent of the problem of contamination. First, the overlayer is too thick. Anything over one monolayer will only serve to wash out the structure. Note, however, that the ordering only occurs at one monolayer and above. Second, the range of d_1's in the first layer may be too great to see any structure. Third, and of the most importance, it now appears that the important parameter is the scattering path length difference, not d_1. Since the c(10 x 2) structure has many sites, there will be an incredible number of path length differences that are on the order of the nearest neighbor distance, not to mention at greater distances. This will wash out any diffraction structure. This suggests that Photoelectron Diffraction will be most successful with single site adsorbate systems and has virtually no chance of success with such a geometrically complicated system.

REFERENCES

1. S. D. Kevan, R. F. Davis, D. B. Rosenblatt, J. G. Tobin, M. G. Mason, D. A. Shirley, C. H. Li and S. Y. Tong, Phys. Rev. Lett. 46, 1629 (1981).

2. D. H. Rosenblatt, J. G. Tobin, M. G. Mason, R. F. Davis, S. D. Kevan, D. A. Shirley, C. H. Li and S. Y. Tong, Phys. Rev. B 23, 3828 (1981).

3. S. Y. Tong, W. M. Kang, D. H. Rosenblatt, J. G. Tobin and D. A. Shirley, Phys. Rev. B 27, 4632 (1983).

4. J. G. Tobin, L. E. Klebanoff, D. H. Rosenblatt, R. F. Davis, E. Umbach, A. G. Baca, D. A. Shirley, Y. Huang, W. M. Kang and S. Y. Tong, Phys. Rev. B26, 7076 (1982).

5. S. Y. Tong and J. C. Tang, Phys. Rev. B25, 6526 (1982).

6. J. J. Barton, C. C. Bahr, Z. Hussain, S. W. Robey, J. G. Tobin, L. E. Klebanoff and D. A. Shirley, submitted to Phys. Rev. Lett., LBL-14645.

7. J. J. Barton, LBL-14993.

8. Z. Hussain, E. Umbach, D.A. Shirley, J. Stohr, and J. Feldhaus, Nucl. Instr. Meth. 195, 115 (1982); J.J. Barton, private communication.

9. M. P. Seah, Surf. Sci. 17, 132 (1969).

Figure Captions

Fig. 1. The fitted gaussian area of the $Ag2p_{3/2}$ peak divided by the secondary electron intensity, plotted versus the external kinetic energy of the ejected $Ag2p_{3/2}$ electrons.

Fig. 2. The relative cross section of the $Ag2p_{3/2}$ peak versus the kinetic energy. The data from Fig. 1 was corrected for the secondary electron cross section by dividing by the kinetic energy squared.

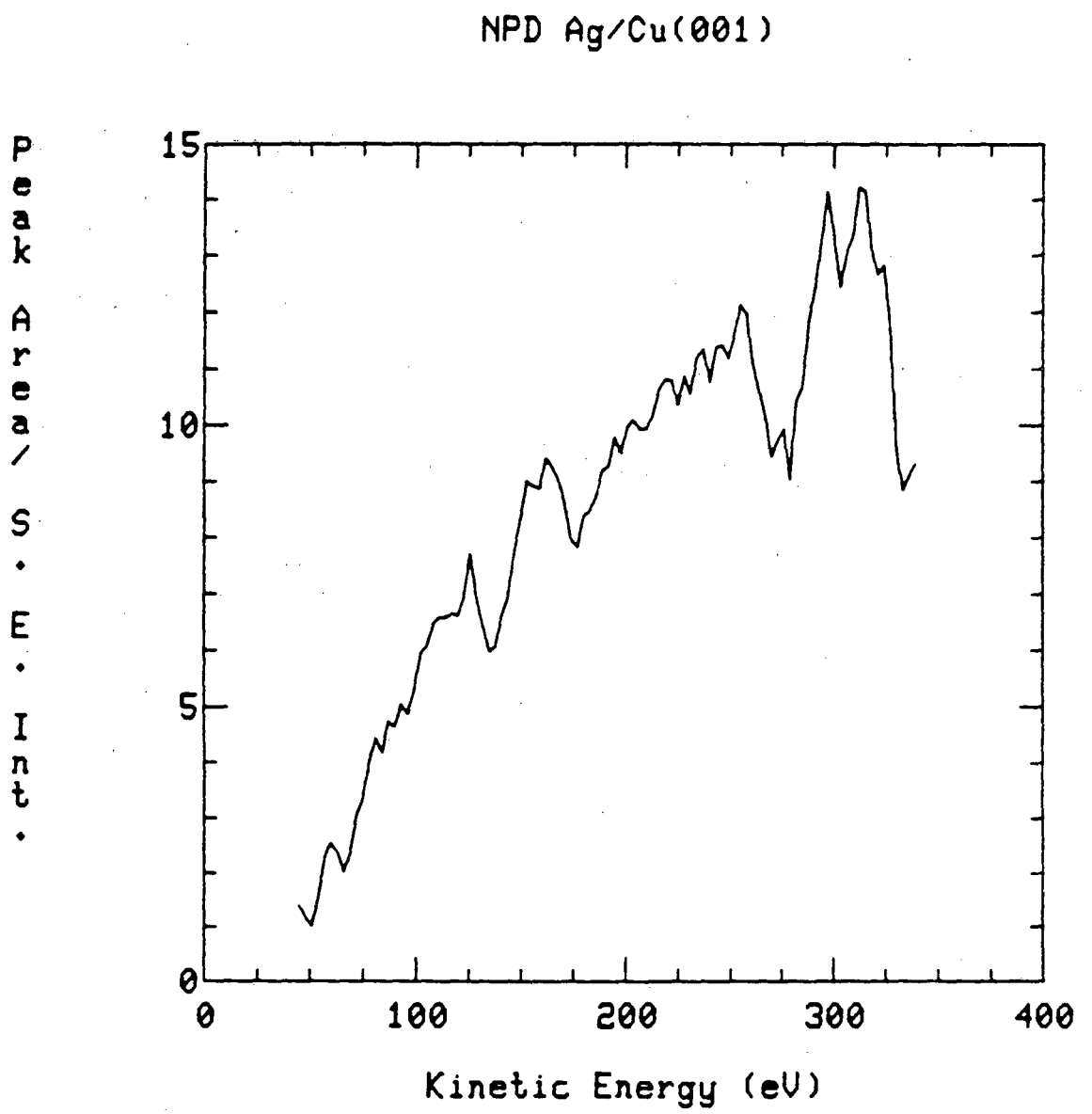
NPD Ag/Cu(001)
Peak Area/ S. E. Int.
15
10
5
0
0
100
200
300
400
Kinetic Energy (eV)

Fig. 1

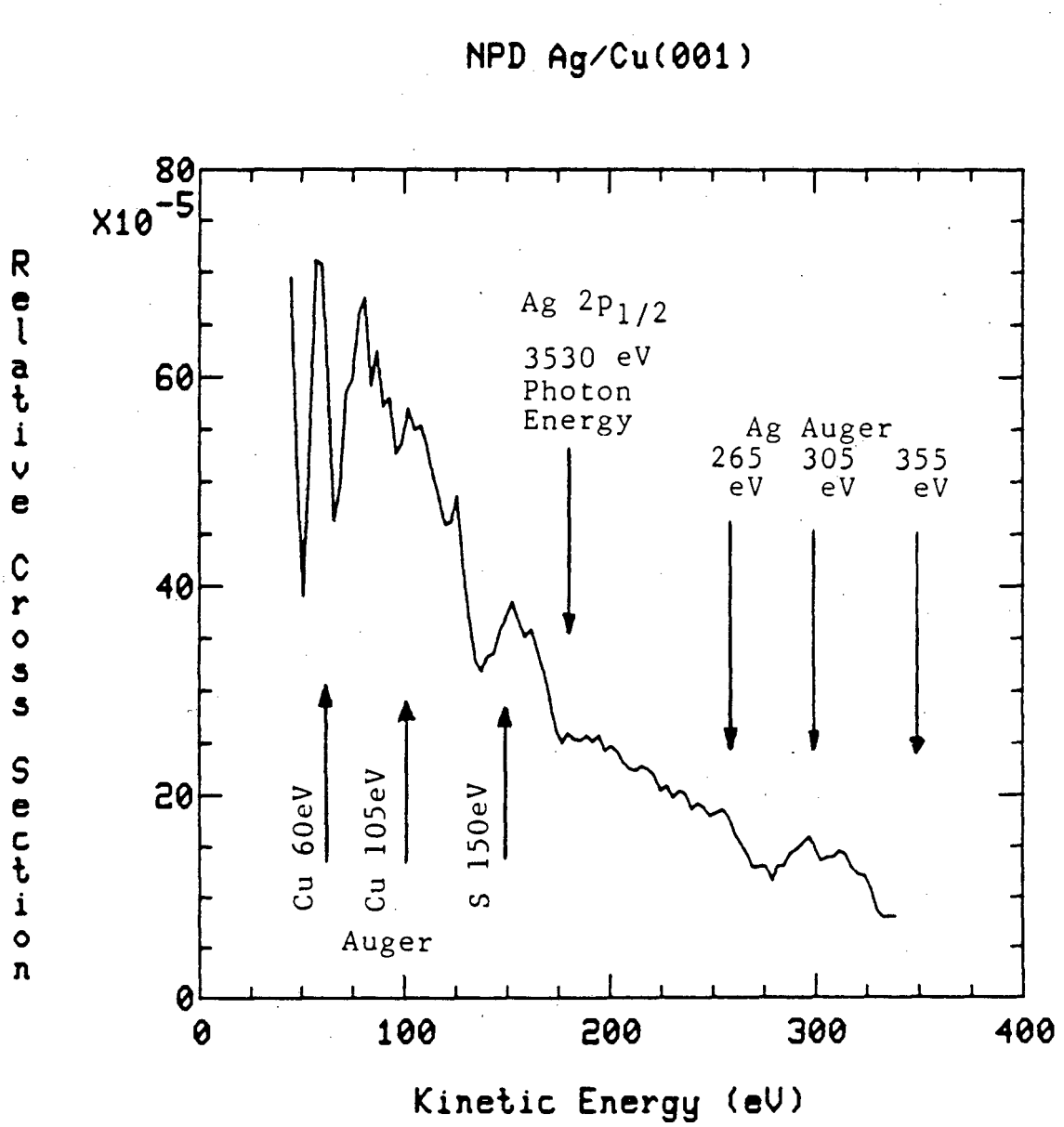
NPD Ag/Cu(001)
Relative Cross Section
X10-5
80
60
40
20
0
0
100
200
300
400
Kinetic Energy (eV)
Ag 2P1/2
3530 eV
Photon
Energy
Ag Auger
265 eV
305 eV
355 eV
Cu 60eV
Cu 105eV
Auger
S 150eV

Fig. 2

VI. General Overview and Conclusions

The development of the valence electronic structure of a metal overlayer system has been observed with Angle-Resolved Photoelectron Spectroscopy. The silver 4d-bands of c(10x2)Ag/Cu(001) behave two-dimensionally at coverages near one monolayer and are converging toward three-dimensional behavior by exposures of 5 ML, as evidenced by the comparison with the spectral and dispersive behavior of bulk, single-crystal Ag(111). The behavior of the non-d components of the silver valence bands is not so well understood: while the d-bands appear unaffected by interaction with the substrate, the sp states may be the source of bonding to the Cu(001) surface. An attempt to determine the interplanar spacing of the monolayer system with NPD failed. Nevertheless, this represents the first explicit experimental observation of the development of valence electronic structure from two- to three-dimensionality.

Orare est laborare, laborare est orare.

[To pray is to work, to work is to pray.]

Ancient motto of the Benedictine order

ACKNOWLEDGEMENTS

First and foremost, I wish to thank Dave Shirley for the opportunity to work and learn under his direction. I can honestly say that I can't imagine having studied under anyone else.

No man is an island: there is no situation more aptly described by that than a research group working at a synchrotron radiation facility and I am personally indebted to many people. Steve Kevan, Rich Davis, Gary Mason, Dave Denley and Danny Rosenblatt were my patient instructors in the art of science. Dennis Trevor, Charlie Bahr and John Barton solved many of my data analysis problems with their superb programming. Dave Tong and his group at UWM proved to be excellent partners in our NPD experiments. Zahid Hussain, Eberhard Umbach, Albert Baca, Leonard Klebanoff and Jim Pollard were crucial to performing of the experimentation. Joe Katz, Don Malone, the late Dick Escaboles and Barbara Moriguchi helped to keep the "ARPES" effort rolling. Wini Heppler's crystals preparations were first class and Steve Robey provided real insight into the science at the heart of our experiments. Jeff Nelson, Bill Gignac and Stan Williams were a great bunch of coworkers at SSRL. It is patently unfair to categorize people thusly: they have helped me in myriad, indescribable ways and

served as teachers as well as coworkers. Though it be insufficient, it is heartfelt when I offer them my thanks. I also owe a debt of gratitude to Claude Woods, Rich Saykally and Yuan Lee for their interest in my work and wellbeing.

Finally and most importantly, I wish to thank my friends and family for their support and encouragement over these last five years. In particular, I would like to thank my grandparents, Mary, Julie, Tom Jr., Linda, Sean and, above all, my parents Tom and Micky, for their patience and help. This would not have been possible without them.

This report was done with support from the Department of Energy. Any conclusions or opinions expressed in this report represent solely those of the author(s) and not necessarily those of The Regents of the University of California, the Lawrence Berkeley Laboratory or the Department of Energy.

Reference to a company or product name does not imply approval or recommendation of the product by the University of California or the U.S. Department of Energy to the exclusion of others that may be suitable.

TECHNICAL INFORMATION DEPARTMENT
LAWRENCE BERKELEY LABORATORY
UNIVERSITY OF CALIFORNIA
BERKELEY, CALIFORNIA 94720